ELECTRICAL PRECISION
TREATMENT OF MATERIALS

Anodic Treatment of Strengthening the Electrochemical Coatings in Electrolytes for Electrochemical Machining: 1. Micromachining of CoW Coatings in Nitrate and Nitrate-Alkaline Solutions

S. A. Silkin[a, b], V. I. Petrenko[b], and A. I. Dikusar[a, b]

[a]*Shevchenko Pridnestrov'e State University, ul. 25 Oktyabrya 128, Tiraspol, Republic of Moldova*
[b]*Institute of Applied Physics, Academy of Sciences of Moldova,*
ul. Academiei 5, Chisinau, MD–2028 Republic of Moldova
e-mail: dikusar@phys.asm.md

Abstract—Polycrystalline CoW coatings (with a 5–6 at % content of W) were found to dissolve in a 2M $NaNO_3$ solution with 100% current efficiency while reaching the conditions of thermokinetic instability (TKI) upon attaining the anode limiting currents resulting from the salt's passivation. The anodic micromachining of nanocrystalline coatings (22–25 at % of W) in a nitrate solution also occurs with a 100% current efficiency, though at a very high degree of dissolution instability prior to attaining the TKI. The electrochemical micromachining of nanocrystalline coatings in a nitrate-alkaline solution (2M $NaNO_2$ + 0.5 M KOH) at low current densities occurs at a current efficiency close to zero, but, in all the cases under the TKI conditions, the current efficiency (upon the coatings treatment with different W contents in different solutions) exceeds the 100% value. A procedure for the removal of the coating material under the TKI conditions is offered that suggests the formation of an oxide-salt film and its periodic destruction due to a thermal explosion. It is shown that the minimal surface roughness is registered after the coating dissolution under the TKI conditions. Results are reported that confirm the possibility of controlling the strengthening (weakening) process of a surface layer after micromachining in different electrolytes using constant and pulse currents.

DOI: 10.3103/S1068375511040132

INTRODUCTION

Surface modifying using electrophysical and electrochemical methods for manufacturing surfaces with certain functional properties is an efficient method for their treatment that is extensively used in industry. One such method is electrochemical strengthening (electrolytic deposition of coatings). It was earlier mentioned that the anodic etching (dissolution) of these coatings used to obtain apertures or cavities, including those with complicated forms, can be regarded as an efficient method for the micromachining of these surfaces [1, 2].

However, the technological development based on the anodic etching of these coatings needs a number of principal questions to be answered:

—To what degree the electrolytes and modes of electrochemical machining (that have been developed for bulk materials) are applicable for thin films (which commonly are from a few to dozens of microns thick) manufactured by the electrochemical technology.

—Whether or not the functional (e.g., mechanical) properties of the surface remain unchanged after the anodic surface modification and what the reasons for the change in the surface properties after the etching are.

—Whether the dimensional effects of changes in the properties exist, i.e., whether the properties change with respect to the depth of the surface treatment (the volume of the removed material).

—Whether general ways for controlling the surface roughness exist, since owning to the relatively small thicknesses of the coatings and the absence of allowance for subsequent finishing (if needed), the roughness plays a key role in the electrochemical machining.

In [2, 3], some of the above questions were answered using the example of the anodic dissolution of chromium coatings in electrolytes for electrochemical machining (ECM). It was shown, in particular, that, after the anodic treatment, the surface softening takes place, which depends considerably both on the nature of the electrolyte and the modes of treatment, as well as on the depth of the etching of the strengthening layer. The role of the surface heat release and its effect on the roughness of a surface and the degree of its softening are also revealed [2, 3].

However, the technology of manufacturing strengthening chromium coatings from electrolytes based on hexavalent chromium involves severe ecological risks, which requires the creation of such surfaces that would allow the possibility of developing the technology under conditions that are more moderate eco-
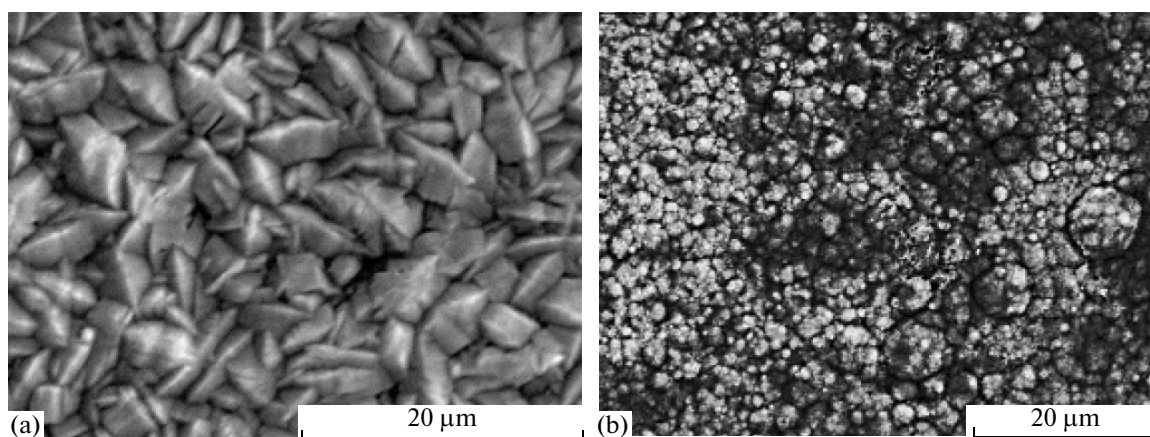
Fig. 1. CoW-alloy morphology that contains 6 at % of W (a) and 22 at % of W(b).

logically provided that the functional properties of the surfaces are conserved. The electrochemical CoW coatings obtained from citrate or gluconate solutions can be regarded as a technology for replacing the one used for obtaining electrolytic chromium [4–10]. This study answers the above questions in the context of the conditions of the micromachining of the CoW coatings manufactured by electrodeposition from citrate solutions.

EXPERIMENTAL

The cobalt-tungsten manufacturing of coatings was performed from a citrate electrolyte with different concentrations of $CoSO_4$ and also with concentrations of 0.2 M of Na_2WO_4 + 0.04 M of $C_6H_8O_7$ + 0.25 M of $Na_3C_6H_5O_7$ + 0.65 M of H_3BO_3 at a deposition temperature of 60°C and pH = 6.7. At a concentration of cobalt sulfate of 0.2 M, this composition for obtaining cobalt-tungsten coatings with a high content of tungsten was used in [8, 9, 11–13]. In our work, the same electrolyte was used with a cobalt sulfate content of 0.28 M. It will be shown below that a change in the cobalt-sulfate concentration, even as small as that, leads to a substantial change (a decrease) in the W content of the coating. The ratio of the tungsten and cobalt concentrations during the deposition from both citrate and gluconate solutions is strongly affected by the potential (the current density) [6, 8–13], the hydrodynamic conditions [10, 12–15], and also by the degree of the long-term operation of the electrolyte (the value of the passed charge per its volume unit) [14].

Under the conditions of micromachining, the surface roughness is significant, since the value of the diluted layer is limited to 10–20 µm and less. In [12], it is shown that the minimal roughness of the coating electrodeposited from the above electrolyte (without the addition of brightening agents and surface active substances (SAS)) at a cobalt sulfate concentration of 0.2 M is reached at the electrodeposition current den-

sity of 1–2 A/dm², and it is independent of the hydrodynamic conditions. This very range of the current densities is used in our study. The deposition was carried out from a nonagitated solution.

The electrodeposition was performed onto 10-mm-diameter steel St3 specimens. The latter were mechanically polished, which was followed by the deposition of a 1-µm-thick nickel underlayer from a sulfate-chloride bath at pH = 5.4. The mean value of the irregularity of the initial surface was Ra = 0.15–0.20 µm. The deposition was performed in a thermostatically controlled cell with an electrolyte volume of 500 ml. In order to increase the productivity of manufacturing the coatings, the subsequent studies were carried out using six specimens simultaneously; the latter were arranged on a special holder parallel to the anode, which was a graphite plate with a total area of 25 cm². The deposition temperature was 60°C.

The polycrystalline coatings were produced at a tungsten concentration of 5–6 at % (Fig. 1) as a result of the deposition from an electrolyte with a cobalt sulfate concentration of 0.28 M and a current density of 1 A/dm². The microhardness of those coatings was relatively low (360 kgf/mm²). It should be noted that the indicated concentrations of tungsten correspond to its content in the "metal" part of the alloy. The matter is that the alloy's composition often comprised carbon and oxygen, with their concentrations varying in different specimens.

The nanocrystalline (close to amorphous) coatings that contained tungsten of 22–25 at % (Fig. 1b) were manufactured using a bath with the cobalt sulfate concentration of 0.2 M and at a current density of 1–2 A/dm². The concentrations differed both inside the lot of 6 specimens and between the different lots, which could have resulted either from the different hydrodynamic conditions on each of the six electrodes or from the degree of the electrolyte's long-term operation. They could also comprise an insignificant amount of carbon and oxygen. The microhard-

ness of those coatings was 600–750 kgf/mm^2. Those two groups of coatings were further studied as the types of surfaces with low (the first case) and high (the second case) contents of tungsten.

The anodic treatment of the obtained surfaces was accomplished using a recessed rotating disk electrode (RRDE) [16] (Fig. 2). The specimens with cobalt-tungsten coatings were flush-mounted into a fluoro-plastic cartridge and fixed on the RDE shaft. In order to obtain the treated and untreated surfaces on one and the same specimen (on its different sections) and to measure these surfaces ~30 μm thick, self-adhesive polymer covers were used. The covers were made using the cutting plotter method from an ORACAL self-adhesive polymer film and were then applied to the coating surface. The cover had the form of a ring with a 20-mm external and a 3-mm internal diameter (Fig. 2). Hence, the site of the coating available for the anode treatment was a 3-mm-diameter circle (Fig. 2). Since, the thickness of the cover was comparable to that of the dissolved layer of the coating, this variant of the RDE can be regarded as an RRDE [16, 17]. The rotation rate varied from 0 to 2550 rot/min.

The described variant of the RRDE was used for the polarization measurements (potentiodynamic and galvanodynamic) and the determination of the current efficiency. After the anode treatment, the morphology and elemental composition of the surface (SEM/EDX, TESCAN, INCA EDX) (GB) were defined along with the roughness and the profile of the manufactured surfaces and of the etched cavities (Surtonic-25) (Taylor Hobson, GB), as well as the microhardness (PMT-3, Berkovich and Vickers indenters were used, and the load varied from 20 to 100 gr). The change in the microhardness was estimated versus the initial microhardness measured on the nontreated surface using the values $(HV^x - HV^n)/HV^n(5)$, where HV^n and HV^x are the microhardness values measured prior to and after the anodic treatment.

The anode microtreatment was carried out in a galvanostatic mode at different current densities and different values of the passed charge. Under the ECM and electrochemical micromachining conditions, the attaining of the anode limiting currents, which affect the current efficiency of the dissolution, the process localization (the treatment accuracy), and the surface roughness, is known to play a key role [17–22]. In this study, a preset current density of the treatment was defined depending on the density of the anode limiting current i_{lim}, and it varied from 0.1 i_{lim} to 3 i_{lim}.

The treatment time was selected so that the etch depth could vary from 5 to 15 μm. In the case of the treatment of strengthening chromium coatings, the value of the removed layer often played a defining role in reaching any particular indices that characterize the quality of the surface layer [2, 3].

Both a constant and a pulsed current were used for the microtreatment. During a constant pulse duration
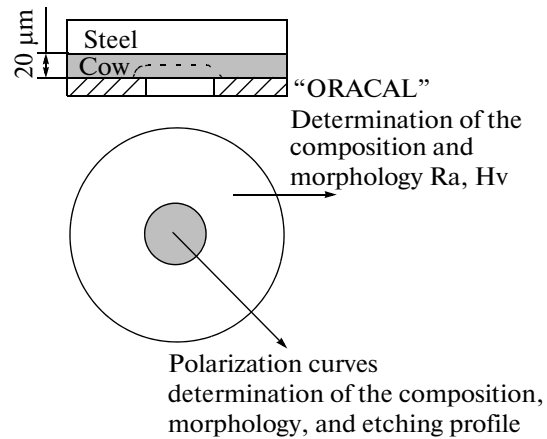

Fig. 2. The RRDE scheme.

of 0.5 s and the interval duration of 1 s, the value of the current density in a pulse varied, with its specific magnitude being determined by the value of the anode limiting current.

Two types of electrolytes were used for the treatment, namely, sodium nitrate solutions with different concentrations and a nitrate-alkaline solution (2 M $NaNO_3$ + 0.5 M KOH). This choice was justified by the use of these solutions for the treatment of the alloys based on the iron-group metals and the cobalt-tungsten solid alloys under the ECM conditions [18, 19]. Nitrate solutions are known to be used more intensively in the ECM of the iron-group metals and also the alloys on their basis. At the same time, tungsten dissolves only in the alkaline solutions, and, for the cobalt-tungsten alloys, nitrate-alkaline solutions are mainly used [18, 19].

The polarization measurements and the measurements of the current efficiency were carried out using both the above RRDE and RDE. As will be shown below, the minimal roughness of the treated surface was attained using high current densities (several amperes per square centimeter). Taking this into account, to decrease the ohmic constituent of the measured potentials, the polarization measurements must be performed on a relatively small electrode surface and with the maximum proximity of Lungin's capillary to it. Therefore, the RRDE was used for the measurements, and the potentials were measured using a thin Lungin's capillary (with an external diameter of ~100 μm), which was brought close to the melting surface with the distance being approximately equal to the capillary diameter (see also [18, 19, 23]). The current density–potential dependences were registered in a potentiodynamic mode (the scanning rate of the potential was 100 mV/s) from a stationary potential of the electrode until reaching the anode limiting currents and the transition to thermokinetic instability (TKI) [22–25]. A saturated Ag/AgCl electrode was used as a reference electrode, and all the val-
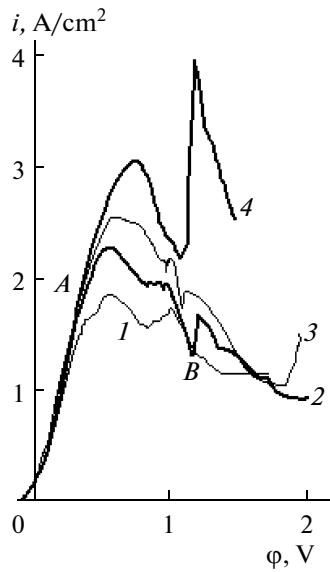
Fig. 3. Polarization curves obtained in 2 M of NaNO₃ at the following RDE rotation speeds, rpm: *1* is 280, *2* is 570, *3* is 1000, and *4* is 2200. 6 % W *A* is the region of the active dissolution, *B* is the region of the salt passivation.
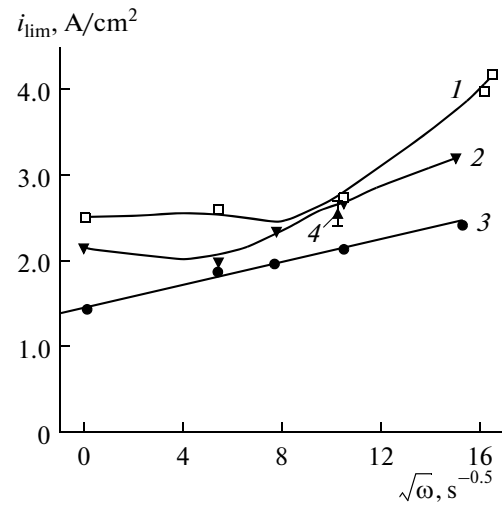
Fig. 4. The effect of the RDE rotation speed on the value of the anode limiting current during the dissolution of the coatings with low (*1−3*) and high (*4*) W contents in a nitrate solution with a concentration, mol/l, of the following: *1* is (1), *2* is (2, 4), and *4* is (3).

ues of the potentials stated below are presented with respect to this reference electrode.

The galvanostatic mode of removal was also used (the rate of the current change was 20 mA/s). Since the micromachining was mainly performed in a galvanostatic mode, the study of the dependence of the potential on the time was carried out (fixing the φ−τ curves) at different current densities and different ratios between the i and i_{lim} current densities. A PI-50-1 potentiostat (the current maximum is 1.1 A) was used as a galvanostat.

The current efficiency was determined using the RDE in a galvanostatic mode measuring the weight losses at i = const. The measurements were performed at different values of the i/i_{lim} ratio (0.1−3). The electrochemical equivalent was calculated taking into account the condition of the cobalt dissolution in the form of Co(II), and tungsten in with the oxidation level of +6 (with the equivalent equaling 0.311 mg/C and it being independent of the tungsten content in the alloy to an accuracy of 1%). In some cases (at higher current densities), a galvanostat of a domestic construction was used with the maximum current of 10 A.

RESULTS AND DISCUSSION

The Anodic Dissolution of Polycrystalline Coatings with a Small Content of Tungsten in a Nitrate Solution

Figure 3 shows a series of potentiodynamic polarization curves of the anodic dissolution of polycrystalline coatings in a nitrate solution at different speeds of the electrode's rotation. At least two regions of dissolution can be distinguished (i.e., one is a region of

active dissolution and the other is a passivity region), which depends on the hydrodynamic conditions. The region of the active dissolution starts almost from the stationary potential (Fig. 3). After reaching the current densities of 2−3 A/cm², the rate limitations of the dissolution appear to correlate with the formation of a passive layer on the surface (the current density decreases with the potential increase Fig. 3)). Similar limitations in the systems with the anodic dissolution are known fairly well [18−20, 22−25].

They result from the so called "salt passivity," and namely due to reaching a surface concentration of the products of dissolution in the electrolyte solution in which the dissolution occurs. Apparently, the more intense the hydrodynamic mode, the higher the current densities must be to reach the anode limiting current, prior to attaining which the active dissolution may occur. Since the passive salt (salt-oxide) layer is formed with the anion solution being involved, the higher its concentration, the lower the value of the limiting current.

This is confirmed by the results of Fig. 4, which shows (a) an increase of the i_{lim} value with increasing $\sqrt{\omega}$, as the RDE theory requires [26], and (b) a decrease of its value with an increase of the nitrate concentration.

However, two peculiarities are characteristic for the results of Fig 4, i.e., (a) the current density can grow with a decrease of the RDE rotation speed; (b) under the conditions of the linearity of the dependence of i_{lim} on $\sqrt{\omega}$, this dependence cannot be extrapolated to the beginning of the coordinates. These peculiarities were
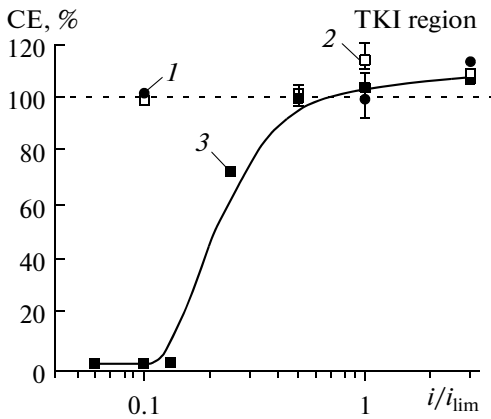
Fig. 5. The dependence of the current efficiency of dissolution in an electrolyte (2 M $NaNO_3$ (1, 2), 2M $NaNO_3$ + 0.5 M KOH (3)) at the tungsten concentration in the alloy of 6% (1) and 22−25% (2, 3) on the current density.
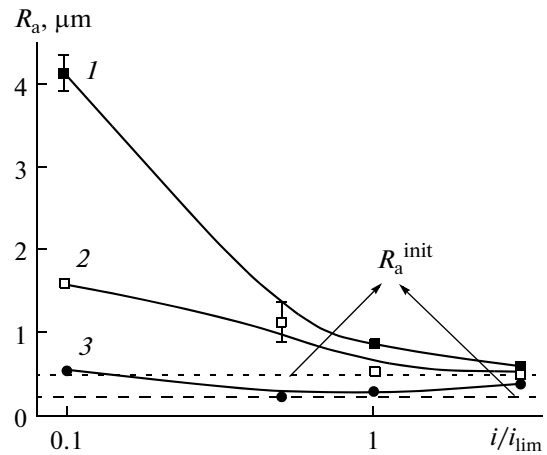

Fig. 6. The dependence of the surface roughness on the current density of dissolution in 2M $NaNO_3$ (1, 3) and 2 M $NaNO_3$ + 0.5 M KOH (2) at a tungsten content in the alloy of 22−25% (1, 2) and 6% (3). The dashed line shows the mean roughness values after the electrodeposition.
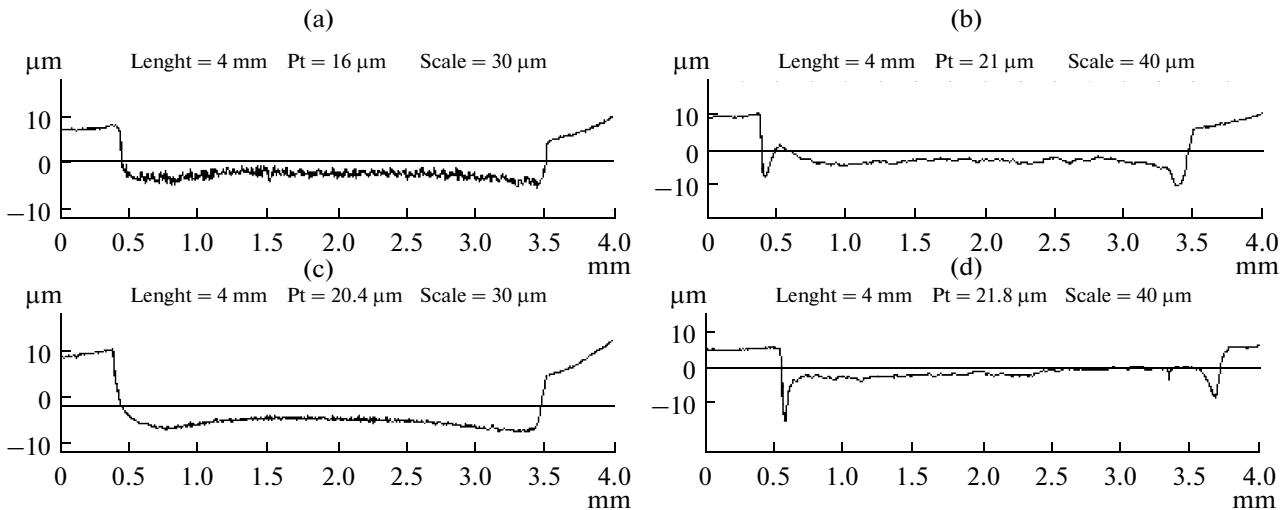

Fig. 7. Profilograms of the surface after the dissolution in 2 M $NaNO_3$ of polycrystalline coatings with a low content of tungsten at the current densities of i/i_{lim}: (a) 0.1; (b) 0.5; (c) 1.0; (d) 3.0.

not studied in detail. However, they can be assumed, on the one hand, to be a consequence of the mixed kinetics of the dissolution process and, on the other hand, to be a result of the macroscopic nonuniformity of this process (see [27] for more details). In [27], using the example of the iron dissolution in a nitrate solution, it was shown that similar peculiarities can be observed under the conditions of the formation of salt films on the dissolving surface.

Considering the aforementioned, the appearance of passivity upon reaching i_{lim} in this case can be regarded to result from the formation of a salt (or salt-oxide) layer from the dissolution products.

The current efficiency of the anode process (Fig. 5) up to the i_{lim} values is 100%; however, at $i > i_{lim}$, it is markedly higher than 100%, and this excess decisively goes beyond the limits of the measurements error (111−112%).

Figure 6 shows the Ra values of the manufactured surfaces, and Fig. 7 displays the surface profiles after the dissolution. One can see that the minimum roughness is attained under the conditions of dissolution when the current density is close to i_{lim} (Fig. 7). On the other hand, under these conditions, a characteristic profile error is observed consisting in the increase of the etch rate in the area of contact with the insulation (Fig. 7). The latter effect confirms the presence of the concen-
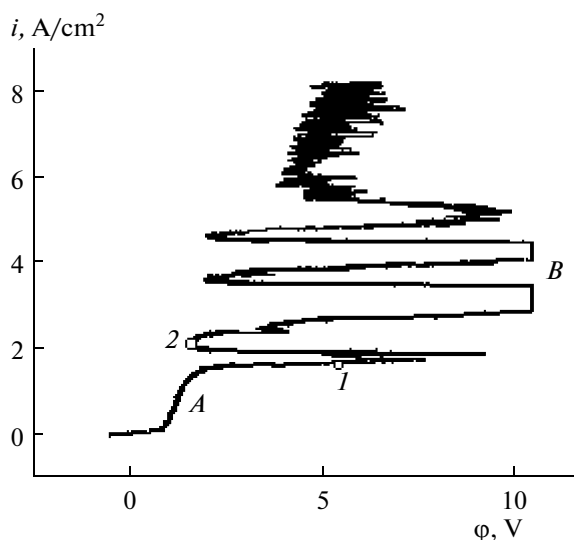
Fig. 8. Galvanodynamic curve of the dissolution of the alloy with a high content of tungsten in 2M NaNO$_3$ (the rate of the scan is 20 mA/s). Points *1* and *2* correspond to the conditions at which the surface analysis was performed (see also Fig. 10).

tration limitations in the etch rates. This error is known to be the consequence of the turbulent vortices formation in the region of contact with the insulation.

From the viewpoint of determining the modes for the practical use of micromachining of such coatings, it seems evident that it must be performed at $i \sim 0.5\, i_{lim}$. It is under these conditions that the surface's minimal roughness is observed, being similar to that prior to the micromachining (Fig. 6), but the observed error fails to be registered (Fig. 7).

The Anodic Dissolution of Nanocrystalline (Amorphous) Coatings in Nitrate Solutions

The dissolution patterns for coatings with a high tungsten content in the nitrate solution (2 M NaNO$_3$) are the same as for the coatings with low concentration; however, significant peculiarities yet exist. In particular, at high current densities, an oscillatory process is registered (Fig. 8). Under the conditions of a stationary process (at $i < i_{lim}$), the dissolution occurs at a higher overvoltage versus the dissolution of coatings with a low W content (the overvoltage increases by about 1 V (region A in Fig. 8); compare with the corresponding dissolution region in Fig. 3). Although the current efficiency at $i < i_{lim}$ is constant and equals 100% (Fig. 5), the same as for the dissolution of polycrystalline coatings in this region, a substantial non-uniformity in the dissolution rates and pitting formations with notable sizes occur, which leads to the manufacturing of a surface with a high level of roughness (Figs. 6, 9).

A transition to the oscillatory process at high current densities can result from a transition to the mode of thermokinetic instability (TKI). The transition to the TKI mode is known to occur upon reaching a critical value of the surface temperature T_s^{cr} [22, p. 40]:

$$T_s^{cr} = \frac{E_a}{2R}\left[1 - \sqrt{1 - \frac{4RT_0}{E_a}}\right], \qquad (1)$$

where E_a is the energy of activation of the dissolution process, and T_0 is the temperature in the bulk of the solution. One can see from (1) that, at a preset bulk temperature, the critical surface temperature of the transition to the TKI is a function of only the activa-
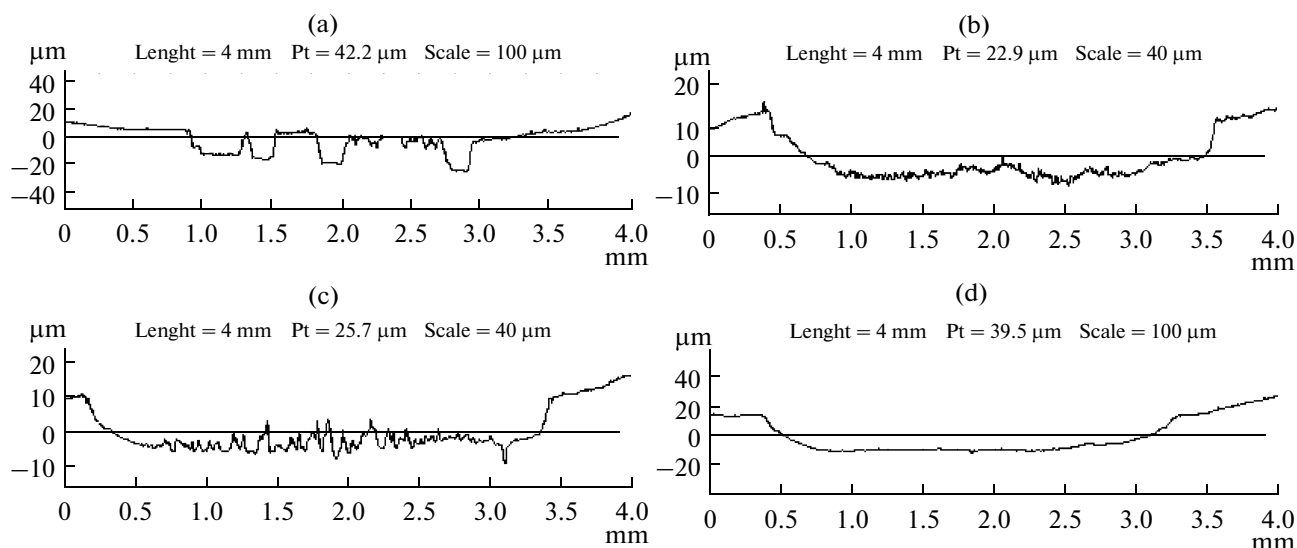

Fig. 9. Profilograms of the surface after the dissolution in 2M NaNO$_3$ of polycrystalline coatings with a high content of tungsten at the current densities of i/i_{lim}: (a) 0.1; (b) 0.5; (c) 1.0; (d) 3.0.

tion energy of the process. For the conditions of this experiment, it is possible to estimate the T_s^{cr} and, hence, the E_a values.

Taking into account that the value of the temperature increment of the surface temperature compared to the bulk temperature can be estimated according to (2) (the Peltier effect at a potential level of ~10 V (Fig. 8) can be neglected), we can obtain (see also [22, p. 36]):

$$\Delta T_s = T_s - T_0 = \frac{i\eta}{\alpha}, \qquad (2)$$

where η is the overvoltage at the preset current density i, and α is the coefficient of the heat transfer from the surface to the solution. Considering that, for the RDE and the speed of rotation of 1000 rot/min, this value is 0.56 W/cm^2 deg (for water) [22, p. 37], we obtain that ΔT_s^{cr} according to (2) is 35°C (at $i = 2$ A/cm^2 and $\eta \sim$ 10 V, Fig. 8). This means, according to (1), that, at a bulk temperature of 20°C, the transition to the thermokinetic instability upon such a critical temperature difference can be observed provided the activation energy is ~30 kJ/mol, which is a typical value for such kinds of processes [22, 24].

Thus, the hypothesis that the transition to the oscillatory process is connected with the transition to the TKI agrees with the experimental results.

However, as is shown, in particular, in [25], the transition to the TKI during the anodic dissolution must be accompanied by the disintegration of the surface film with the heat release and its partial disintegration owning to a "thermal explosion," i.e., the partial transition of the anode material into the solution in the form of solid particles.

This is confirmed by the data of Fig. 5, from which it follows that, at $i > i_{lim}$, the current efficiency always exceeds 100%, which should be regarded as indirect evidence of the disintegration of part of the material at the anodic dissolution under these conditions.

After the process terminated, the surface was analyzed at points 1 and 2 (Fig. 8) by scanning electron microscopy combined with the elemental analysis. The results are shown in Fig. 10. Both sodium and oxygen were found to be contained in the film composition prior to its disintegration (Fig. 10b) along with a considerably higher W content compared to the initial surface (Fig. 10a). After the destruction of the salt-oxide layer (point 2, Fig. 8), an oxidized surface forms with the concentration ratio of cobalt and tungsten close to that observed prior to the dissolution (Fig. 10c).

Thus, the oscillation process of dissolution represents the periodic formation and destruction of the salt-oxide surface layer with the partial disintegration of the electrode products into the electrolyte bulk.

Under the TKI conditions, the roughness is found to be minimal (Fig. 9).

The results shown in Fig. 11 also appear to be in favor of this method for the material removal (micromachining). It is clear that the oscillation frequency grows with the current density increase. It decreases upon an increase of the intensity of the removal of the dissolution products using hydrodynamics (Fig. 11). In Fig. 11, region A is the region of formation of the salt-oxide layer, region B is the TKI region, and region C is the transition to the substrate dissolution.

Thus, such coatings can be efficiently treated using micromachining in simple nitrate solutions, however, only provided that high current densities are present (i.e., in the mode of thermokinetic instability). In this situation, the specific etch errors that result from the turbulent vortices in the region of the contact with the insulation are absent.

Although the hydrodynamic effect on the values of the anode limiting currents during the treatment of such coatings was not studied in detail, the data in Fig. 4 show that they (the anode limiting currents) are close to those observed during the treatment of the cobalt films with a low content of tungsten.

The Anodic Treatment in a Nitrate-Alkaline Solution

From the potentiodynamic curves (Fig. 12) obtained at different RRDE speeds of rotation, it follows that, in this case, a transition to the salt passivity and an effect of the hydrodynamics on the current density of this transition also take place. However, a specific region is observed on polarization curve A of this solution. In this region, the limiting currents are reached (at the current densities lower than those in the formation of the salt passivity), which depend on the rate of mixing.

This region was not studied in detail; however, its connection with reaching a zero surface concentration of hydroxyl ions cannot be ruled out. Indeed, in accordance with [10], nanocrystalline cobalt-tungsten coatings contain tungsten clusters aggregated along the boundaries of crystallite grains. Since tungsten is dissolved only in an alkali, during its dissolution, limiting currents are commonly observed, which depend on the mixing rate and the alkaline concentration [8, 19, 22]. Region A in Fig. 12 obviously corresponds to this process. If so, this can both indirectly indicate the validity of [10] and lead to surface passivation upon the dissolution in this electrolyte after the tungsten cluster dissolution in an alkali from the surface layer.

Indeed, the dissolution current efficiency in this region of current densities is close to zero (Fig. 5), but pitting dissolution partially takes place (Fig. 13 a). The current efficiency in region C grows (Fig. 5), and in the TKI region (region B) it (the same as for the dissolution in the nitrate solution without an alkali) exceeds
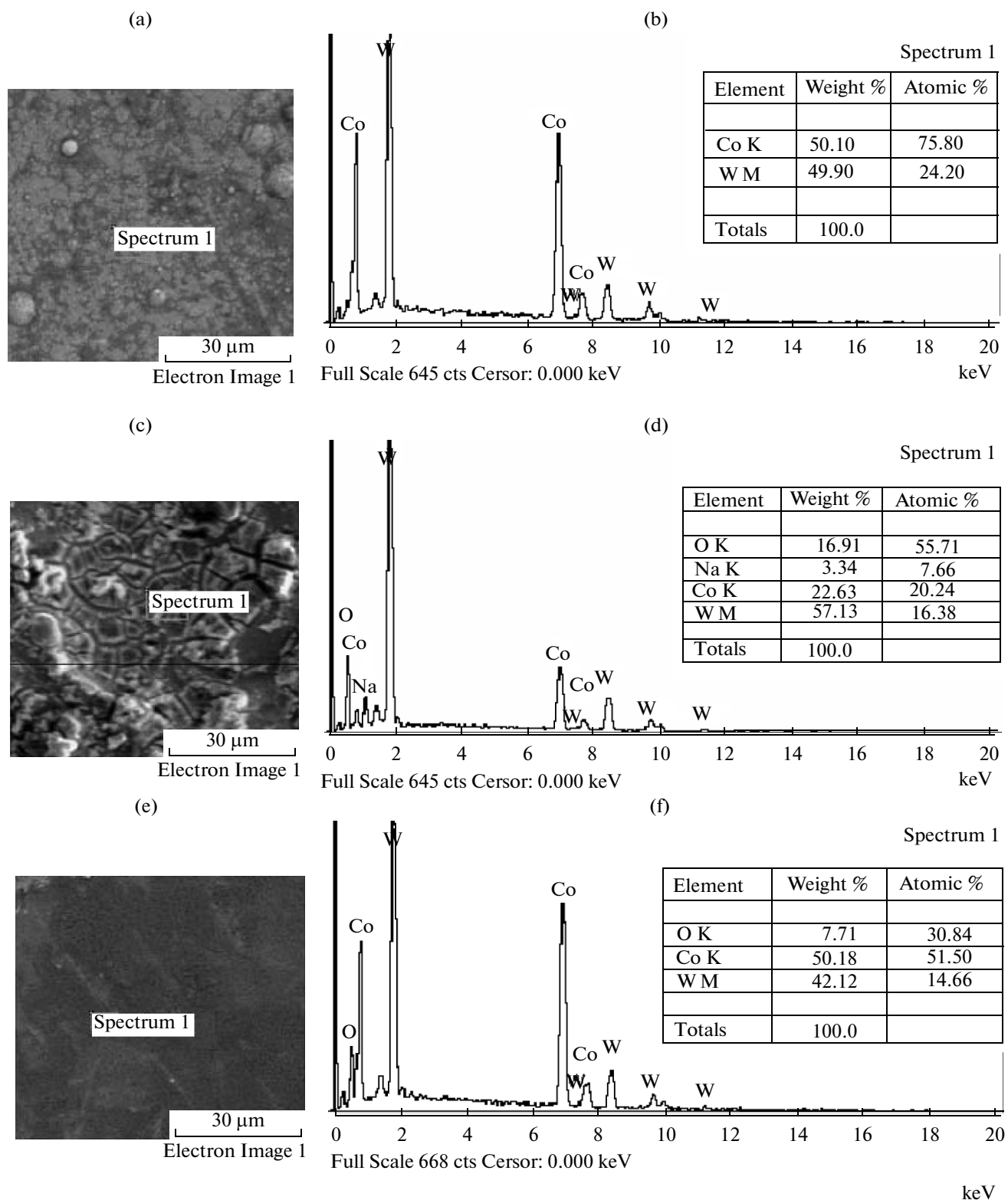
(a)

(b)

Spectrum 1

Element	Weight %	Atomic %
Co K	50.10	75.80
W M	49.90	24.20
Totals	100.0	

Co

W

Co

Co W
W W
W

30 μm
Electron Image 1

Full Scale 645 cts Cersor: 0.000 keV

keV

(c)

(d)

Spectrum 1

Element	Weight %	Atomic %
O K	16.91	55.71
Na K	3.34	7.66
Co K	22.63	20.24
W M	57.13	16.38
Totals	100.0	

Spectrum 1

W

O
Co
Na

Co
Co W
W W W

30 μm
Electron Image 1

Full Scale 645 cts Cersor: 0.000 keV

keV

(e)

(f)

Spectrum 1

Element	Weight %	Atomic %
O K	7.71	30.84
Co K	50.18	51.50
W M	42.12	14.66
Totals	100.0	

Spectrum 1

W

Co

Co

O

Co W
W W
W W

30 μm
Electron Image 1

Full Scale 668 cts Cersor: 0.000 keV

keV

Fig. 10. Surface morphology of the coating prior to the treatment (a) and after stopping the process at point *1* (Fig. 8) (c) and point *2* (Fig. 8) (e) and the EDX spectra of the corresponding surfaces (b, d, f).
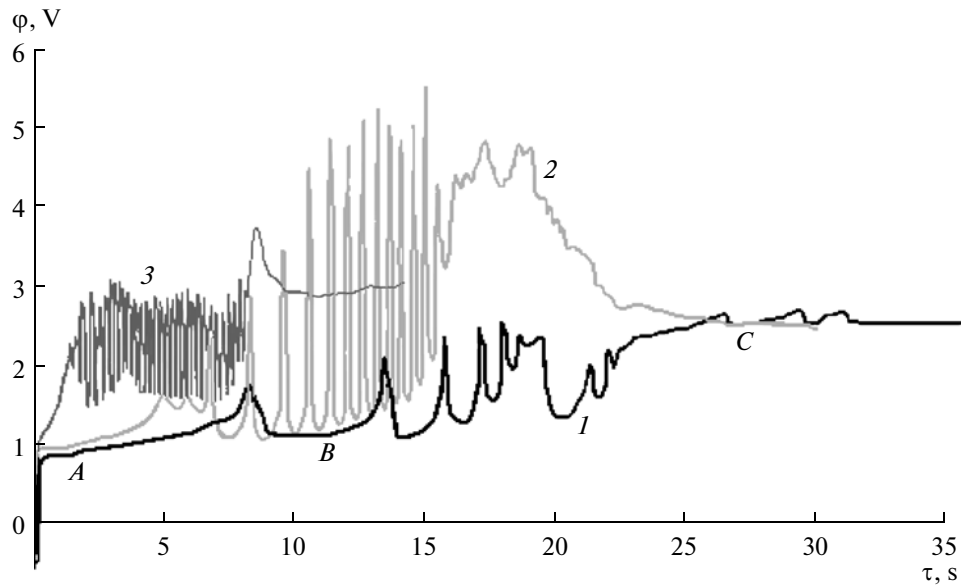
Fig. 11. The dependence of the potential on the time upon the micromachining of the coating with a high content of W in 2 M NaNO$_3$ and at $i = i_{lim}$ (*1*), $i = 1.4$ A/cm^2 without rotation (*2*), and $i = 2i_{lim}$ (*3*).

100%, which attests to the partial disintegration of the surface layer during the anode treatment (Fig. 5).

During the transition to the TKI, a minimal surface roughness is registered (Fig. 6), and the forming profile contains no specific errors determined by the presence of turbulent vertices in the region of contact with the insulation (Figs. 13 c, 13 d). The oscillatory process occurs only at the current densities that either exceed or equal i_{lim} (Fig. 14). At lower current densities, the steadiness of the electrode process is detected, which indicates that the forming film has an electron conductivity.

Thus, when using the nitrate-alkaline solutions, the treatment with minimal roughness and high current efficiency is possible only under the TKI conditions. Moreover, unlike the treatment in nitrates, an increasing dependency of the current efficiency on the current density is registered, which, under the ECM conditions, always provides high localization of the dissolution process. In addition, as was shown, e.g., in [17], the maximum localization of the anodic dissolution process at partial isolation of the surface with covers, which is correlated with a decrease of etching under the insulation, is observed precisely under the conditions of reaching the anode limiting currents that result from salt passivation.

The Change of the Surface Microhardness after the Treatment

Due to the anodic dissolution and micromachining, a new surface is created whose functional properties differ greatly from those of the initial surface. In this chapter, we present the results of changes in the

microhardness during the etching process and describe the possible methods for the microhardness control. As a parameter for the estimation of the microhardness's change, we used a relative value, i.e., the difference between the microhardness values prior to and after the etching (on one and the same specimen) related to the microhardness of the initial surface.
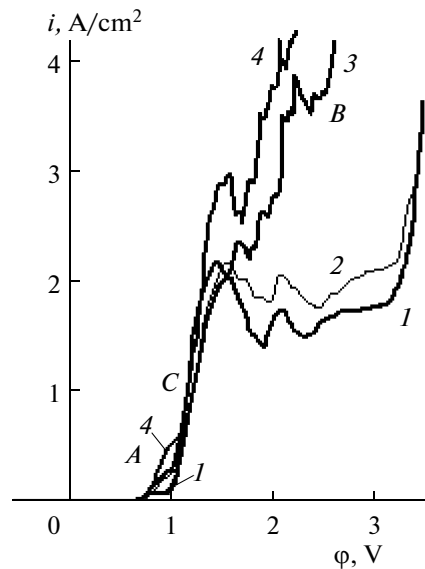

Fig. 12. Potentiodynamic polarization curves for the coating with a high W content manufactured in 2M NaNO$_3$ + 0.5 M KOH at the following RDE rotation speeds, rot/min: *1* is 280, *2* is 1000, *3* is 1500, and *4* is 2260.

(a)

μm　　　Lenght = 4 mm　Pt = 28.2 μm　Scale = 50 μm

(b)

μm　　　Lenght = 4 mm　Pt = 39.3 μm　Scale = 100 μm

(c)

μm　　　Lenght = 4 mm　Pt = 41.2 μm　Scale = 100 μm

(d)
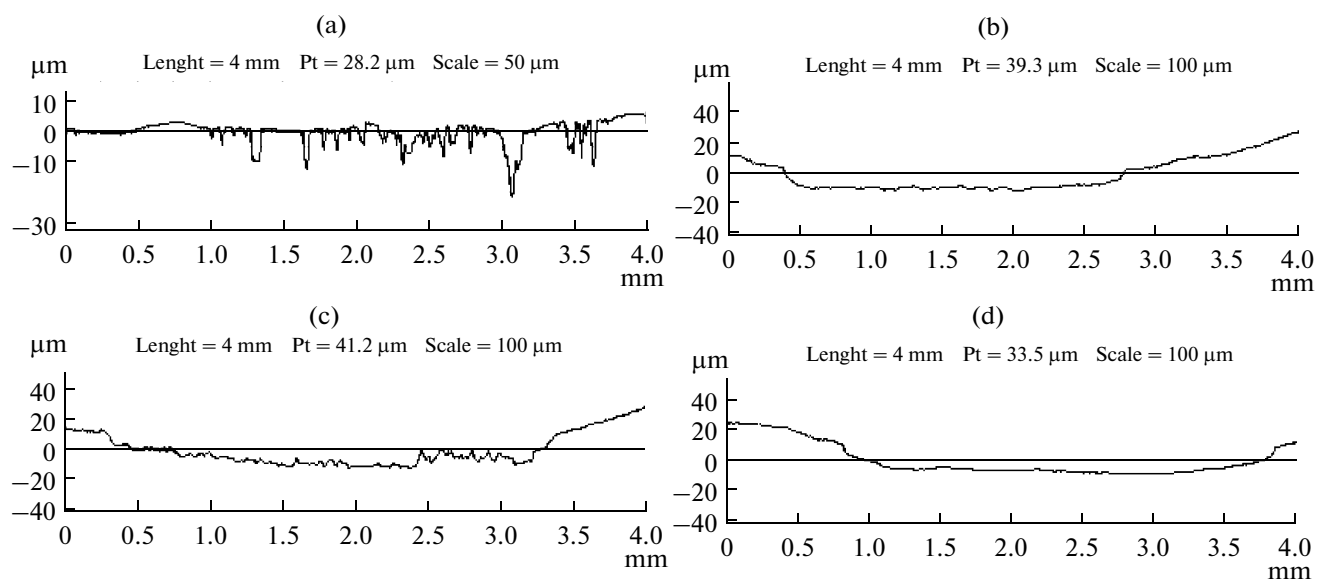
μm　　　Lenght = 4 mm　Pt = 33.5 μm　Scale = 100 μm

Fig. 13. Profilograms of the surface after the dissolution in 2M $NaNO_3$ + 0.5M KOH of coatings with a high W content at the following current densities, i/i_{lim}: (a) 0.1, (b) 0.5, (c) 1.0, and (d) 3.
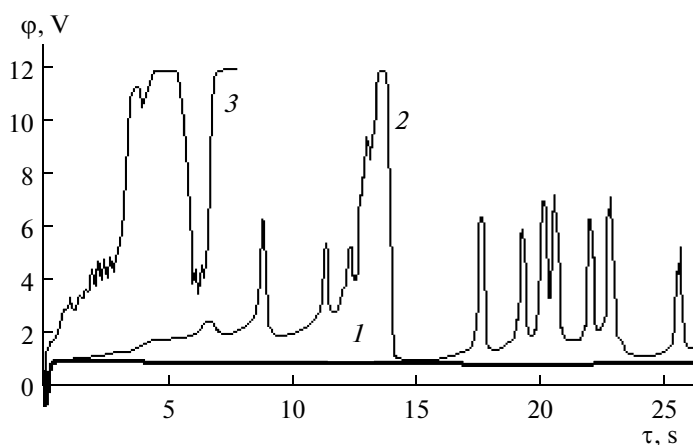
φ, V

τ, s

Fig. 14. The potential's dependence on the time upon the dissolution of a coating with a high W content in 2M $NaNO_3$ + 0.5M KOH at $i = 0.1\, i_{lim}$ (*1*), $i = i_{lim}$ (*2*), and $i = 3i_{lim}$ (*3*).

As is seen, during the treatment of the surfaces with a low tungsten content, the surface microhardness may even increase after etching (Fig. 15), which is apparently connected with the surface oxidation; however, it decreases after etching in the modes that correspond to the TKI. A still sharper decrease in the microhardness is detected during the treatment of surfaces with a high W content and a higher initial microhardness; a more abrupt decrease in the microhardness is observed at $i > i_{lim}$ (almost twofold at $i = 3\, i_{lim}$ (Fig. 15)). This is assumed to be correlated with the partial involvement of the products of disintegration of the surface film in the process of the dissolution and thus forming the surface.

With a thickness increase of the removed layer, the degree of the microhardness decrease grows (Fig. 16). The observed decrease cannot be the outcome of the inaccuracy in the measurements, since using different loads led to close HV values that were measured.

Assuming that the surface formed in the treatment process (among other factors) owning to the participation of the products of disintegration in this process, the use of a pulsed current can lead to the conservation of its properties, since, during a pause, these products can be removed from the surface by the electrolyte flow.

Indeed, the microhardness value is almost conserved (Fig. 16, curve *3*) owning to a pulsed current
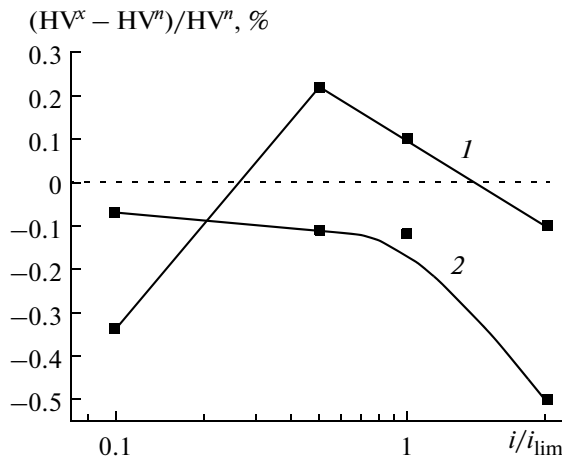
$(HV^x - HV^n)/HV^n$, %

$(HV^x - HV^n)/HV^n$, %

Fig. 15. The current density's effect on the relative change in the microhardness after the 10-μm-depth etching of the coatings with a low (*1*) and high (*2*) W content in the coating during the anodic dissolution in 2M NaNO$_3$. The mean value of the microhardness (kG/mm^2) prior to the micromachining of the coatings with a low content of W (it was 360 and with a high content, 600).
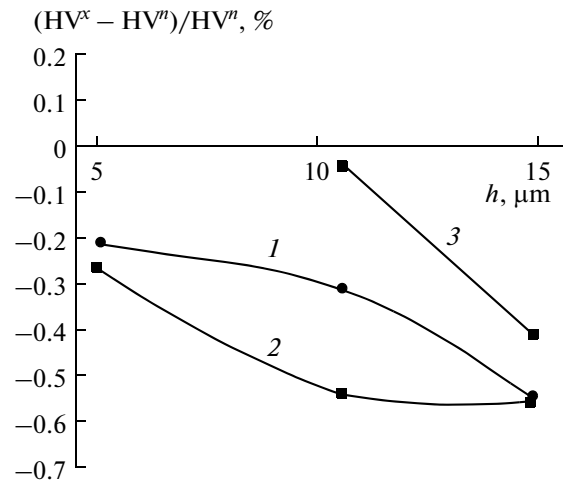
Fig. 16. The effect of the etch depth on the degree of the surface disordering when the alloy with a high W content is treated in 2M NaNO$_3$ by a constant current i_{lim} (*1*), a pulse current with a current density of 3 i_{lim} (*2*) in a pulse, and a pulse current with a current density of i_{lim} (*3*) in a pulse. The microhardness of the nontreated surface was in the range of 600–650 kG/mm^2.

with a pulse duration of 0.5 s, a pause duration of 1 s, and the current density in a pulse equaling the density of the anodic limiting current upon etching for a depth that is half the thickness of the coating. At the same time, using a pulsed current with the same values of the durations of the pulses and a pause but at a current density in the pulse of 3 i_{lim} led to an increase in the degree of the microhardness decrease even versus a constant current. That is, at the same average current density under the conditions of the pulsed treatment at high i, the degree of the microhardness decrease grows (Fig. 16, curve *2*). This is another argument in favor of the fact that, with a current density increase (higher than the anodic limiting), the degree of disintegration of the surface films grows and, hence, the microhardness of the newly created layer decreases, which is confirmed by the data shown in Fig. 17.

It is evident that the treatment in the modes which correspond to the region of the anodic limiting current should be first of all considered as the optimal conditions. In this case, a minimal undercutting occurs under the insulation (provided the insulating covers are used in the micromachining [17]), the surface roughness is minimal, and the conservation of the surface layer's microhardness is possible upon the pulsed treatment.

This inference is supported still more upon the treatment in a nitrate-alkaline solution (Fig. 18). In this case, the conservation of the microhardness is possible after the dissolution using even a constant current.

CONCLUSIONS

The results of this study show that the modes corresponding to thermokinetic instability (TKI) are efficient when used under the conditions of electrochemical micromachining of the CoW hardening coatings. In this case, the surface roughness after the treatment is minimal and the current efficiency exceeds 100% owing to the disintegration of the surface film and the partial transition of the coating material in a solid state into the solution. A way for the removal of the coating
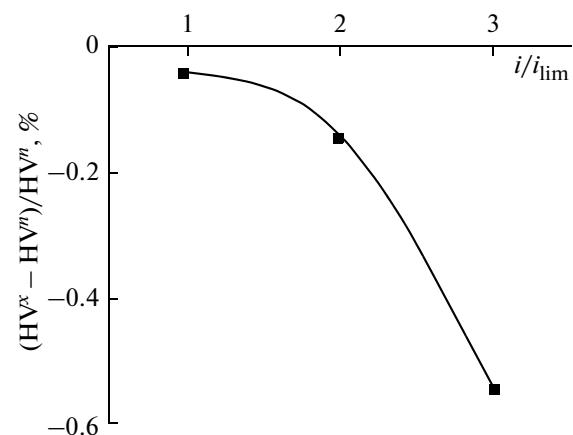

Fig. 17. The current density effect in a pulse depending on the degree of the surface disordering after the dissolution of a coating with a high content of tungsten for a depth of 10 μm by a pulse current in 2M NaNO$_3$. The microhardness of the nontreated surface was in the range of 600–650 kG/mm^2.
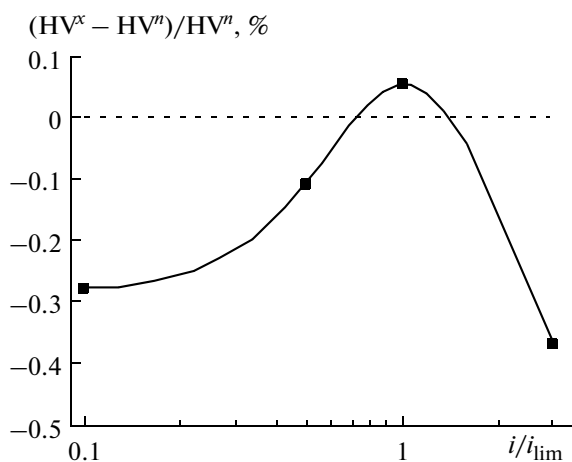
$(HV^x - HV^n)/HV^n$, %

Fig. 18. The effect of the current density on the relative change in the surface's microhardness after the dissolution of a coating with a high W content for a 10-μm depth by a constant current in 2M $NaNO_3$ + 0.5M KOH. The average microhardness of the nontreated surface was 750 kG/mm^2.

material under the TKI conditions based on the periodic formation of a salt-oxide surface film and its destruction due to a thermal explosion is proposed.

The change in the profile after micromachining in different electrolytes both for polycrystalline (the coatings with the W content of 5–6 at %) and nanocrystalline surfaces (22–25 at %) was examined experimentally, and it was shown that, during the dissolution of the first-type coatings in the nitrate solutions in the modes close to the reaching of the anodic limiting currents that result from the salt passivation, a specific error of the profile is detected that is correlated with an increase of the dissolution rate in the region of the contact with the insulation and is connected with the presence of turbulent vertices. The latter fails to be observed upon the treatment of nanocrystalline coatings in the nitrate and nitrate-alkaline solutions.

The experimental results of the study of hardening (softening) the surface after treatment under different conditions allow us to infer that the products of the dissolution and disintegration of the surface layers can participate in the formation of surface layers after the treatment. The proposed modes of micromachining using constant and pulsed currents make it possible to partially control this process.

ACKNOWLEDGMENTS

REFERENCES

1. Benikov, V.S., Saushkin, B.P., and Dikusar, A.I., The Analysis of the Technologies for Manufacturing Surface Downward Shifts with a Depth of 10–20 μm, *Uprochnyayushchie Tekhnol. Pokrytiya*, 2008, no. 6, pp. 48–53.

2. Silkin, S.A., Petrenko, V.I., and Dikusar, A.I., Anodic Dissolution of Electrochemical Chromium Coatings in Electrolytes for Electrochemical Machining. The Dissolution Rate and Surface Roughness, *Surf. Eng. Appl. Electrochem.*, 2010, vol. 46, no. 1, pp. 1–8.

3. Silkin, S.A., Petrenko, V.I., and Dukusar, A.I., Surface Softening of the Electrolytic Chromium Coatings after Their Anodic Dissolution in Chloride and Nitrate Solutions, *Izv. Vyssh. Uchebn. Zaved., Khim. Khim. Tekhnol.*, 2011, vol. 54, no. 11, pp. 51–57.

4. Brenner, A., *Electrodeposition of Alloys*, New York: Acad. Press Inc., 1963.

5. Vas'ko, A.T., *Elektrochimiya molibdena i vol'frama* (Electrochemistry of Molybdenum and Tungstem), Kiev: Naukova Dumka, 1977.

6. Eliaz, N. and Gileady, E., Induced Codeposition of Alloys of Tungsten, Molybdenum and Rhenium with Transition Metals, *Mod. Aspects of Electrochem.*, 2008, no. 42, pp. 191–301.

7. Weston, D.P., Shipway, P.H., Harris, S.J., and Cheng, M.K., Friction and Sliding Wear Behavior of Electrodeposited Cobalt and Cobalt-Tungsten Alloy Coatings for Replacement of Electrodeposited Chromium, *Wear*, 2009, no. 267, pp. 934–943.

8. Tsyntsaru, N., Belevskii, S., Dikusar, A., and Celis, J.-P., Tribological Behavior of Electrodeposited Cobalt-Tungsten Coatings: Dependence on Current Parameters, *Trans. Inst. Metal Finnish.*, 2008, no 86, pp. 301–307.

9. Tsyntsaru, N., Dikusar, A., Cesiulis, H., Celis, J.-P., Bobanova, J., Sidelinikova, S., Belevsky, S., Yapontseva, Yu., Bersirova, O., and Kublanovsky, V., Tribological and Corrosion Properties of Electrochemical Coatings on the Base of Cobalt and Iron Superalloys, *Powder Metal Metal. Ceram.*, 2009, nos. 7–8, pp. 66–78.

10. Weston, D.P., Harris, S.J., Shipway, P.H., Weston, N.J., Yap, G.N., Establishing Relationships between Bath Chemistry, Electrtodeposition and Microstrructure of CoW Alloy Coatings Produced from Gluconate Bath, *Electrochem. Acta*, 2010, vol. 55, pp. 5695–5708.

11. Cesiulis, H. and Budreika, A., Hydrogen Evolution and corrosion of W and Mo Alloys with Co and Ni, *Physicochem. Mechanics Mater.*, 2010, no. 8, pp. 808–814.

12. Silkin, S.A., Belevskii, S.S., Gradinar', A.S., Petrenko, V.I., Yakovets, I.V., Tsyntsaru, N.I., and Dikusar, A.I., Electrodeposition of Nanocrystalline CoW Coatings from Citrate electrolytes under Controlled Hydrodynamic Conditions. Part 3. The Micro- and Macrodistribution of the Deposition Rates, the Structure and Mechanical Properties, *Surf. Eng. Appl. Electrochem.*, 2010, vol. 46, no. 3, pp. 206–214.

13. Belevskii, S.S., Cesiulis, H., Tsyntsaru, N.I., and Dikusar, A.I., The Role of Mass Transfer in the Formation of the Composition and Structure of CoW Coat-

ings Electrodeposited from the Citrate Solutions, *Surf. Eng. Appl. Electrochem.*, 2010, vol. 46, no. 6, pp. 570−578.

14. Silkin, S.A., Belevskii, S.S., Tsyntsaru, N.I., Shulman, A.I., Shuplyakov, A.N., and Dikusar, A.I., Influence of Long-Term Operation of Electrolytes on the Composition, Morphology and Stress-Strain Properties of Surfaces Produced at Deposition of CoW Coatings from Citrate Solutions, *Surf. Eng. Appl. Electrochem.*, 2009, vol. 45, no. 1, pp. 1−12.

15. Belevskii, S.S., Tsyntsaru, N.I., and Dikusar, A.I., Electrodeposition of Nanocrystalline CoW Coatings from Citrate Eletrolytes under Conditions of Controlled Hydrodynamic II. Electrodeposition Rate and Composition of the Coatings, *Surf. Eng. Appl. Electrochem.*, 2009, vol. 46, no. 2, pp. 91−99.

16. Dinan, T.E., Matlosz, M., and Landolt, D., Experimental Investigation of the Current Distribution on a Recessed Rotating Disk Electrodes, *J. Elechem. Soc.*, 1991, vol. 138, no. 10, pp. 2947−2951.

17. Dikusar, A.I., Redkozubova, O.O., Yushchenko, S.P., Kriksunov, L.B., and Harris, D., Role of Hydrodynamic Conditions in the Distribution of Anodic Dissolution Rates in Cavity Etching Regions during Electrochemical Micromachining of Partially Insulated Surfaces, *Russian J. Electrochem.,* 2003, vol. 39, no. 10, pp. 1073−1077.

18. Davydov, A.D. and Kozak, E*., Vysokoskorostnoe elektrokhimicheskoe formoobrazovanie* (High Rate Electrochemical Forming), Moscow: Nauka, 1990.

19. Dikusar, A.I., Engel'gardt, G.R., Petrenko, V.I., and Petrov, Yu.N., *Elektrodnye protsessy i protsessy perenosa pri elektrokhimicheskoi razmernoi obrabotke metallov* (Electrode Processes and the Transport Processes in Electrochemical Machining of Metals), Kishinev: Shtiintsa, 1983.

20. Landolt, D., Muller, R.H., and Tobias, C.W., *Transport Processes in ECM. Fundamentals of Electrochemical Machining* (Ed. Faust, Ch.L.), Prinston: 1971, pp. 200−226.

21. Datta, M. and Romankiw, L.T., Application of Chemical and Electrochemical Micromachining in the Electronics Industry, *J. Electrochem. Soc.*, 1989, vol. 136, no. 6, pp. 285−292.

22. Dikusar, A.I., Engel'gardt, G.R., and Molin, A.N., *Termokineticheskie yavleniya pri vysokoskorostnykh elektrodnykh protsessakh* (Thermokinetic Phenomena in High Rate Electrode Processes), Kishinev: Shtiintsa, 1989.

23. Engel'gardt, G.R. and Dikusar, A.I., Thermokinetic Instability of Electrode Processes. Part I. Theoretical Analysis, *J. Electroanal. Chem.*, 1986, vol. 207, no. 1, pp. 1−11.

24. Dikusar, A.I., Molin, A.N., Petrenko, V.I., Engel'gardt, G.R., and Mustiatze, A.N., Thermokinetic Instability of Electrode Processes. Part II. Transpassive Dissolution of Copper in Nitrate Solutions, *J. Electroanal. Chem.*, 1986, vol. 207, no. 1, pp. 12−23.

25. Dikusar, A.I., Mustiatze, A.N., and Yuschenko, S.P., The Thermokinetic Instability of the Surface-Covering Layers during High-Rate Anodic Dissolution Controlled by Mass Transfer, *Russ. J. Electrochem.*, 1997, vol. 33, no. 2, pp. 163−172.

26. Pleskov, Yu.V. and Filinovskii, V.Yu., *Vrashchayushchiisya diskovyi elektrod* (Rotating Disk Electrode), Moscow: Nauka, 1972.

27. Dikusar, A.I., Redkozubova, O.O., Yuschenko, S.P., and Yakhova, E.A., Anodic Dissolution of Armco Iron in a Mixed Kinetic Mode: Effect of Macroscopic Heterogeneity, *Russ. J. Electrochem.*, 2002, vol. 38, no. 6, pp. 632−637.

ELECTRICAL PRECISION
TREATMENT OF MATERIALS

Magnetic Models of Cast Amorphous Microwires

S. A. Baranov

Applied Physics Institute, Moldavian Academy of Sciences, ul. Alademiei 5, Kishinev, MD−2028 Moldova
T.G. Shevchenko Transdniestrial State University, ul. 25 Oktyabrya 128, Tiraspol', Moldova
Départament de Génie Phisique, École Polytechnique de Montréal,
C.P. 6079, succ. Centre−ville, Montréal H3C 3A7 (Québec) Canada
e-mail: serghei.baranov@polymtl.ca; baranov@phys.asm.md
Received November 29, 2010

Abstract—A theory of a magnetic domain model for glass-coated amorphous microwires is studied. The obtained theoretical results are confirmed by experiments. Cast glass-coated amorphous microwires with positive magnetostriction have a rectangle hysteresis loop, which is characterized by a coercive-force stable magnitude. The coercive-force magnitude and the fluctuations of this magnitude are of theoretical and practical interest. The theory of the relaxation mechanism of magnetic reversal is constructed. For the more precise comparison of the theory and the experiment, a series of experimental measurements is needed, which are also discussed in the paper.

INTRODUCTION

Bi-stable ferromagnetics are widely used in the field of instrumentation technology and automatic devices. Their features are as follows: they are magnetically reversed by a large Barkhausen jump (GBJ) [1], and, among bi-stable materials, it is possible to find both crystalline and amorphous ones. Independently of the structure, to create bi-stable properties, it is necessary to form a clearly pronounced gradient of the magnetic potential relief; it may be under uniaxial magnetic anisotropy. Earlier, bi-stable elements made of polycrystalline ferromagnetics were manufactured by thermal and mechanical treatment, for example, the well known vicalloy Wiegand wire. For amorphous materials, this problem is solved in a simpler way: by the technology of amorphous wires' formation itself. The needed combinations of magnetic and mechanical properties, which are investigated in the present work, are formed in them.

Since the operating performances of bi-stable elements are determined by the magnetic reversal processes that happen in them, the investigation of these processes makes it possible to reveal the technical parameters of the elements: the EMF (electromotive force) pulse amplitude; the domain nucleation field; the response time, and the performance stability as a function of different factors, such as the magnetic reversal conditions, the alloy's chemical composition, the nonuniformities or cracks presence, etc. One problem is how to stabilize the operation threshold, i.e., to decrease the fluctuations of the domain nucleation field. The existing methods for solving this problem are very complicated and should be modified.

In the present work, there is investigated a cast amorphous glass-coated microwire (CAGCMW) that is characterized by bi-stable properties from the moment of its manufacturing and the required coercive force, limit magnetization, and magnetic permeability.

Since it is possible to investigate single pulses [1], it is possible to study in more detailed the large Barkhausen jump parameters and the mechanism of the magnetic reversal. When the vicalloy was investigated, it was revealed that the switching is performed by two ways: by relaxation and acceleration mechanisms. These two mechanisms have already been discussed when researching the multijump magnetic reversal.

The relaxation mechanism is characterized by a pulse with a steep rise and a low-angle drop, and the acceleration mechanism is characterized by a smooth rise and a steep drop over the second front pulse (for more details, see below).

In the present work, the large Barkhausen jump parameters for the cast amorphous glass-coated microwire are investigated theoretically and experimentally, the magnetic structure of the cast amorphous glass-coated microwire is studied and compared with other wires, and the factors that influence to large Barkhausen jump parameters in the cast amorphous glass-coated microwire are examined. The models of the magnetic structure presented by other scientists are discussed in the paper.
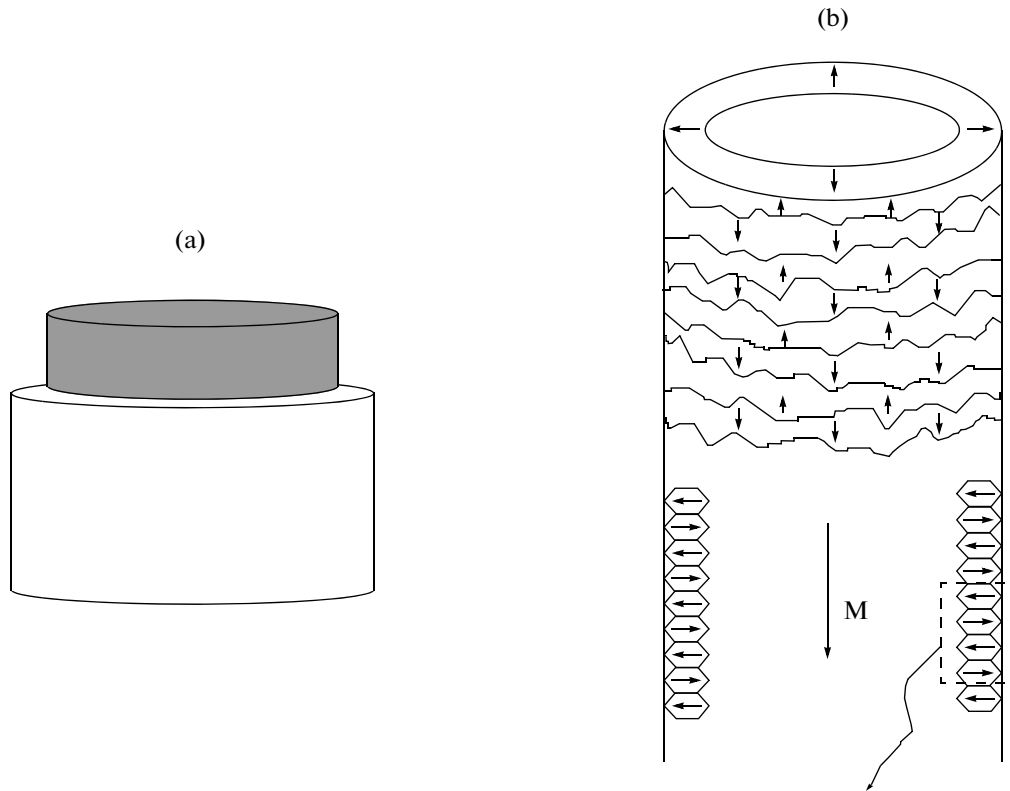
Fig. 1. (a) The domain structure of an infinitely long cast amorphous glass-coated microwire with positive magnetostriction; (b) the domain structure of an Unitika wire with positive magnetostriction [5, 6].

ANALYSIS OF THE MICROWIRE'S MAGNETIC STRUCTURE

The magnetic properties and possible structures of the cast amorphous glass-coated microwires are investigated in [2—20]. In addition to the cast amorphous glass-coated microwires (CAGCMW) technology, there is the technology developed by Unitika Ltd (Unitika technology). The wires manufactured according to Unitika technology (it is also called "in rotating water quenching") are characterized by another magnetic structure and magnetic performance (with respect to the cast amorphous glass-coated microwire), while many magnetic properties are alike. As we know, in the published information, the magnetic structures of the cast amorphous glass-coated microwires and of the wires produced by Unitika Ltd. are not compared, and a part of the present work is devoted to this problem.

The cast amorphous glass-coated microwires with positive magnetostriction and a thread diameter of 1—20 μm are characterized by a rectangle hysteresis loop and by a large Barkhausen jump [2, 7—11] and also by natural ferromagnetic resonance (NFMR) in the range up to 10 GHz, which is typical for this object [3, 4]. The last property indicates indirectly that the magnetic structure can be represented by longitudinally magnetized domains [3, 4, 7—11]. This idea is

not universally recognized or it is interpreted in different ways. As follows from [2], the authors of this work accept this model. However, there is another point of view: (in the figure presented in [2], the magnetic structure is not defined concretely) the wire is a monodomain. There is a modification of this idea: the wire consists of microscopic monodomain segments with longitudinal magnetization directed oppositely. It disagrees with the experimental data obtained when the high frequency magnetic permeabilities of the ferromagnetic resonance and natural ferromagnetic resonance spectra [3, 4] are investigated. Several criticisms of this model, we examine obiter dictum.

It is known that, in a zero field, the cast amorphous glass-coated microwire is characterized by residual magnetization that is lower than the limit magnetization. The coercive force ($H_c \sim 1-5$ Oe) is lower by magnitudes than the field of the longitudinal magnetic anisotropy that causes the natural ferromagnetic resonance [3, 4]. Therefore, the cast amorphous glass-coated microwire in a quasi-static magnetic field can be switched due to the magnetic wall motion, i.e., inversely [21]. The simplest scheme of the magnetic reversal process is the domain wall motion along the thread radius of the cast amorphous glass-coated microwire. The domain structure can be represented schematically by two domains: internal and external domains in the form of an enveloping surface (Fig. 1a)
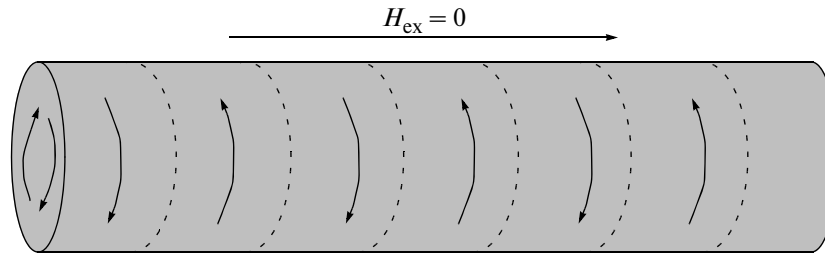
$H_{ex} = 0$

Fig. 2. The magnetic structure of bamboo type for Unitika wires with small negative magnetostriction [12]. A thin longitudinally magnetized domain should be in the center.
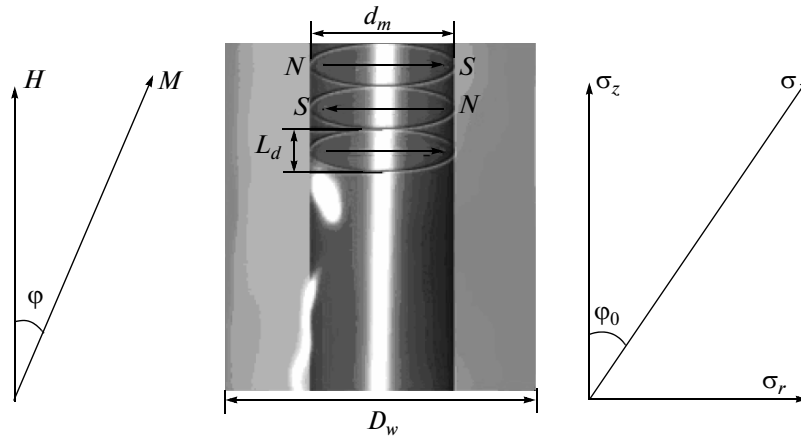

Fig. 3. The magnetic structure of the cast amorphous glass-coated microwire with small negative magnetostriction. Here, d_m is the thread's diameter, D_w is the diameter with the glass coating, and L_d is the domain's size (see [13]).

[7−11]. If we take into account that the examined segment of the cast amorphous glass-coated microwire is finite and that, at the segment's end, a defect in the glass coating of the closure domains is formed, the picture of the domain structure becomes more complicated. In the defect area of the glass coating, the external and internal domains can swap places towards the direction of magnetization. Such places are seen under magneto-optical and other investigations. The picture of the domain wall motion also becomes more complicated in a nonuniform field if the long wire segment is switched and the signal is detected by small remote coils.

For comparison, let us present the domain structure of the Unitika wire with positive magnetostriction according to the information presented in [5, 6] (Fig. 1b).

Both the cast amorphous glass-coated microwire and the Unitika wire as wires with negative magnetostriction are characterized by soft magnetic properties with sufficiently high magnetic permeability and practically by an hysteresisless loop. They are topical for developing sensors that use the huge magnetic impedance (HMI) phenomena [2, 12]. The domain structure of the wires produced by Unitika Ltd. is presented in the form of ring domains, which are magnetized as is shown in Fig. 2 (the so-called "bamboo" or BDS

structure, which is described in detail, for example, in [2, 12]).

The majority of scientists transpose the bamboo structure to the cast amorphous glass-coated microwire [2] and do it without correct grounding. For grounding, it is necessary to calculate the residual stresses in the thread of the cast amorphous glass-coated microwire, and it is done in [13], where the magnetic structure given in Fig. 3 is presented.

If we use this structure, it is possible to accept that the ferromagnetic resonance that causes the huge magnetic impedance appears in the subsystem of closure domains, which are magnetized in parallel to the wire's axis. For this purpose, in the magnetizing field, the thickness of the FRM active domains should be equal at least to the thickness of the skin layer (which should be calculated by considering the magnetic permeability variation caused by the resonance). It is possible to accept that the bamboo structure turns its domains due to the magnetic field action. It would seem that the qualitative description differs a little, but quantitatively the inversion can take place under fields that are significantly lower than the rotation of the domain magnetization. To take into account the nonlinear effect, the model that describes the domain structure is more important.

Let us point out that, for the wires with zero magnetostriction, there is the precise instanton solution [10, 14], it is different from the bamboo structure, and this result is independent of the technology of the wire's manufacturing. The rotating modes can appear if the constant anisotropy is taken into account [21] and if the anisotropy energy is independent of the reduced radius in contrast to [10, 14]. It is not sufficient for proving that the domains with a bamboo structure are formed [15]. There is the model of the bamboo structure formation due to the possible ellipticity of the wire, but we do not discuss this problem. To our mind, the bamboo structure can form in the wires with negative magnetostriction, since the residual tangential stresses are small in comparison with other stresses.

From all the mentioned above, it follows that it is necessary to ground the domain structures, and this is the aim of the present work. Since the domain structure is determined by the specificity of the magnetic anisotropy and the energy of the magnetostriction interaction is used as the anisotropy energy in an amorphous magnetic, to calculate the domain structure, it is necessary to properly solve the problem of how to calculate the residual stresses that appear during the microwire's manufacturing. It depends how correctly we solve the next problem for calculating the domain structure. There are several works [16–20] whose results are differed from the results obtained in previous works [3], and these disagreements are not explained. That is why we analyze once more the results obtained in previous works [3, 7–11]. Let us point out that, in [19], where the results of work [3] are used (without referencing [3]), improper conclusions are reached (from our point of view), and the authors of [19] continue pushing for their conclusions [20]. To calculate correctly the residual stresses, it is very important to take into account the experimental and theoretical results: all the residual stresses in the metallic thread of the cast amorphous glass-coated microwire are tensile. It follows from the fact that, if the glass coat is removed (etched), the thread becomes shorter [22].

Let us point out that the authors of [16] declare wrongly that the stresses in the wire are compressive. They are based on the indirect result that the thermal resistance of the cast amorphous glass-coated microwire structure increases.

INITIAL APPROXIMATION FOR CALCULATING THE RESIDUAL STRESSES IN THE CAST AMORPHOUS GLASS-COATED MICROWIRE

Any rapidly quenched microwire (Unitika or CAGCMW) synthesized directly from the liquid phase is in a stressed state [23]. Let us show how to calculate the residual stresses, which were examined in [3, 7–11], and let us accept this approach as a zero one that determines all the next refinements.

In cylindrical coordinates [3], the formulas for the radial $\sigma_{r(0)}$, tangential $\sigma_{r,\varphi(0)}$, and axial $\sigma_{z(0)}$ stress components can be written as follows:

$$\sigma_{r(0)} = \sigma_{\varphi(0)} = P = \sigma_m \frac{kx}{\left(\frac{k}{3} + 1\right)x + \frac{4}{3}},$$

$$\sigma_{z(0)} = P\frac{(k+1)x + 2}{kx + 1}, \qquad (1)$$

$$x = \left(\frac{Rc}{Rm}\right)^2 - 1,$$

where $\sigma_m = \varepsilon E_1$, $\varepsilon = (\alpha_1 - \alpha_2)(T^* - T) \approx 5 \times 10^{-3}$; α_1 is the coefficient of thermal expansion (CTE) for the metal ($i = 1$) and for the glass ($i = 2$); T^* is the temperature of the composite's solidification at the metal–glass contact ($T^* \sim 800–1000$ K); T is the temperature at which the experiment is performed; R_m is the metallic thread's radius ($d_m = 2R_m$); R_c is the external radius of the glass coating ($D_w = 2R_c$); $k = E_2/E_1 \sim (0.3–0.5)$; and E_i is Young's modulus (for the metal ($i = 1$) and for the glass ($i = 2$)).

To simplify the presented expressions, the Poisson ratio for the metal and glass are taken as 1/3. (Let us point out that the x parameter is similar to the r parameter in [2]).

According to Eq. (1), the longitudinal stress is the highest

$$\sigma_{z(0)} \sim (2–3)P; \qquad (1a)$$

i.e., $\sigma_{z(0)} > \sigma_{r,\varphi(0)}$, and P maximum is determined as follows:

$$P \to 0.5\sigma_m \sim 10^9 \text{ Pa.} \qquad (1b)$$

For the next step of the residual stresses' calculation, it is valid to use Eq. (1) as an initial approach (the first calculation in the framework of this model for the cast amorphous glass-coated microwire was presented in [3] and verified experimentally [3, 4, 8, 22]). Let us accept that the stresses calculated according to Eq. (1) take place on the thread surface of the cast amorphous glass-coated microwire.

The presented formulas consider not the total class of residual stresses. Let us present the established classification for the residual stresses according to [23–32].

(1) Stresses of the first kind.

These stresses are macroscopic ones: they are typical for the material volume, where the macroscopic equations with macroscopic coefficients are used. For example, the stresses appearing due to the difference in the thermal expansion coefficients for the metal and silicate glass (1) and maybe for the intermediate layer [33]. They have symmetry orientation, for example, connected with a cylindrical shape. To calculate these

stresses, the methods used in the theory of elasticity are sufficient.

(2) Stresses of the second kind.

These stresses are microscopic and they are spread for separate metal grains or for group of grains. These stresses should be studied in the framework of the dislocation theory, for example, [25]).

(3) Stresses of the third kind.

These stresses are submicroscopic, and they relate to the crystal lattice's distortion. To calculate these stresses, it is necessary to investigate the atomic models of the structure.

In the first approximation, the residual stresses of the first kind for the cast the amorphous glass-coated microwire are described by Eq (1). Just the stresses of the first kind form the magnetic structure. That is why as the least approximation we accept just the stresses caused by the difference in the thermal expansion coefficients for the glass and metal. These stresses appear in the glass—metal seal during the amorphous glass-coated microwire's casting, and they increase with the composite's cooling. As we know, nobody takes into account the residual stresses of the second and third kinds for micro- and nanowires, but it is possible to accept that they appear in very small chaotically placed microareas (of about nanometers), and there is a trend for averaging (in the micron range). However, to calculate the domain structure of the cast amorphous glass-coated microwire, the relaxation processes in the microwire thread should be taken into account, since they cause the relationships between σ_r, σ_φ, and r. r is the cylinder's coordinate (which is varied from the center towards the thread's surface). Let us examine the simplest variant for the stresses' calculation by using the theory of elasticity and by considering the plastic relaxations [26—32]. Let us point out that the same problem was solved by G. Lamè in 1852.

THE LAMÈ PROBLEM WITH RESPECT TO THE CAST AMORPHOUS GLASS-COATED AND UNITIKA MICROWIRES

Let us present the microwire thread in the form of coaxial cylindrical surfaces with radiuses of R_i ($i = 1$, 2, 3...). Since the problem is symmetric, the field of the displacements for the metal thread is introduced as a function of U_r and U_z (over the axes r and z).

Let us examine an infinitely long cylinder, for which it is sufficient to introduce the radial deformation $U_r \equiv u$, which meets the following equation (for more detailed see in [26, 27]):

$$u'' + \frac{1}{r}u' + \frac{1}{r^2}u = cf(r). \qquad (2)$$

This equation makes it possible to examine in more detailed the deformation problem of an infinite cylindrical figure with the internal radius r_1 and the external

radius r_2. Let the pressures P_1 and P_2 and the volumetric forces directed along the radius with density of $f(r)$ (where $c \sim \nu/E$) act on the cylindrical surfaces of the figure.

If there are no volumetric forces, the solution for the residual stresses can be presented as follows [26—32]:

$$\sigma_r = P_1' - \frac{c_1}{r^2}, \quad \sigma_\varphi = P_1' + \frac{c_1}{r^2}, \qquad (3)$$

where P_1' and c_1 are determined from the boundary conditions for the stresses (and the surface geometry). For our case,

$$P_1' = \frac{P_2 r_2^2 - P_1 r_1^2}{r_2^2 - r_1^2}, \quad c_1 = \frac{P_2 - P_1}{r_2^2 - r_1^2} r_2^2 r_1^2. \qquad (4)$$

It is assumed that the stresses (i.e., the pressures superposed on the cylindrical surface) are tensile (for the cast amorphous glass-coated microwire), which is important for selecting the sign. In the presented formulas, the values of P_1' and c_1 are positive if

$$P_2 \geq P_1. \qquad (5)$$

Just such a situation takes place in the cast amorphous microwire. From here, there follows the important relationship

$$\sigma_r \leq \sigma_\varphi. \qquad (6)$$

If we present the microwire thread in the form of coaxial cylindrical surfaces with radiuses R_i ($i = 1, 2, 3, ...$), respectively, and if we specify the external boundary conditions, it is possible to generate the recurrent relationships, which make it possible to calculate numerically the residual stresses (the procedure for such calculations is presented, for example, in [30, 33]). As the boundary conditions, we accept the maximal stresses on the thread's surface, which can be estimated by using Eq. (1). From the numerical calculations for the cast amorphous glass-coated microwire, it follows that the residual stresses in the next layers decrease (in magnitude) and remain tensile. The calculations carried out according to this procedure, if even several layers are taken into account, are differed from the results presented in [15—20] (the details of which we examined in the other paper).

The analytical relationships between the residual stresses and the coordinates of the cylinder's radius are important for the problem concerning the domain's structure. It is possible to show that, in the limit of an infinite number of layers, the residual stresses σ should meet the nonlinear differential relationship

$$\frac{\partial\sigma(s)}{\sigma(s)} = \left(1 - \frac{s^2}{\partial s}\right)^{-1}, \qquad (7)$$

where $s = \pi r^2$ is the cross section area in the given cylinder's segment. Equation (7) has the approximate solution

$$\sigma_s \approx \sigma_0 \exp\left\{-\frac{c_1'}{r^2}\right\}. \qquad (8)$$

Let us expand Eq. (8) into a series and compare Eqs. (8), (3), and (1); as a result, we have as follows:

$$\sigma_{r(1)} \approx P\left[1 - \left(\frac{b}{r}\right)^2\right], \quad \sigma_{\varphi(1)} \approx P\left[1 + \left(\frac{b}{r}\right)^2\right], \qquad (9)$$

where b is the minimal limit value of the radius r_1. In contrast to Eq. (1), the residual stresses (9) take into account the relaxation processes. If we accept that the area with boundaries from $r_1 \equiv b$ up to the external radius $r_2 \equiv R_{th}$ is the area of elastic stresses, from Eq. (9) it is easy to generate the equilibrium equation [26−29]

$$r\left(\frac{d\sigma_r}{dr}\right) = \sigma_\varphi - \sigma_r. \qquad (10)$$

In addition, the relation that follows from Hooke's law is true: the sum of the radial and tangential stresses under the given radius of the cylindrical surface is constant:

$$\sigma_r + \sigma_\varphi = 2P. \qquad (11)$$

Let us estimate the axial stress σ_z of the known components $\sigma_{r\varphi}$ (1):

$$\sigma_{z(1)} \approx \nu 2P. \qquad (12)$$

The estimation carried out according to Eq. (12) is undervalued in comparison with Eq. (1a) if we accept that the Poisson's coefficient is 1/3. The zero problem's inaccuracy with respect to the obtained solution is manifested in the invalid equality between $\sigma_{r(1)}$ and $\sigma_{\varphi(1)}$ on the thread's surface, which is valid for the zero problem

$$\sigma_{r(0)} = \sigma_{\varphi(0)} = P.$$

To bind Eq. (9) more accurately, it is possible to use the fact that the constant stresses $\sigma_{r,\varphi,z(1)}^0$ (independent of the coordinate r) are added to the general solution. In this case, it is possible to rewrite Eq. (9) as follows:

$$\sigma_{r(1)} \approx P\left(1 - \frac{b^2}{r^2}\right) + \sigma_{r(1)}^\circ,$$

$$\sigma_{\varphi(1)} \approx P\left(1 + \frac{b^2}{r^2}\right) + \sigma_{\varphi(1)}^\circ,$$

$$\sigma_{z(1)} \approx \nu(\sigma_{r(1)} + \sigma_{\varphi(1)}) + \sigma_{z(1)}^\circ \sim \nu(P + \sigma_{z(1)}^\circ).$$

From Eqs. (10)−(12), it follows that

$$\sigma_{r(1)}^0 = \sigma_{\varphi(1)}^0 \sim P/2 \to 0.5(\sigma_{z(1)}^0).$$

And, if $\nu \to 0.5$ (and $b \le R_m/2$), the residual decreases. It is possible to decrease the residual totally only by numerical calculations, that is why below only the functional relationship between $\sigma_{r(1)}$ and the thread's radius is of interest.

If we take into account that, in an Unitika wire, in contrast to the cast amorphous glass-coated microwire, the summary stresses should decrease on the thread's surface and increase towards its center, inequality (6) is changed to the opposite one. Since under negative magnetostriction the magnetization is orientated according to the minimal stress (in our case according to σ_φ), in an Unitika wire the bamboo structure is possible. The bamboo magnetic structure in the cast amorphous glass-coated microwire can appear during the glass coating's etching. Maybe it exists in the cast amorphous glass-coated microwire with a thin glass coating or after the thermal or thermomechanical treatment. For Unitika wires with positive magnetostriction, it is reasonable to assume that the main domains' magnetization is directed along the radius, which verifies indirectly the scheme for the domain structure of the magnetic wire with positive magnetostriction according to [5, 6] (Fig. 1b). Maybe for the thin microwire, it will be simpler. The analytical relationship for the residual stresses in an Unitika wire in the area close to the surface can be asymptotic:

$$\sigma_{r(u)} \sim P_u + b_u\left(\frac{1}{r}\right)^2,$$

$$\sigma_{\varphi(u)} \sim P_u - b_u\left(\frac{1}{r}\right)^2,$$

$$\sigma_{z(u)} \sim \nu 2P_u,$$

where P_u and b_u are determined from the boundary conditions [26−32]. For a more complicated variant, the problem for calculating the residual stresses for the free cylinder by considering the thermal relaxation is examined in [28, 32].

THE WAY TO CONSIDER THE PLASTIC RELAXATION IN THE CAST AMORPHOUS GLASS-COATED MICROWIRE AND TO CALCULATE THE STRESSES IN THE RELAXATION AREA

According to the present model, we accept that, inside the microwire, there is an area beginning from the radius b and less where plastic relaxations are important. It is not my aim to describe in detail how to find the solution; I present a short way for solving the problem.

According to the known procedure for the calculation, let us introduce the Airy function Φ [26−28, 31, 32], for which it is possible to write the following:

$$\Phi_t'''' - 4\Phi_t''' + 4\Phi_t'' = 0, \qquad (13)$$

where the differentiation is performed with respect to $t = \ln r$. In this case, the general solution (with arbitrary constants P_1', c_1, k) for the residual stresses can be presented as follows [26−28, 31, 32]:

$$\sigma_r = P_1' - \frac{c_1}{r^2} + 2k\ln r,$$

$$\sigma_\varphi = P_1' + \frac{c_1}{r^2} + 2k(1 + \ln r). \tag{14}$$

The two first members of the generated functions are used in the previous part of the paper. The stresses that appear in the third area when $r < b$ we accept as "plastic," since, under rapid quenching of the amorphous material, plastic relaxation is possible. Until the stresses are elastic and they are independent of the angle φ in cylindrical coordinates, it is possible to show that Eq. (9) totally describes the set problem till the radius b in the whole elastic area ([32, pp.112−113]). According to the theory of plastic stresses, the solution region can be extended up to the radius b, where the criterion of the continuum model's applicability is invalid. Let us present the additions to the stresses in the "plastic" area (for $r < b$) as follows:

$$\sigma_{r(2)} = 2K \times \ln\left(\frac{r}{b}\right),$$

$$\sigma_{\varphi(2)} = 2K \times \left[1 + \ln\left(\frac{r}{b}\right)\right], \tag{15}$$

$$\sigma_{z(2)} \approx \nu \times (\sigma_{p(1)} + \sigma_{\varphi(2)}) \sim 2K \times \left[1 + 2\ln\left(\frac{r}{b}\right)\right],$$

which agrees with the results of the more precise theory [28] (here, the Poisson coefficient ν is equal to 1/2 [28, 32]). This analytical solution for Eq. (15), which is sufficient for calculating the magnetic structure, is known in the theory of plastic relaxation as a solution where the Tresca yield condition is considered (for more details about the Tresca yield condition, see [28], [32]). Let us point out that it is possible to add the stresses $\sigma_{i(k)}$, which depend weakly on the radius, to Eqs. (1), (9), and (15) (for more detail, see in [28]). In our case, for calculating the domain structure, their contribution is insufficient.

To estimate the K and b parameters, we used the experimental data [8] and, based on the experiment and the physical ideas of [8−11, 34], we accept that the upper boundary is $b \le Rm/2$ and the bottom boundary is $K \sim 0.1P$.

Hereby, there is presented the model in which the residual stresses $\sigma_{r, z}$ in the cast amorphous glass-coated microwire thread (in contrast to [16−20]) decrease towards the thread's center. The stresses' relaxation is the reason for this phenomenon. The plastic relaxations of the elastic stresses can be explained as follows: during the thread cooling, the temperature drop between its center and periphery is hundreds of degrees (Celsius) [23]. The microwire's surface connects with the glass by a chemical bond, which is higher than the residual stresses' energy. Up to the internal radius b, only the elastic relaxation takes place. The stresses that appear in the microwire's area close to the thread's center ($r < b$) we accept as "plastic," since, during the amorphous materials' quick quenching, the plastic relaxation can occur. For clearness, let us present the schemes for the stresses that take place in the amorphous thread and silicate glass, which only illustrate our further reasoning. For the examined domain model, the radial residual stresses are of interest, but the numerical calculations show that their qualitative forms are similar to the form of the axial stresses that is seen in Fig. 4.

We also accept that all the residual stresses in the microwire thread are tensile (i.e., positive) since there is no mechanism that can change them. The negative addition $\sigma_{r(2)}$, which refers to the relaxation, is lower than the positive (tensile) stress, which has already existed and been calculated according to Eq. (1). For $r \ll b$, where this addition becomes higher, the range of applicability of our model is invalid and we "cut" this area from our examination. In the glass coat, the residual (axial and radial) stresses are compressive. According to the equilibrium condition on thread−glass surface, if the thread is stretched out, the glass is compressed. We also assume that, when the coating is taken away, the radial stresses inside the thread can become compressive (in the thread's internal area) [28] (Fig. 4b, item β).

In contrast to our model, in the model presented in [18−20], the residual stresses decease towards the cast amorphous glass-coated microwire's surface and the axial stress σ_z is the least stress on the thread's surface, which disagrees with Eqs. (1), (1a), and (1b) and with the experiments on natural ferromagnetic resonance. That is why, from our point of view, the works where these results are used are not correct due to this reason.

THE WAY TO CALCULATE THE DOMAIN WALL IN THE CAST AMORPHOUS GLASS-COATED MICROWIRE WITH POSITIVE MAGNETOSTRICTION

Let us examine the simplest magnetic model of the microwire consisting of two domains magnetized along a cylinder's axis in different directions and separated by a 180° Bloch domain wall (DW) of cylindrical form (Fig. 1a). In terms of energy, the domain wall should originate in the area of $r < b$, where the anisotropy energy is lower (Fig. 4a, b). Let us estimate the domain wall size Δ_1 according to two competitive energies:
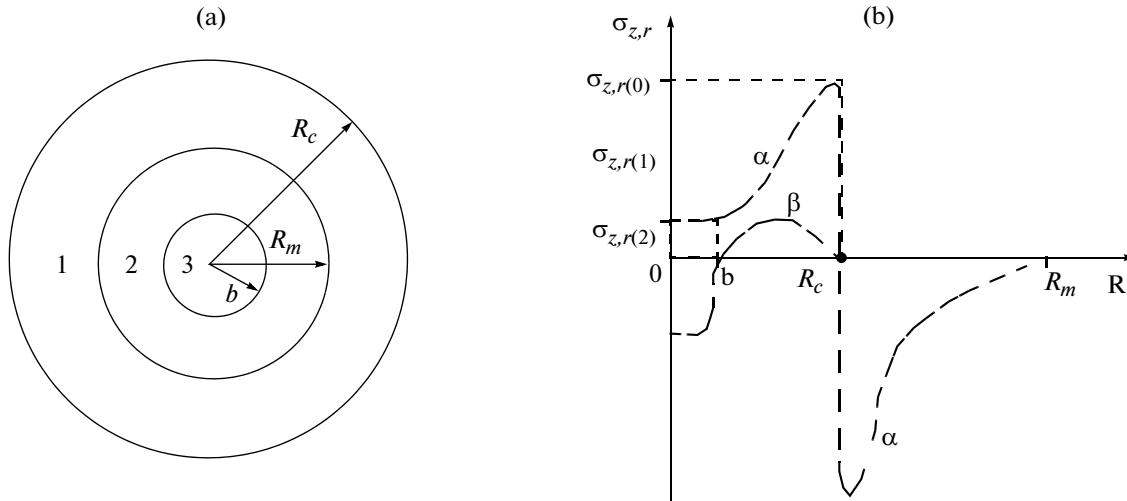
Fig. 4. (a) Microwire transversal cross section: R_m is the metallic thread's radius, R_c is the external radius of the glass coating, and b is the radius of the plastic deformation boundary. The maximal stresses (1) in the thread take place at the thread−glass boundary (boundary *1−2* in the R_m area). The area inside *3* where the criterion of the model's applicability is invalid is not shown (which is lower by orders than the radius b). (b) A qualitative view of the residual stresses distribution ($\sigma_{r,\ z}$ along the mircowire's radius; α is in the initial state (in the thread and in the glass); β when the glass coating is totally removed (only for radial stresses).

the energy of the exchange interaction

$$W_0 \sim \frac{A}{\Delta_1}$$

and the anisotropy energy, which is estimated as follows in the third area:

$$W_a \sim \lambda K b \times \ln\left(\frac{\Delta_1}{b}\right) + \frac{2}{3}\lambda\sigma_z^\circ b.$$

The standard procedure for minimizing the sum of these energies

$$\frac{\partial}{\partial(\Delta_1/b)}\left(\frac{A}{\Delta_1} + \lambda K b \times \ln\left(\frac{\Delta_1}{b}\right) + \frac{2}{3}\lambda\sigma_r^\circ b\right) = 0 \quad (16)$$

results in the following formula:

$$-\frac{A}{\Delta_1^2} + \lambda K b\left(\frac{1}{\Delta_1}\right) = 0. \quad (17)$$

From here, for the thickness of the incipient domain wall, we obtain the estimating value

$$\Delta_1 \approx \frac{A}{\lambda K b}. \quad (18)$$

To estimate the domain wall's size, let us use the following parameters: $A \sim 10^{-11}$ J/m; $b \sim 10^{-6}$ m; $\lambda \sim 10^{-6}$; and $K \sim 10^8$ Pa. As a result, we have

$$\Delta_1 \sim 10^{-7} \text{ m}, \quad (19)$$

which is lower by an order than the microwire's diameter. According to this result, it is possible to say that, in a wire with positive magnetostriction and with a diameter lower than 10^{-6} m, the domainless magnetic

structures can be [10, 14, 21]. The cast amorphous glass-coated microwire can be monodomain with sufficiently high positive magnetostriction beginning from sizes of $10^{-7}-10^{-8}$ m if the estimations are performed according to [21]. Therefore, there are no contradictions in logic if we assume that the presented magnetic structure is possible for the cast amorphous glass-coated microwire with a thread diameter higher than 10^{-6} m and sufficiently high positive magnetostriction. A wire with zero magnetostriction can be domainless even if the radiuses are higher than 10^{-6} m [10, 14].

For the energy density of the domain's wall, we obtain the following estimation:

$$W_1(\Delta_1) \sim \Delta_1\lambda\sigma \sim \frac{A}{\sigma} \sim 10^{-5} \text{ J/m}^2. \quad (20)$$

Let us compare the results obtained according to Eqs. (18)−(20) with the classical domain wall thickness δ obtained according to the Landau−Lifshits−Doering theory [35, 36]. The simplest variant of the procedure for minimizing the sum of two competitive energies—the energy of the exchange interaction $W_0 \sim A/\delta$ and the anisotropy energy $W_a^{II} \sim \lambda\sigma_z^\circ\delta$— results in the equation

$$-\frac{A}{\delta^2} + \lambda\sigma_z^\circ = 0 \quad (21)$$

and in the known formula for the classical domain wall (Bloch−Landau−Lifshits−Doring [35, 36])

$$\delta_{LL} \sim \sqrt{\frac{A}{C}}, \quad (22)$$

where the value of $C \sim \lambda \sigma_z^\circ$ is comparable with the anisotropy energy of the cast amorphous glass-coated microwire with positive magnetostriction. If we estimate δ_{LL}, we obtain sizes whose value is higher by an order than Δ_1 (i.e., δ_{LL} can become higher than the cast amorphous glass-coated microwire's diameter). However, if we like the presented domain scheme to exist, the domain wall should be significantly lower than the microwire's diameter to form at least a two-domain structure. To save the situation, it is possible to accept the model of a microwire consisting of monodomain segments (according to theory [36] their size should be approximately of $(L)^{1/2}$, where L is the sample's length), which are separated by transversal domain structures. However, in this case, the problem of the enormously high rate of the domain wall's motion, which can be higher than the sound velocity in the metal, appears. The experiments on the magnetic permeability of the natural ferromagnetic resonance are incomprehensible, since even two oppositely magnetized macroscopic areas should be seen in the spectrum of the natural ferromagnetic resonance.

It is possible to write the energy density of the infinite flat Bloch domain wall that separates the domain's infinite half-space as follows:

$$W_{LL} \sim (AC)^{1/2}. \tag{23}$$

It is known [35] that the functional relationship between H_c and the magnetic and technological parameters is the same as for the energy density of the domain wall. If Eq. (23) is used, we obtain the popular relationship

$$H_{c(LL)} \sim (\sigma)^{1/2}. \tag{24}$$

Where, under σ, we mean both the residual and external stresses superposed onto the microwire, and it explains, for example, why the coercive force increases under tension. It is absolutely clear that in Eq. (24) the geometrical, magnetic, and technological features of the cast amorphous glass-coated microwire are not taken into account, and it can be used only qualitatively for confirming the experiments. It is observed for any stretched wire.

According to our model, the cast amorphous glass-coated microwire consists of three segments, and magnetic reversal nucleation takes place in the microwire's center if we do not consider the microwire's ends and the defects in the glass coating. Therefore, if the domain wall moves along the thread's radius, it should be transformed. In the experiment, it should result in several values of the domain nucleation field during the switch, and it is seen in the experiment (see below). From Eq. 20, it follows that the first domain nucleation field H_{c1} (after the domain wall nucleation) is independent of the magnetostriction and residual stresses, and it is determined only by the specific exchange energy A/b, which is typical for the domain wall nuclei. It is possible to accept that H_{c1}

is the field corresponding to the new magnetic phase nucleation during the microwire's magnetic reversal. It is difficult to see H_{c1} experimentally, since the volume of the magnetic reversal material is very small and the magnetic noise is high, but it is possible (especially under low temperatures).

In the second area (Fig. 4), which is described by Eqs. (9)−(12), it is impossible to have a stable domain wall, and this area should be switched by a jump. It is due to the fact that the relationship between the anisotropy and the coordinate r is steeper than for the exchange interaction.

In the third area of the cast amorphous glass-coated microwire thread (in Fig. 4, it is not shown), which is the near-surface area of the metal−glass interface, where Eq. (1) is true, the residual stresses can be accepted as constant, and here the domain wall is a cylindrical surface. For it a calculation similar to the calculation presented in [15] is sufficient (in [15] another model is examined, but the analytical relationship obtained in [15] is suitable for our model). However, to obtain the final formulas, let us take into account Eq. (1), and, as a result, we have

$$\Delta_3 = \left(\frac{A R_m}{\lambda P}\right)^{1/3} \sim 10^{-6} \text{ m}, \tag{25}$$

$$W_3(\Delta_3) = \left(\frac{A^2 \lambda P}{R_m}\right)^{1/3} \sim 10^{-4} \text{ J/m}^2. \tag{26}$$

The respective domain nucleation field H_{c3} should be higher than H_{c1} (since W_3 is higher than W_1). Let us estimate the relationship between H_{c3} and the microwire's thread radius R_m by considering Eq. (1):

$$
\begin{aligned}
H_{c3} &\sim \sqrt{\frac{kx}{\sqrt[3]{R_m\left[\left(\frac{k}{3}+1\right)x+\frac{4}{3}\right]}}}, \\
&\quad k \sim 0.3-0.5, \\
&\quad x = \left(\frac{R_c}{R_m}\right)^2 - 1.
\end{aligned}
\tag{27}
$$

From the experiment, it is known that the coercive force's value decreases if the thread's radius R_m increases (if the glass coating's thickness is fixed), which corresponds to the obtained formula.

The dependence on the magnetostriction $\lambda^{1/3}$ (and the similar dependence on the residual stresses) corresponds to the experimental data with the same error as the dependence obtained by several scientists under fitting Eq. (24) (i.e., $\lambda^{1/2} \sigma^{1/2}$). However, Eq. (26) is more suitable for the cast amorphous glass-coated microwire's geometry than Eq. (24) (which follows from Eq. (23)).
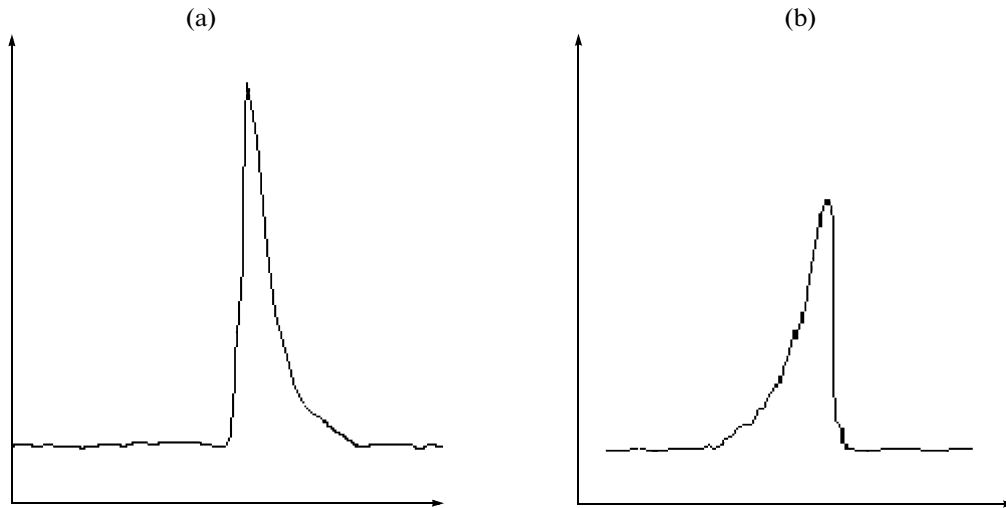
Fig. 5. Electromotive force pulses caused by the large Barkhausen jump in the cast amorphous glass-coated microwire: (a) relaxation, (b) acceleration.

EXPERIMENTAL RESULTS AND DISCUSSION

The experimental investigation of the magnetic reversal process in the cast amorphous glass-coated microwire shows that there are two mechanisms of magnetic reversal: relaxation and acceleration [7, 37]. The electromotive force pulses at the measuring coils caused by the large Barkhausen jump that correspond to these mechanisms are different in shape, amplitude, and duration. The relaxation mechanism is characterized by a pulse with a steep rise and a smooth droop; the acceleration mechanism is characterized by a smooth rise and a steep drop over the second pulse's edge (see Fig. 5 and also [7, 37]).

The experimentally detected parameters are examined: the domain nucleation field Hs (let us designate the theoretical domain nucleation field as Hc and the experimental one as Hs), the amplitude of the Um pulse induced in the measuring coil, and the domain's nucleation field fluctuations Σ_{Hs}. We investigate how the magnetic reversal conditions influence the glass coating state of the cast amorphous glass-coated microwire. As the main and practically single important result, we reveal the follows: if the glass coating is removed from of the cast amorphous glass-coated microwire's end by etching with hydrofluoric acid, the domain's nucleation field and its fluctuations decrease by 2–3 times.

The experimental result demonstrating that there are two mechanisms of the magnetic reversal agrees with the presented theory on the domain wall's nucleation and motion in the cast amorphous glass-coated microwire in the following way (the presented theory is based on the residual stresses' calculation). Let us describe qualitatively how the domain wall moves from the thread's center towards the microwire's surface. In the third area (Fig. 4a), where the residual stresses are small, the magnetic reversal occurs first of all due to the domain wall's nucleation and, second, due to its motion (i.e., according to the acceleration mechanism), and the domain wall is retarded continuously by small defects. These defects always exist in the amorphous matrix and they are formed during the microwire's manufacturing. It is most probable that they are the reason for the Barkhausen jumps' fluctuations during the magnetic reversal according to the acceleration mechanism. To describe this segment of the domain wall's motion, it is possible to use Doring's equations [35, 36]. Let us point out that the acceleration form of motion can be at the end of the second area near the boundary with the glass coating with the domain nucleation field of H_{c3}.

As was mentioned before, in the second area (Fig. 4a) (more precise, at it very beginning), the magnetic reversal should occur according to the mechanism of the domain wall's motion. In this area, the domain wall exists virtually. For this segment, it is possible to write Brown's equation [10, 11, 21] with the external magnetic force. If we accept that the radius of this area during the magnetic reversal changes weakly (i.e., we replace the cylindrical surface by a flat one) and if we assume that the magnetic reversal rate is finite, it is possible to generate a differential equation (of the second order) similar to Doring's equation. It is important that the values of the relaxation and elastic constants in this equation are different from the previous Doring equation that describes the acceleration mechanism of the motion. As follows from the experiment and from our reasoning, the magnetic reversal in this area occurs by a jump (i.e., practically in the same way as for small domainless particles) with further relaxation fluctuations. The relaxation fluctuations are caused by the fact that the relaxation after the magnetic reversal is rather slower than it is under
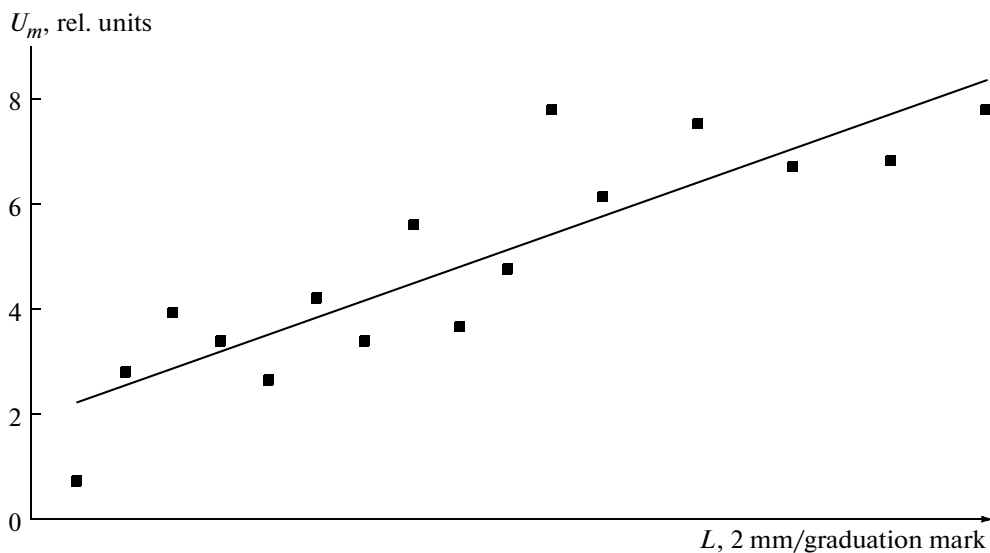
Fig. 6. The relationship between the pulse amplitude U_m at measuring the coil and the sample length L [37, 38].

the real motion of the domain wall. The transition model is similar to the motion of a quasi-classical particle during transiting between two quasi-degenerate adiabatic states. The reason for the quasi-degeneracy of these states is the heat energy, which, at a temperature higher than 100 K, is higher than the anisotropy energy's barrier (the model of over-barrier motion). If the condition of the energy terms' degeneration is invalid, the domain's nucleation field increases exponentially, which can be under the temperature decreasing [7–11]. In this case, the magnetic reversal rate decreases exponentially. In the case of energy quasi-degeneracy, the problem can be described by the quasi-classical way (similar to Landau–Zener–Stuckelberg). The probability is that the process is proportional to the energy of the interaction in the transition area. In our case, it is proportional to $\sigma_{r(0)} = \sigma_{\varphi(0)} = P$ and inversely proportional to the difference in the forces at the point of the terms intersection; in our case, it is similar to the domain nucleation field H_c. It is possible to accept that the transition probability is the highest if the following relation is true:

$$H_c \sim P,$$

which agrees qualitatively with the experiment. If the microwire is stretched, the P parameter increases and, therefore, H_c rises. It is possible to verify the theory, for example, by creating the magnetization nucleus. It can suppress the acceleration phase of the motion of the domain wall. Experimentally, it can be done, for example, by etching the glass insulation from microwire's ends.

We start to discuss the experimental data by verifying how the length of the cast amorphous glass-coated microwire sample influences Hs, Um, and the domain's nucleation field fluctuation Σ_{Hs}. Only the

amorphous glass-coated microwire samples with positive magnetostriction on the basis of ferrum with additions of cobalt, nickel, and metalloids (boron, silicon, and carbon) have been studied [7, 37]. The sample's length is varied from 20 up to 1 mm by cutting the microwire (the diameter of the metallic thread for different samples is varied in the framework of 2–25 μm, and the glass coating's thickness is varied from 1 up to 15 μm). The samples with the following characteristic feature—their hysteresis loop is rectangular even if their length is about 1 mm (the sample is bistable, if its length is less than 1 mm [38]) are chosen for the investigation. For the samples cutting, we choose the segments without cracks, bendings, or fractures, which are detected visually and by means of a microscope, and those samples are rejected. Figure 6 depicts the relationship between the signal's amplitude Um of the reading coil and the sample's length. The relationships between the other parameters (in particular, for the domain's nucleation field Hs) and the sample's length are not observed in the framework of the experimental error: 10% [37, 38]. We obtain a linear relationship between the signal's amplitude Um and the sample's length in the framework of the measurement error (Fig. 6). If the sample consisted of macroscopic domains magnetized in opposite directions (longitudinally) and separated by sufficiently thick domain walls, the root nonlinearity of the presented relationship could be, since the number of domain walls can be estimated as $\sim(L)^{1/2}$, and the signal is proportional to them.

Since in several samples four and more Barkhausen jumps can be within one cycle of magnetic reversal (possibly due to defects' presence [37] and we do not discuss it), the samples are prepared for examination very carefully in two ways: mechanically and chemi-
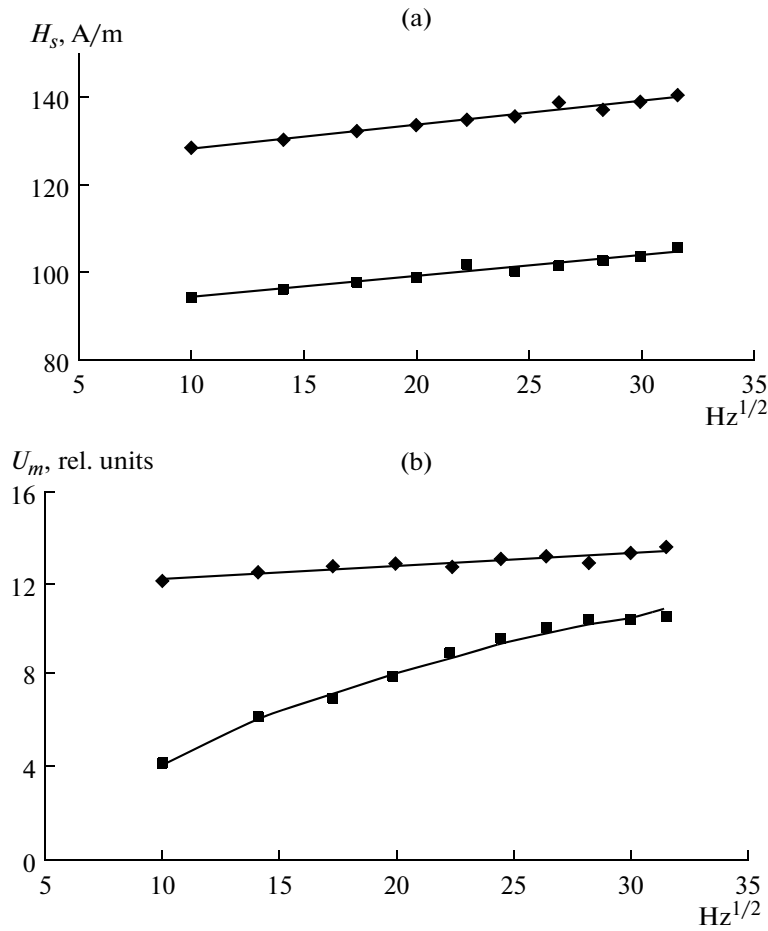
Fig. 7. The relationship between the electromotive force pulse and the switching field frequency; (a) $H_s = F(\sqrt{f})$; (b) $Um = F(\sqrt{f})$. In the plot, H_s and Um for the pulse relaxation mechanism are shown by small rhombs, and H_s and Um for the pulse acceleration mechanism are shown by small rectangles.

cally−mechanically and inspected carefully by means of a microscope. The mechanical method makes it possible to cut the samples to 1 mm in length. The chemical−mechanical procedure for the samples' preparation is the chemical processing (after cutting) of the elements or elements segments. The samples are placed into an HF-based solution until all or some part of the glass coating is removed. To etch the glass from a certain length of the sample, it is treated by special solutions to exclude the capillary effect. If necessary, the etching process can be stopped by removing the acid remains by water.

After that, we discuss the results of the investigations for the cast amorphous glass-coated microwire whose ends were not treated chemically [37]. Both forms of motion of the domain wall are investigated (the experimental error is not higher than 10%), and we reveal that the domain's nucleation field Hsr of the relaxation pulse (in the plot it is shown by small rhombs) is higher than the domain nucleation field Hsa of the acceleration pulse (in the plot, it is shown

by small rectangles) (Figs. 7, 8). The frequency is varied from 100 up to 1000 Hz, and the field's amplitude is varied from 200 up to 700 A/m.

It is shown (Fig. 7) that the domain nucleation field Hs of the relaxation and acceleration pulses depends weakly on the frequency f of the external pulse of the switching field (in the examined frequency range). The amplitude Umr and the domain nucleation field Hsr of the relaxation pulse depend weakly both on the frequency f and the amplitude H_M of the external pulse of the switching field (Figs. 7, 8). Similar parameters of the acceleration pulse are more sensitive to external field variation: both the amplitude Uma and the domain nucleation field Hsa of the acceleration pulse increase by 2 times and more (Fig. 7, 8). As for practical application, the relaxation mechanism's stability is a useful property. The relationships between the Uma of the acceleration mechanism of the domain wall's motion and the frequency and between Has and the switching field H_M's amplitude (Fig. 7, 8) can be con-
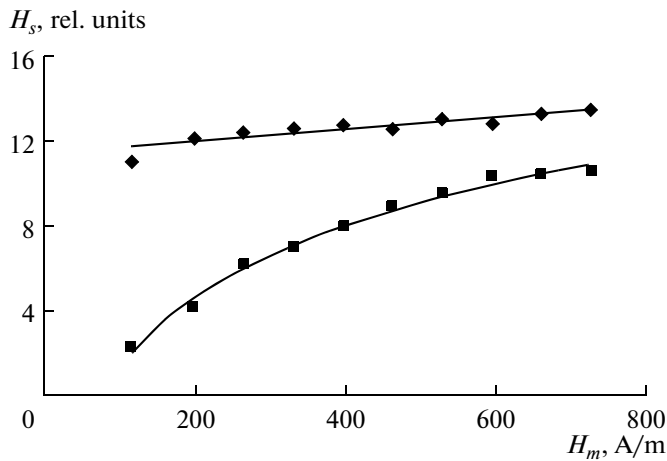
H_s, rel. units

Fig. 8. The relationship between the domain nucleation field H_s and the switching field amplitude (all the designations are similar to the designations presented in Fig. 7).

nected with the domain wall's retardation by microdefects.

One of the important results obtained in the presented work is as follows: we reveal how the state of the glass coat at the wire's ends influences the magnetic reversal process. Figure 9 depicts the microwire samples with different states of the glass coating. As a rule, the glass coating at the microwire's end is damaged during mechanical impact; therefore, by using chemical–mechanical means, the following ends are formed:

—an even fracture;

—the thread's end sticks out;

—the thread's end is immersed (the microwire's end is chemically etched in a mixture of hydrochloric and nitric acids) (fig. 9).

As an example, let us present one typical result of the investigation.

The second variant of the microwire's end with the thread sticking out is of the most interest, since the domain's nucleation field and its fluctuations decrease, and it is very important for practice.

We also etch step by step the glass coating from one end of a 10 mm sample (the etching length is less than 2 mm). The final thickness of the etched glass is measured by a microscope. If the glass's thickness at the sample's end has decreased, the domain's nucleation

field and its fluctuations decrease approximately by two times.

If the total glass coating is etched off of the sample, we observe as follows: Hs decreases, for example, from 136.6 down to 87.9 A/m, but the fluctuations of the domain's nucleation field increase by two times.

CONCLUSIONS

Since the requirements for the parameters and the operating performance for modern instruments are increased and also due to the instruments' miniaturization, there is a necessity for new sensors and active magnetic field elements. The progress in this field is connected with new materials. The most topical are the bistable amorphous dipoles made of cast amorphous glass-coated microwires switched by a large Barkhausen jump. However, they are of interested not only in terms of practice. The investigation of the properties and bistability formation in amorphous ferromagnetics are important for the theory of ferromagnetism [1, 37–39].

It is shown that, during magnetic reversal, complicated processes caused by the residual stresses' distribution, which influences the important performance (in terms of practice) such as the domain's nucleation field and its amplitude and fluctuation, take place in the cast amorphous glass-coated microwires. A way for controlling the domain's nucleation field fluctuations in bistable cast amorphous glass-coated microwires by means of the glass coating's etching out of the dipole segments' ends is developed. This method for improving the large Barkgausen jump connects with the nucleation process and its idea is as follows: the areas able to switch by relaxation are formed. Two types of electromotive force pulses—relaxation and acceleration—which indicate that there are two mechanisms for switching the large Barkgausen jump, are investigated by means of the induction method. A theoretical model that explains this fact is presented. Under the transition from the acceleration mechanism of the domain wall's motion to the relaxation mechanism, the fluctuations of the domain's nucleation field decrease by two times.

Unfortunately, in the framework of the presented work, it is impossible to analyze all the models. Let us refer only to the last ones [40, 41]. Let us point out that, when determining the real rate of the domain wall's motion V in the wire, the author use a model
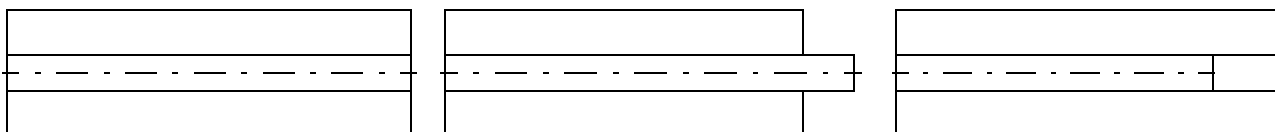

Fig. 9. End types of the cast amorphous glass-coated microwire.

The domain nucleation field and its fluctuation by the example of three types of samples 10 mm in length with different types of microwire ends

Number	End type	Domain nucleation field Hs, A/m	Fluctuation of the domain nucleation field	
			A/m	*%Hs*
1	Even fracture	146.88	2.64	1.8
2	Thread end sticks out	82.52	1.23	1.49
3	Thread end is immersed	150.02	4.68	3.11

similar to the model presented in [42], where it is determined as follows:

$$V \sim \nu(D_w/L_e),$$

where ν is the magnetic reversal rate of the sample [43], and L_e is *the longitudinal length* of the domain wall. For estimations, it is possible to use the sample's length L instead of L_e. Since the D_w/L value is sufficiently small, the rate of the domain wall's motion does not exceed the sound velocity in the sample. Let us point out that the magnetic models presented in [43] and [35] are close to the model described in the present paper. Let us remind the authors of [40] and [41] that a 1D model being separated into phases is normally divided infinitely, since it has no free energy minimum [44].

ACKNOWLEDGMENTS

REFERENCES

1. Rudyak, V.M., Barkhausen Effect, *Usp. Fiz. Nauk*, 1970, vol. 101, no. 3, pp. 429–462.

2. Vazquez, M. and Adenot-Engelvin, A.-L., Glass–Coated Amorphous Ferromagnetic Microwires at Microwave Frequencies, *J. Magn. Magn. Mater.*, 2009, vol. 321, pp. 2066–2073.

3. Baranov, S.A., Berzhanskii, V.N., Zotov, S.K., Larin, V.S., and Torkunov, A.V., Ferromagnetic Resonance in Amorphous Magnetic Wires, *Fiz. Met. Metalloved.*, 1989, vol. 67, no. 1, pp. 73–78.

4. Baranov, S.A., Zotov, S.K., Larin, V.S., and Torkunov, A.V., Features of the Natural Ferromagnetic Resonance, *Fiz. Met. Metalloved.*, 1991, vol. 69, no. 12, pp. 172–174.

5. Mohri, K., Humphrey, F.R., Kawashimay, K., Kimura, K., and Mizutani, M., Large Barkhausen and Matteucci Effects in FeCoSiB, FeCrSiB and FeNiSiB Amorphous Wires, *IEEE Trans. Magn.*, 1990, vol. 26, no. 5, pp. 1789–1791.

6. Vazquez, M., Gomez-Polo, C., Theuss, H., and Kronmuller, H., Domain Structure and Magnetization Process of Bent Fe–Rich Amorphous Wires, *J. Magn. Magn. Mater.*, 1996, vol. 164, pp. 319–326.

7. Baranov, S.A., Karimova, G.V., and Lomaev, G.V., Domain Wall Movement in the Cast Amorphous Microwire, *Surf. Eng. Appl. Electrochem.*, 2006, vol. 42, no. 2, pp. 73–78.

8. Baranov, S.A., Estimation of Distribution of Residual Stresses in Core Amorphous Microwires, *Metal Sci. Heat Treatment*, 2001, vol. 43, nos. 3–4, pp. 167–168.

9. Baranov, S.A., Residual Stresses in the Core of an Amorphous Microwire, *Metal Sci. Heat Treatment*, 2003, vol. 45, nos. 7–8, pp. 280–282.

10. Baranov S.A., Vazquez, M., Garcia, K.L., and Usenco, V.P., Magnetic Properties of Amorphous Microwires, *Surf. Eng. Appl. Electrochem.*, 2004, vol. 40, no. 6, pp. 79–86.

11. Baranov, S.A., Laroze, D., Vargas, P., and Vazquez, M., Domain Structure of Fe–Based Microwires, *Phys. B*, 2006, vol. 372, pp. 324–327.

12. Panina, L.V. and Mori, K., Magneto–Impedance Effect in Amorphous Wires, *Appl. Phys. Lett.*, 1994, vol. 65, no. 9, pp. 1189–1196.

13. Baranov, S.A., Magnetic Properties of Co–Based Amorphous Microwire, *J. Magn. Magn. Mater.*, 2003, vol. 266, pp. 278–281.

14. Baranov, S.A., Laroze, D., Vargas, P., and Vazquez, M., On Micromagnetic Theory of Thin Cast Amorphous Microwires, *Phys. B*, 2006, vol. 372, pp. 320–323.

15. Antonov, A., Dykhne, A., Lagar'kov, A., and Usov, N., Structure of 90° Domain Wall in Co–Based Amorphous Wire, *Phys. A*, 1997, vol. 241, pp. 425–248.

16. Molokanov, V.V., Umnov, P.P., Kurakova, N.V., Sviridova, T.A., Shalygin, A.N., and Kovneristyi, Yu.K., How Thickness of Glass Coating Influences onto the Structure and Properties of Amorphous Soft Magnetic Co Alloy, *Perspekt. Mater.*, 2006, no. 2, pp. 5–14.

17. Velazquez, J., Vazquez, M., and Zhukov, A.P., Magnetoelastic Anisotropy Distribution in Glass–Coated Microwires, *J. Mater. Res.*, 1996, vol. 11, no. 10, pp. 2499–2505.

18. Antonov, A.S., Borisov, V.T., Borisov, O.V., Prokoshin, A.F., and Usov, N.A., Residual Quenching Stresses in Glass–Coated Amorphous Ferromagnetic Microwires, *J. Phys. D: Appl. Phys.*, 2000, vol. 33, pp. 1161–1168.

19. Chiriac, H., Ovari, T.-A., and Pop, Gr., Internal Stress Distribution in Glass–Covered Amorphous Magnetic Wires, *Phys. Rev. B*, 1995, vol. 52, no. 14, pp. 10104–10114.

20. Chiriac, H., Ovari, T.-A., Corodeanu, S., and Ababei, G., Interdomain Wall in Amorphous Glass–Coated

Microwires, *Phys. Rev. B*, 2007, vol. 76, pp. 214433-1—214433-8.

21. Brown, W.F., Jr., *Micromagnetics*, New York: Intersci. Publ., 1963.

22. Baranov, S.A., Residual Stress in Amorphous Microwire, *Surf. Eng. Appl. Electrochem.,* 2006, vol. 42, no. 6, pp. 44—46.

23. Miroshnichenko, S.I., *Zakalka iz zhidkogo sostoyaniya* (Quenching from the Liquid State), Moscow: Metallurgiya, 1982.

24. Manasevich, A.D., *Fizicheskie osnovy napryazhennogo sostoyaniya i prochnosti metallov* (Physical Foundations of Metals Stressed State and Durability), Moscow: Mashgiz, 1962.

25. Panin, V.E., Likhachev, V.A., and Grinyaev, Yu.V., *Strukturnye urovni deformatsii tverdykh tel* (Structural Levels of Solids Deformation), Novosibirsk: Nauka, 1985.

26. Timoshenko, S.P., *Soprotivlenie materialov* (Strength of Materials), Moscow: Nauka, 1965, vol. 2.

27. Filin, A.P., *Prikladnaya mekhanika tverdogo deformiruemogo tela* (Applied Mechanics of Deformed Solid), Moscow: Nauka, 1975, vol. 1, pp. 675—677.

28. Boley, B.A. and Weiner, J.H., *Theory of Thermal Stresses*, New York: John Willey and Sons, 1960, pp. 470—490.

29. Lyubimov, M.L., *Spai metalla so steklom* (Glass—Metal Seals), Moscow: Energiya, 1968, pp. 131—142.

30. Luganskii, L.B., The Way to Calculate the Mechanical Stresses in Solenoids (The Multi—Layer Model), *Zh. Tekh. Fiz.*, 1995, vol. 65, no. 12, pp. 120—131.

31. Amenzade, Yu.A., *Teoriya uprugosti* (The Theory of Elasticity), Moscow: Vysshaya Shkola, 1976.

32. Godfrey, D.E.R., *Theory of Plasticity and Plasticity for Engineers*, London: Thames and Hudson, 1965; Kiev: Budivel'nik, 1969.

33. Baranov, S.A., A Three—Layer Model of the Amorphous Microwire, *Surf. Eng. Appl. Electrochem.*, 2010, vol. 46, no. 3, pp. 271—275.

34. Baranov, S.A. and Stoianov, S.S., Experimental Measurement of a Tensing in a Microwire, *Surf. Eng. Appl. Electrochem.*, 2008, no. 2, pp. 98—105.

35. Doering, W., Switch Nucleation Growth under the Large Barkhausen Jumps, *Usp. Fiz. Nauk*, 1939, vol. 22, no. 1(5), pp. 78—92.

36. Landau, L.D. and Lifshits, E.M., To the Theory of Magnetic Permeability Dispersion in Ferromagnetic Solids, *Sov. Phys.*, 1935, vol. 8, pp. 153—166; Landau, L.D., *Sobranie trudov* (Collection of Works), Moscow: Nauka, 1969, vol. 1, pp. 125—143.

37. Karimova, G.V., Bi—Stable Cast Amorphous Glass—Coated Microwires Made of Fe, FeCo Alloys and Its Application in Magnetometry, *Extended Abstract of Cand. (Physmath.) Dissertation*, Izhevsk, 2006.

38. Perov, N.S., Radkovskaya, A.A., Antonov, A.S., Usov, N.A., Baranov, S.A., Larin, V.S., and Torcunov, A.V., Magnetic Properties of Short Amorphous Microwires, *J. Magn. Magn. Mater.*, 1999, vols. 196—197, pp. 385—387.

39. Lomaev, G.V., *Datchiki Barkgauzena* (Barkhausen Sensors), Izhevsk, 2008, pp. 23—31.

40. Gudoshnikov, S.A., Grebenshchikov, Yu.B., Ljubimov, B.Ya., Palvanov, P.S., Usov, N.A., Ipatov, M., Zhukov, A., and Gonzalez, J., Ground State Magnetization Distribution and Characteristic Width of Head to Head Domain Wall in Fe—Rich Amorphous Microwire, *Phys. Status Solidi A*, 2009, vol. 206, no. 4, pp. 613—617.

41. Gudoshnikov, S., Usov, N., Zhukov, A., Gonzalez, J., and Palvanov, P., Measurements of Stray Magnetic Fields of Amorphous Microwires Using Scanning Microscope Based on Superconducting Quantum Interference Device, *J. Magn. Magn. Mater.*, 2007, vol. 316, pp. 188—191.

42. Garcia-Miguel, H., Chen, D.-X., and Vazquez, M., Domain Wall Propagation in Bistable Amorphous Wires, *J. Magn. Magn. Mater.*, 2000, vol. 212, pp. 101—106.

43. Sixtus, K.J. and Tonks, L., Propagation of Large Barkhausen Discontinuities, *Phys. Rev.*, 1931, vol. 37, pp. 930—959.

44. Landau, L.D. and Lifshits, E.M., *Teoreticheskaya fizika* (Theoretical Physics), vol. 5, part 1: *Statisticheskaya fizika* (Statistical Physics), Moscow: Nauka, 1976, pp. 582—583.

Giant Magnetoresistance and Super-Paramagnetism in Electrodeposited NiFe/Cu Multilayers[1]

Sitra Esmaili[a], M. E. Bahrololoom[a], and C. Zamani[b]

[a]*Department of Materials Science and Engineering, School of Engineering, Shiraz University, Zand Blvd., Shiraz, Iran*
e-mail: esmaili@shirazu.ac.ir, esmaili_sitra@yahoo.com
[b]*Departament d'Electronica, Universitat de Barcelona, 08028 Barcelona, Spain*
Received December 27, 2010

Abstract—The giant magnetoresistance of electrodeposited NiFe/Cu multilayers from a single bath under potentiostatic control is studied. The observed nonsaturating behavior urged us to investigate the probability of the occurrence of superparamagnetic regions in these multilayers. In this research, for the first time, the presence of super-paramagnetic regions in electrodeposited NiFe/Cu multilayers is shown and proved via high resolution transmission electron microscopy. The reason was found to be the existence of a very large anodic transient at the beginning of the copper deposition pulse, which could be eliminated by choosing a more negative potential.

DOI: 10.3103/S1068375511040077

1. INTRODUCTION

A possible application of nanoscale multilayers exhibiting giant magnetoresistance (GMR) as magnetic field sensors has been the main driving force for the worldwide research into them. The first observation of GMR on sputtered magnetic/nonmagnetic multilayers [1, 2] was followed by the detection of the same effect in several electrodeposited multilayers such as CoCu/Cu [3], NiCu/Cu [4], CoNiCu/Cu [5, 6], NiFeCu/Cu [7, 8], CoFeCu/Cu [9] and quaternary CoFeNiCu/Cu [10].

It has been reported for several magnetic/nonmagnetic multilayer systems prepared by a variety of techniques such as sputtering [11, 12], MBE [13, 14] or electrodeposition [15–18] that the magnetization may contain both ferromagnetic (FM) and superparamagnetic (SPM) contributions. One can visualize the magnetic layers in such multilayers as consisting of both FM and SPM regions whereby the SPM regions are magnetically decoupled from the FM regions. A pictorial representation of such SPM regions can be in the form of small magnetic islands [17] within the magnetic layers surrounded by some magnetically diluted or completely nonmagnetic (NM) regions, ensuring magnetic decoupling from the FM regions. It has also been reported for the same systems that the magnetoresistance (MR) can exhibit a strongly nonsaturating behavior, sometimes up to magnetic fields of several tens of kOe. Since the saturation against an antiferromagnetic (AF) coupling in multilayers can be usually achieved in a few kOe, this nonsaturating MR component should have a different origin. Magnetic

measurements have revealed that in multilayers, in addition to the ferromagnetic (FM) term, the magnetization also has a superparamagnetic (SPM) term, the latter one sometimes even dominating over the FM contribution. The phenomenon of nonsaturating magnetoresistance and the occurrence of a SPM magnetization contribution are not restricted to any specific deposition technique or element combination. It is because, depending on layer's thicknesses and specific deposition conditions, they have been observed in multilayers of the Co/Au, Co/Cu, Ni/Cu, Ni–Fe/Cu, and Ni–Co/Cu systems grown by various methods such as molecular-beam epitaxy (MBE), sputtering, or electrodeposition [16].

According to Bakonyi and Peter [19], the actual physical appearance and location of these SPM regions in the multilayer structure has not yet been revealed. Nevertheless, evidence from the magnetic data clearly supports their possible presence in magnetic/nonmagnetic multilayers. Therefore, the aim of this paper is, firstly, to investigate the giant magnetoresistance of electrodeposited NiFe/Cu multilayers grown from a tailored single electrolyte. Secondly, to discuss the possibility of the existence of super-paramagnetic regions and to prove this idea with the aid of high-resolution transmission electron microscopy (HRTEM). The HRTEM studies do provide direct evidence for the actual physical appearance of these regions.

2. EXPERIMENTAL

2.1. Sample Preparation

The composition of the single electrolyte used was a modified version of an early work of Chang et al.
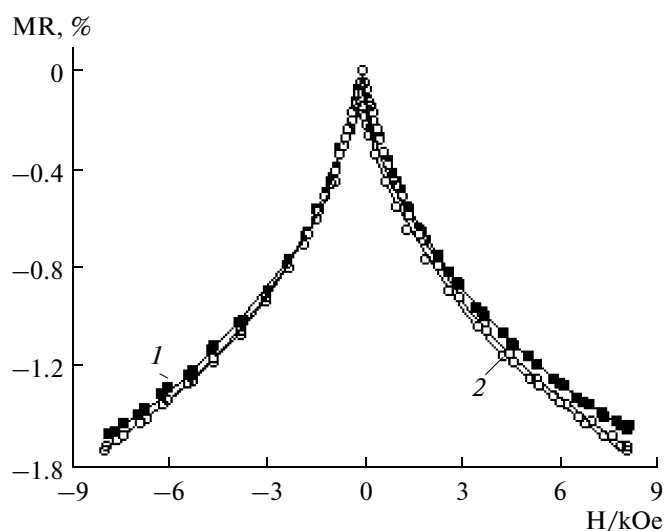
---

[1] The article is published in the original.

MR, %

Fig. 1. Magnetoresistance measured at room temperature for electrodeposited $[NiFe_{(3\ nm)}/Cu_{(1.2\ nm)}]_{150}$ multilayers. *1*—LMR; *2*—TMR.
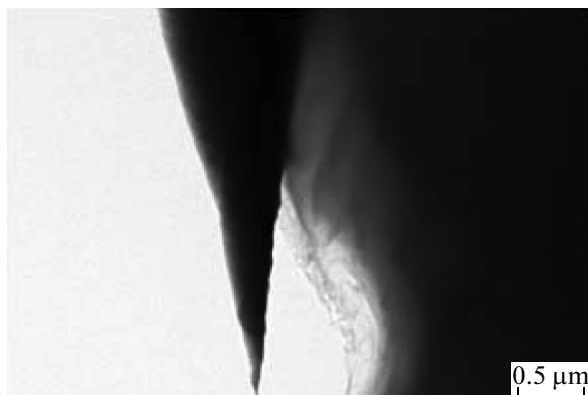

Fig. 2. General view of the sample after preparation by PIPS.

[20], i.e 0.4 M $NiSO_4$, 0.004 M $FeSO_4$, 0.01 M $CuSO_4$, and 0.2 M boric acid. A computer-controlled potentiostat was used to monitor the entire electrochemical process. The process was carried out at room temperature. The deposition potentials were chosen to be −2.5 V for the NiFe layer and −0.4 V for the Cu layer, measured relative to a saturated calomel electrode (SCE) that was placed in the cell. The computer controlled potentiostat switched between these two potentials. A Pt foil counter electrode was placed directly opposite the working electrode substrate. The layer thicknesses were controlled via the pulse lengths and from the charge deposited during the pulse, the nominal layer thicknesses were determined by Faraday's law. The thickness of the NiFe layer was estimated to be 3 nm, while the Cu layer thickness 1.2 nm. Electrodeposited were 150 repeats.

2.2. Morphological Investigations

A high-resolution transmission electron microscope operating at the voltage of 200 keV (0.23 resolution) was used for morphological studies. Cu foils, (200) oriented, 1 cm^2 in area, were used as substrates. In order to perform the HRTEM study, the samples were polished mechanically and then thinned by means of Ar^+ bombardment to achieve the appropriate thickness, which allows electrons to pass through the sample (around 100 nm). The samples were then mounted on a copper holder.

2.3. Giant Magnetoresistance Measurements (GMR)

The multilayers prepared for magnetotransport measurements were deposited onto Si(100)/Cr(5 nm)/Cu(20 nm). The Cr adhesive layer and the Cu seed layer were prepared by evaporation on the Si wafer.

The magnetoresistance was measured on 2 mm wide strips at room temperature with the four-point-in-line method in magnetic fields between −8 and +8 kOe in the field-in-plane/current-in-plane geometry. Both the longitudinal (LMR) and the transverse magnetoresistance (TMR) (field parallel to current and field perpendicular to current, respectively) components were recorded for each sample. The following formula was used for calculating the magnetoresistance ratio: $\Delta R/R_0 = (R_H - R_0)/R_0$ where R_H is the resistance in a magnetic field H and R_0 is the resistance value of the magnetoresistance peak around zero field. The shunt effect of the substrate was not corrected.

3. RESULTS AND DISCUSSION

The result of magnetoresistance measurements is shown in Fig. 1. A slow saturation is seen, which is an indication of a superparamagnetic (SPM) character. The SPM character of the GMR curves tells that the magnetic layer is either fragmented or quite rich in Cu, and there is some element segregation.

In order to investigate and ensure the presence of these super-paramagnetic regions, a HRTEM image was taken. Figure 2 shows the general view after sample preparation. Figures 3 and 4 show the HRTEM images of the electrodeposited $[NiFe_{(3\ nm)}/Cu_{(1.2\ nm)}]_{150}$ multilayers. It is evident that there was no layered structure detected. In many cases, only Cu was detectable. In some areas, however, Ni and Fe were also found. In those areas, the distribution of some nanoparticles is seen. Figure 5 shows the energy dispersive spectra (EDS) microanalysis corresponding to the area indicated shown in Fig. 4. Peaks of Fe and Ni are clearly seen. Large peaks correspond to Cu.
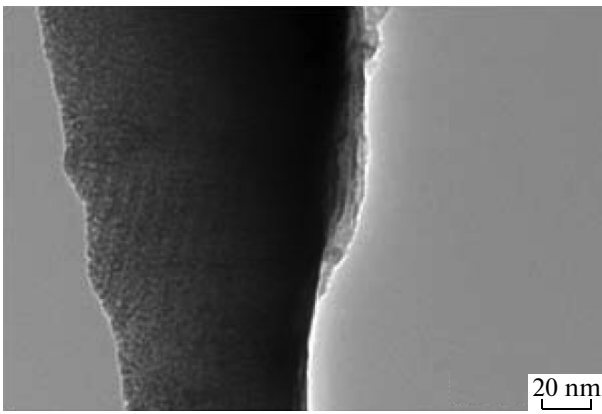
Fig. 3. The magnified area of the sample.

The first attempt to ascribe the nonsaturating magnetoresistance behavior to the presence of SPM regions was performed for MBE grown Co/Cu multilayers [21, 22]. Beyond technical saturation of the magnetization at about $H_s = 1.7$ kOe, the field dependence of both the magnetization M(H) and the magnetoresistance MR(H) has been described by the Langevin function L(x) where $L(x) = \mu H/kT$, with μ constituting the average magnetic moment of an SPM region. The magnitude of μ is typically in the range of $100-1000$ μ_B, where μ_B is the Bohr magneton. In the simultaneous presence of both FM and SPM regions, the GMR can contain three contributions [16]: (i) $GMR_{SPM-SPM}$, (ii) GMR_{FM-FM} and (iii) GMR_{SPM-FM}, where by a term GMR_{A-B} means a spin dependent scattering event for an electron path "magnetic region" A nonmagnetic region magnetic region B. Each of these three cases makes a completely different contribution to the field dependence of the magnetoresistance MR(H) since for an SPM particle, a large magnetic field (typically well in excess of 10 kOe) is needed to align its magnetic moment whereas the moment of a FM particle is aligned in a much smaller magnetic field, typically in a few kOe.

As seen in Fig. 4, an assembly of SPM particles is embedded in the copper matrix in a manner that there is a sufficient separation distance between the particles so that there in no magnetic interaction between their magnetic moments. A conduction electron just leaving a SPM entity is polarized by the magnetic moment of the particle. If this electron travels in the copper matrix and arrives at a neighboring SPM particle in a time shorter than its spin-memory time (i.e., it arrives with its original spin orientation), then at the second SPM particle it will undergo a spin-dependent scattering event since the orientations of the two SPM moments are uncorrelated. This spin-dependent scattering gives rise to a GMR contribution just as in the case of ferromagnetic/nonmagnetic multilayers when electrons travel via the nonmagnetic spacer between the two ferromagnetic layers of different magnetization orientations [19].

The three governing factors controlling the appearance of the SPM regions have been identified. These factors are discussed as follows. The improper choice of the deposition potential of the nonmagnetic metal, which can result in a significant increase of the GMR_{SPM} fraction [19]. In the case of immiscible elements such as Co and Cu, the tendency for the formation of SPM regions was found to be larger when the content of Cu in the magnetic layer increases [23].

A large GMR_{SPM} term may develop also for the sputtered Co/Cu multilayers deposited on rough Ta substrates (mechanically polished Ti foil) with respect to identical conditions on a smooth substrate (Si wafer with evaporated Ta or Cr adhesive and Cu seed layers) [24, 25].

The reason of the SPM character found in our samples could also be explained in Fig. 6 that shows the typical current-time response during the pulse potential deposition of sample 8. A very large anodic transient at the beginning of the Cu pulse is depicted, which means that there is a significant dissolution at the beginning of the pulse until Cu fully covers the surface. The dissolution of the magnetic layer contributes to both the interface roughening and the fragmentation of the magnetic layer. To overcome this problem either the Cu deposition potential should be chosen to
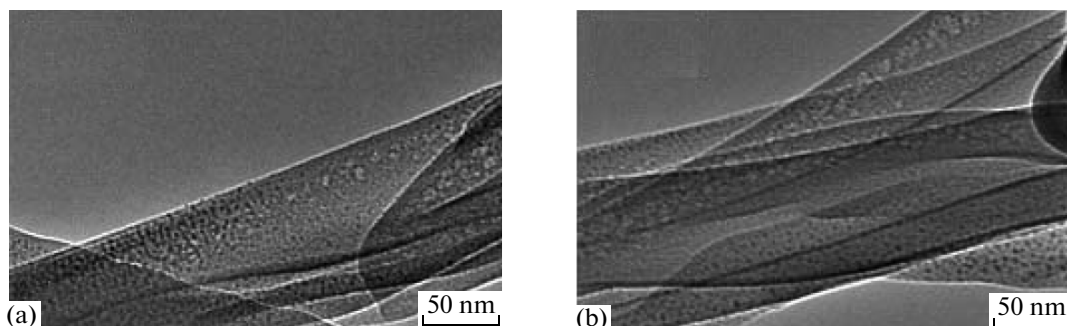

Fig. 4. Super-paramagetic (SPM) regions including the small islands of NiFe electrodeposited in the matrix of Cu.
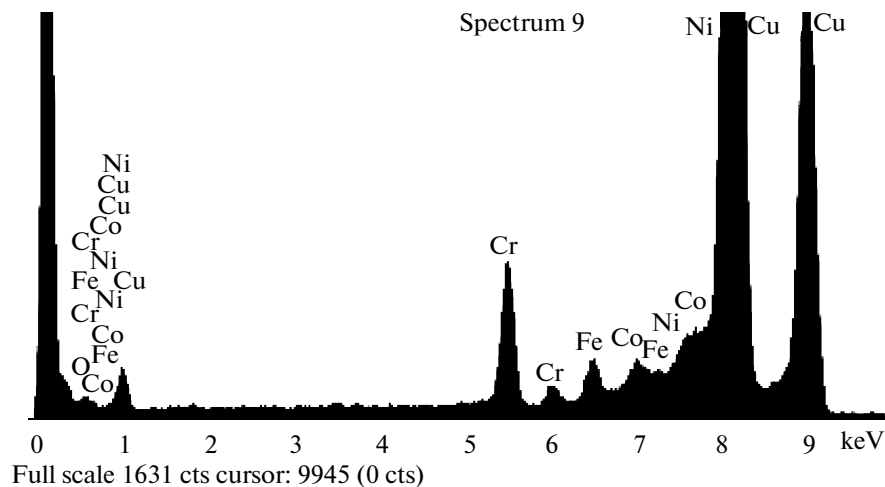
Fig. 5. A microanalysis (EDS spectra) corresponding to the area indicated in above image. Peaks of Fe and Ni are clearly seen, large peaks correspond to Cu.
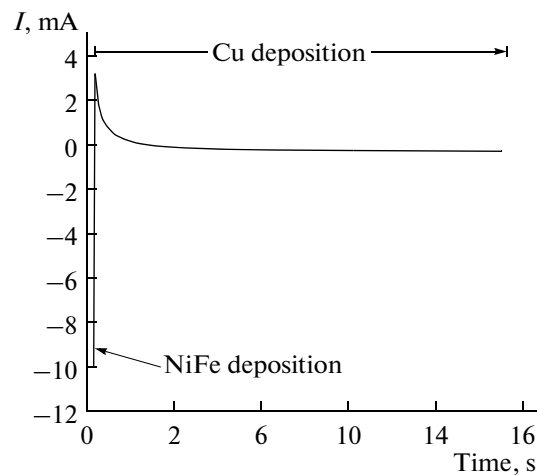

Fig. 6. Typical current-time response of one cycle during the pulse potential deposition.

be more negative or the pulse length should be increased.

4. CONCLUSIONS

The inferior GMR characteristics of electrodeposited multilayers as compared to physically deposited multilayers can be ascribed to microstructural features leading to the appearance of SPM regions, pinholes in the spacer layers and not sufficiently perfect interfaces. In this research, for the first time, the presence of SPM regions in the electrodeposited NiFe/Cu multilayers was proved with the aid of high resolution transmission electron microscopy. The reason for that behavior was found to be the improper choice of the deposition potential. It is possible to improve the quality of layers and increase the thickness of magnetic layers in order to obtain higher magneto resistances and eliminate the SPM regions.

REFERENCES

1. Baibich, M.N., Broto, J.M., Fert, A., Van Dau, F.N., Petroff, F., and Etienne, P., Giant Magnetoresistance of (001)Fe/(001)Cr Magnetic Superlattices, *Phys. Rev. Lett.*, 1988, vol. 61, pp. 2472–2475.

2. Binasch, G., Grunberg, P., Saurenbach, F., and Zinn, W., Enhanced Magnetoresistance in Layered Magnetic Structures with Antiferromagnetic Interlayer

Exchange, *Phys. Rev., Ser. B*, 1989, vol. 39, pp. 4828–4830.

3. Liu, Q.X., Péter, L., Toth, J., Kiss, L.F., Cziraki, A., and Bakonyi, I., The Role of Nucleation in the Evolution of Giant Magnetoresistance with Layer Thicknesses in Electrodeposited Co–Cu/Cu Multilayers, *J. Magn. Magn. Mater.*, 2004, vol. 280, pp. 60–74.

4. Toth, J., Kiss, L.F., Toth-Kadar, E., Dinia, A.,. Pierron-Bohnes, V., and Bakonyi, I., Giant Magnetoresistance and Magnetic Properties of Electrodeposited $Ni_{81}Cu_{19}$/Cu Multilayers, *J. Magn. Magn. Mater.*, 1999, vols. 198-199, pp. 243–245.

5. Alper, M., Attenborough, K., Hart, R., Lane, S.J., and Younes, C., Giant Magnetoresistance in Electrodeposited Superlattices, *Appl. Phys. Lett.*, 1993, vol. 63, pp. 2144-2146.

6. Nabiyouni, G., Schwarzacher, W., Rolik, Z., and Bakonyi, I., Giant Magnetoresistance in Ni–Co–Cu/Cu Multilayers, *J. Magn. Magn. Mater.*, 2002, vol. 253, pp. 77–85.

7. Attenborough, K., Hart, R., Lane, S.J., Alper, M., and Schwarzacher, W., Magnetoresistance in Electrodeposited Ni–Fe–Cu/Cu Multilayers, *J. Magn. Magn. Mater.*, 1995, vol. 148, pp. 335–336.

8. Chassaing, E., Nallet, P., and Trichet, M.F., Electrodeposition of $Cu/Fe_{20}Ni_{80}$ Multilayers, *J. Electrochem. Soc.*, 1996, vol. 143, P. L98–L100.

9. Kakuno, E.M., Da Silva, R.C., Mattoso, N., Schreiner, W.H., Mosca, D.H., and Teixeira, S.R., Giant Magnetoresistance in Electrodeposited $Co_{87}Fe_{13}$/Cu Compositionally Modulated Alloys, *J. Phys., Ser. D*, 1999, vol. 32, pp. 1209–1213.

10. Huang, Q., Young, D.P., Chan, J.Y., Jiang, J., and Podlaha, Ej., Electrodeposition of FeCoNiCu/Cu Compositionally Modulated Multilayers, *J. Electrochem. Soc.*, 2002, vol. 149, pp. C349–C354.

11. Wu, M. and Abdul-Razzaq, W., Spin-Glass-Like Behavior in Cu/Ni Multilayered Films, *Phys. Rev., Ser. B*, 1990, vol. 42, pp. 4590-4593.

12. Vavassori, P., Spizzo, F., Angeli, E., Bisero, D., and Ronconi, F., Evolution from Multilayer to Granular Behavior via Cobalt Layers Fragmentation in Co/Cu Multilayers, *J. Magn. Magn. Mater.,* 2003, vol. 262, pp. 120–123.

13. Xu, J., Howson, M.A., Hickey, B.J., Greig, D., Veillet, P., and Kolb, E., Giant Magnetoresistance and Superparamagnetism in Co/Au Multilayers, *J. Magn. Magn. Mater.*, 1996, vol. 156, pp. 379–380.

14. Xu, J., Howson, M.A., Hickey, Bj., Greig, D., Kolb, E., Veillet, P., et al., Superparamagnetism and Different Growth Mechanisms of Co/Au(111) and Co/Cu(111) Multilayers Grown by Molecular-Beam Epitaxy, *Phys. Rev., Ser. B*, 1997, vol. 55, pp. 416–422.

15. Tokarz, A., Wolkenberg, A., and Przeslawski, T., Magnetic Properties of Electrochemically Deposited Ni/Cu Superlattices, *J. Electrochem. Soc.*, 2002, vol. 149, pp. C607–C609.

16. Bakonyi, I., Péter, L., Rolik, Z., Kiss-Szab, K., Kupay, Z., Tóth, J., et al., Decomposition of the Giant Magnetoresistance of Multilayers into Ferromagnetic and Superparamagnetic Contributions, *Phys. Rev., Ser. B*, 2004, vol. 70, p. 054427/1–10.

17. Bakonyi, L, Tóth, J., Kiss, L.F., Tóth-Kadar, E., Péter, L., and Dinia, A., Origin of GMR Contributions in Electrodeposited Ni-Cu/Cu Multilayers, *J. Magn. Magn. Mater.*, 2004, vol. 269, pp. 156–167.

18. Péter, L., Rolik, Z., Kiss, L.F., Tóth, J., Weihnacht, V., Schneider, C.M., et al., Temperature Dependence of the Giant Magnetoresistance and Magnetic Properties in Electrodeposited Co–Cu/Cu Multilayers: the Role of Superparamagnetic Regions, *Phys. Rev., Ser. B*, 2006, vol. 73, pp. 174410/1–10.

19. Bakonyi, I. and Péter, L., Electrodeposited Multilayer Films with Giant Magnetoresistance (GMR): Progress and Problems, *Prog. Mater. Sci.*, 2010, vol. 55-3, pp. 107–245.

20. Chang, J.W. and Romankiw, L.T., Electrodeposited Superlattices of CoFe/Cu and NiFe/Cu on n-Type (111) Si Single Crystal Wafers, in *Magnetic Materials, Processes, and Devices III*, Romankiw, L.T. and Herman, D.A., Jr., Ed., Pennington (NJ): The Electrochemical Society Proceedings Series, 1994, vol. [PV94-6], pp. 223–232.

21. Barlett, D., Tsui, F., Glick, D., Lauhon, L., Mandrekar, T., Uher, C., et al., Langevin-Like Giant Magnetoresistance in Co–Cu Superlattices, *Phys. Rev., Ser. B*, 1994, vol. 49, pp. 1521–1521.

22. Clarke, R., Barlett, D., Tsui, F., Chen, Bx., and Uher, C., An Alternate Route to Giant Magnetoresistance in MBE-Grown Co–Cu Superlattices, *J. Appl. Phys.*, 1994, vol. 75, pp. 6174–6177.

23. Liu, Qx, Péter, L, Padar, J., and Bakonyi, I., Ferromagnetic and Superparamagnetic Contributions in the Magnetoresistance of Electrodeposited Co–Cu/Cu Multilayers, *J. Electrochem. Soc.*, 2005, vol. 152, pp. C316–C323.

24. Cziraki, A., Péter, L., Weihnacht, V., Tóth, J., Simon, E., Padar, J., et al., Structure and Giant Magnetoresistance Behaviour of Co–Cu/Cu Multilayers Electrodeposited under Various Deposition Conditions, *J. Nanosci. Nanotechnol.*, 2006, vol. 6, pp. 2000–2012.

25. Péter, L, Weihnacht, V., Tóth, J., Padar, J., Pogany, L., Schneider, C.M., et al., Influence of Superparamagnetic Regions on the Giant Magnetoresistance of Electrodeposited Co–Cu/Cu Multilayers, *J. Magn. Magn. Mater.*, 2007, vol. 312, pp. 258–265.

Formation of Composite Coatings Based on Titanium Carbide via Electrospark Alloying

F. I. Panteleenko[a], V. V. Sarantsev[a], A. M. Stolin[b], P. M. Bazhin[b], and E. L. Azarenko[a]

[a]*Belarusian State Technical University, pr. Nezavisimosti 65, Minsk, 220013 Republic of Belarus*
[b]*Institute of Structural Macrokinetics and Materials Science, Russian Academy of Sciences,*
Chernogolovka, Moscow oblast, 142432 Russia
e-mail: BNTU_MTF@mail.ru
Received December 3, 2010; in final form, January 14, 2011

Abstract—This work concerns studying the coatings prepared via electrospark alloying. To deposit the coatings, we used STIM-2/30 electrodes derived from a combination of self-propagating high-temperature synthesis (SHS) and extrusion. It was found that the composite coating is formed from titanium carbides and a solid solution of nickel in iron and contains both large (4–5 μm) and small carbides (less than 1 μm); in addition, large grains of titanium carbide are formed in the central portion of the coating, and the grain size decreases to 100 nm while approaching the transition zone. Large grains of titanium carbide in the coating consist of dispersed carbides with sizes less than 1 μm. It is determined that the composition of the substrate has an effect on the size of the transition and diffusion zones. It ranges from 17 μm for steel 9KhSA to 26 μm for steel 20; that is, the higher the degree of alloying, the less the depth of the modified layer.

INTRODUCTION

The development and implementation of new technologies for forming composite coatings on the working surfaces of machine parts and mechanisms are of current concern for the industry in any country.

PROBLEM FORMULATION AND EXPERIMENTAL

In [1, 2], the feasibility of using self-propagating high-temperature synthesis (SHS) and the method of electrospark alloying (ESA) to form high-quality composite coatings (CCs) is shown. The authors of [3] prove the possibility of using a combination of SHS processes and the shear plastic deformation of synthesized materials (SHS extrusion) to prepare electrodes for ESA. The SHS-extrusion method provides the synthesis of the material and the production of the workpiece in one installation and combines the advantages of both extrusion (the possibility to prepare products with a desired profile with minimum subsequent machining) and SHS technology (economic efficiency, the simplicity of the equipment, a short process life, and an operation that does not require high efforts during deformation and energy consumption for the external heating of semimanufactured products).

The advantageous use of SHS electrodes requires studying the properties of the resulting coatings, the structural and phase transformations, and the distribution of the elements in the "coating–substrate" system during the formation of the hardening layer. In [3], the laws of structure formation in the electrode material during SHS extrusion were studied. This work represents a more detailed study of the microstructure and phase formation in a CC deposited using a STIM-2/30 SHS-electrode. The composition of the electrode is 70% TiC + 30% Ni [4]. We selected substrates of steel 20, 45, U8, and 9KhSA. The CCs were deposited using an EES-3 installation (Resti, Izhevsk) with a maximum unit pulse intensity of 20 J and an electromechanical vibrator (OAO VTI, Moscow) with an oscillation frequency up to 100 Hz.

To prepare coatings with the maximum possible thickness in one pass using a STIM-2/30 SHS-electrode (⌀2 mm), it is necessary to use high-power deposition modes. However, the electrodes based on titanium carbide spalled during the deposition of the coatings at a high power (above 5–20 J) because of the thermal stresses. Therefore, the optimum energy of the unit pulses that leads to the uniform melting of an STIM-2/30 electrode and the formation of a continuous coating (95%) is $W = 5$ J; in addition, a coating with a thickness of 80–100 μm is formed in one pass. The rate of the electrospark machining in the case of the coating's deposition by hand using an STIM-2/30 electrode is 2 cm^2/min.

The microstructure of the powder and coatings was examined in transverse sections using a Mira high-resolution scanning electron microscope (Tescan, Czech Republic) with an INCA Energy 350 X-ray microanalyzer. The studies were carried out both pointwise
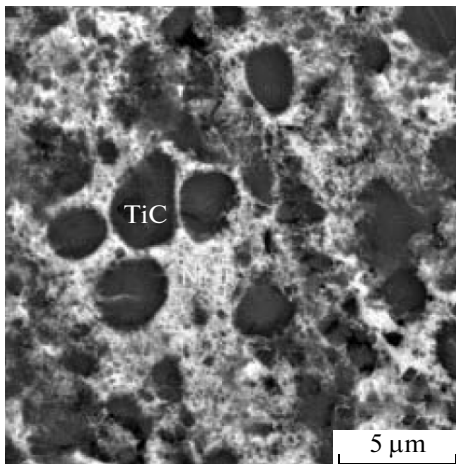
Fig. 1. Microstructure of a STIM-2/30 electrode.

(a point-by-point X-ray spectral microprobe analysis (XSMA)) with concentration distribution curves and via photography in characteristic X-ray radiation using the Cameo+ software program. The pattern of the distribution of the element under study was shown on a screen using a color display. The concentration of the element is determined according to the color density.

RESULTS AND DISCUSSION

The composition of the electrodes has a significant effect on the quality of coatings in ESA. The most promising electrodes are hard-alloy materials, which can be prepared using several methods: the formation of the electrodes from powders with subsequent sintering, the preparation of materials via drawing from a metal melt, and the casing of powders.

The electrodes prepared from powder materials are of greatest interest. Via mixing the original powders in certain proportions, we can select the desired compositions for coatings with the necessary properties.

STIM-2/30 SHS electrodes are characterized by a matrix structure: fragile particles of titanium carbide TiC (the dark grains in Fig. 1), which are close to a spherical shape, are located in a viscous matrix of nickel (the bright area). The studies showed that the characteristic grain sizes in an arbitrary direction (including longitudinal and transverse sections) are approximately the same, which further proves the spherical shape of the titanium carbide grains. The sizes of the TiC are 0.2 to 6.0 μm.

Figure 2 shows the images of the cross sectional structure of a coating deposited on a substrate of steel 20 using a STIM-2/30 electrode. In this case, a dense nonporous surface is formed. The upper portion of the coating (Fig. 2) exhibits a homogeneous dispersed structure with round grains of titanium carbide distributed in it. The presence of titanium carbide in the dark structural components is proved by the results of the point-by-point XSMA of the distribution of carbon and titanium. The distribution of titanium (Fig. 3) follows the distribution of carbon, which confirms the fact that bound titanium is present in the form of carbides with a grain size of 0.2 to 3.0 μm in the CC. Two types of structural components of a round and elongated shape are present in the central portion of the coating. The elongated shape of the particles is indic-
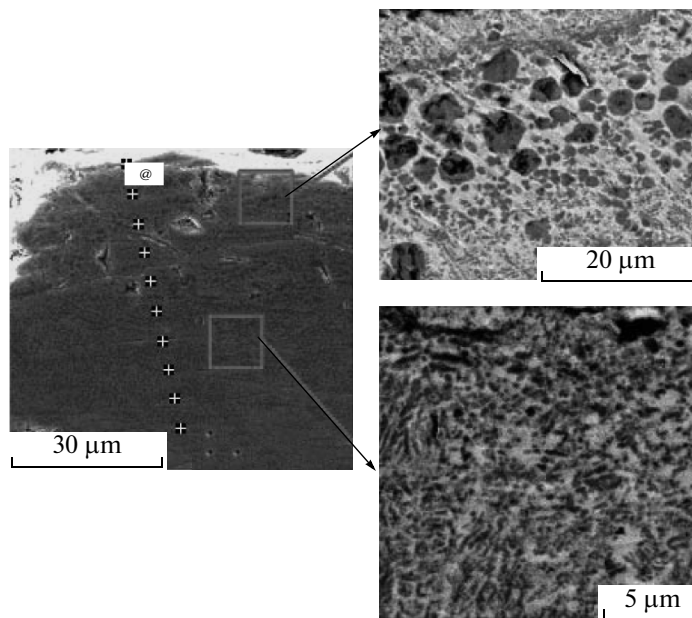

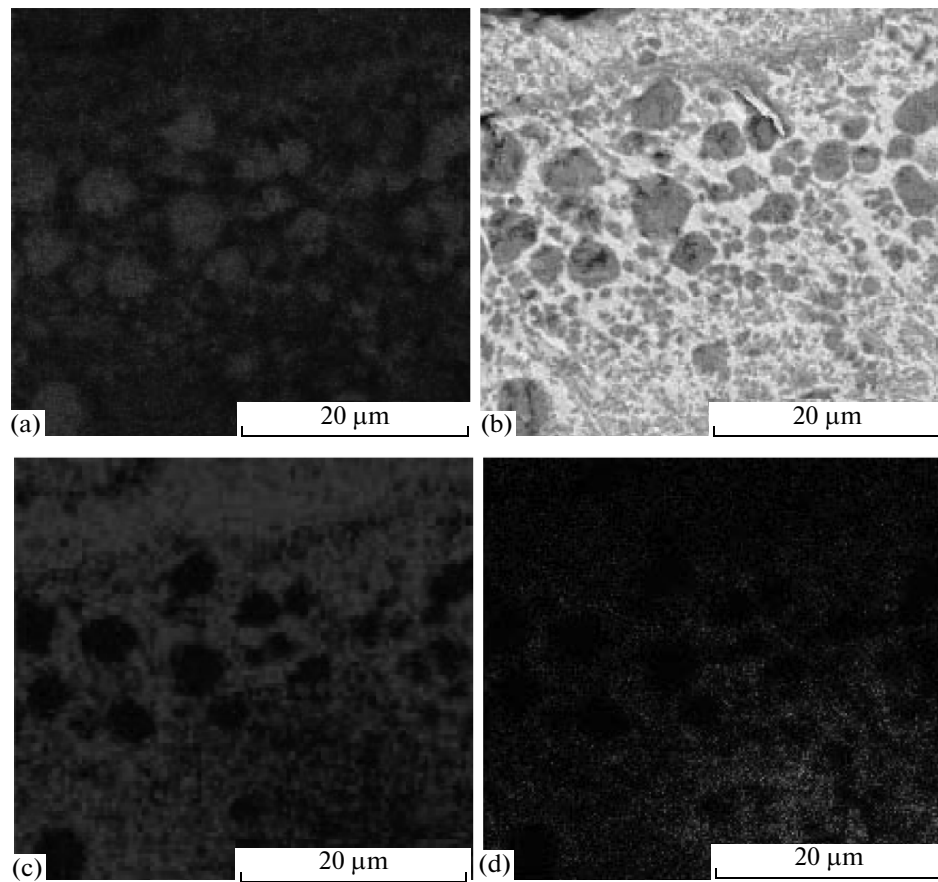**Fig. 2.** Microstructure of the central portion of the CC (the base is steel 20).

Fig. 3. Photograph of the CC in characteristic X-ray radiation: (a) Ti, (b) C, (c) Ni, and (d) Fe.

ative of the direction of motion of the heat removal during their formation.

A more detailed examination of the near-surface portion of the coating (see Fig. 2) reveals large grains of titanium carbide. The grain size in the upper por-

Fig. 4. Concentration distribution of elements in the CC.

tion of the CC is similar to the grain size of titanium carbide in the electrode (see Fig. 1). In the central and lower portions of the coating, a size reduction of the titanium carbide grains is observed. The presence of small round structural components and larger dendrite-like elongated structural entities is revealed. In addition, it is clearly seen that the dendrite-like particles consist of smaller round particles with a size of less than 100 nm. The distribution of carbon suggests that the carbide particles are both round and dendrite-like. This feature is attributed to the passage of the electrode material through a microplasma gap; according to [5], the temperature in the gap can achieve 10000–11000°C. The partial melting of titanium carbide grains with the subsequent rapid cooling caused by heat removal into the material of the base leads to the formation of a fine-grained structure (the grain size of the TiC is no more than 0.2 μm). Large grains of TiC are transferred to the coating during the contact of the heated electrode face and the substrate.

The distribution of elements shows that iron and nickel are concentrated between the particles of titanium carbide (see Fig. 3). They poorly dissolve in titanium carbide and do not form ternary compounds with it [6]; they are contained in the form of a solid
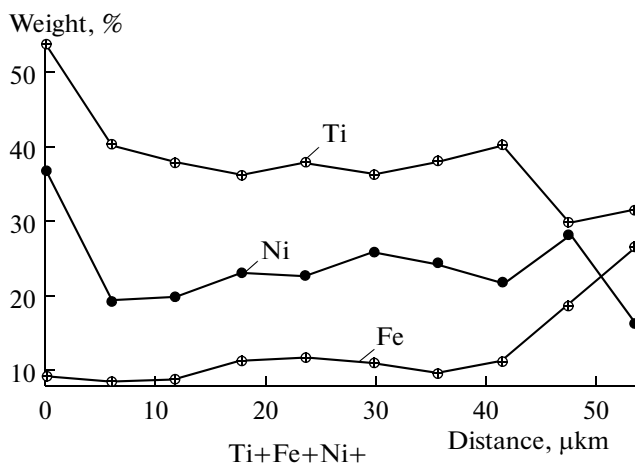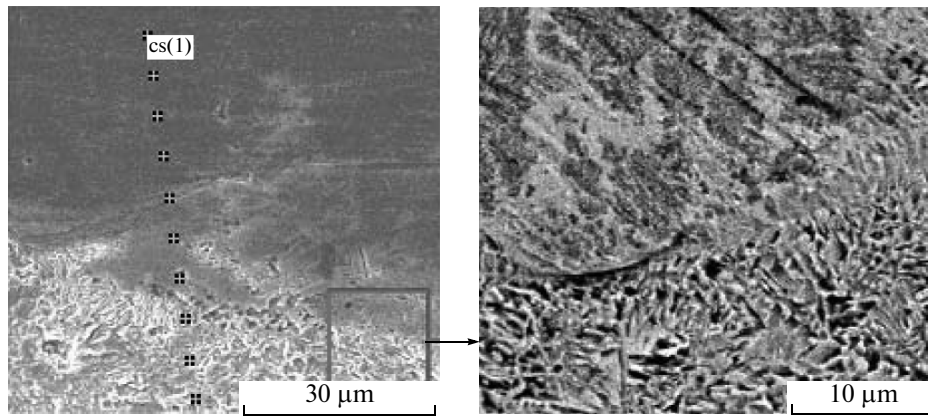
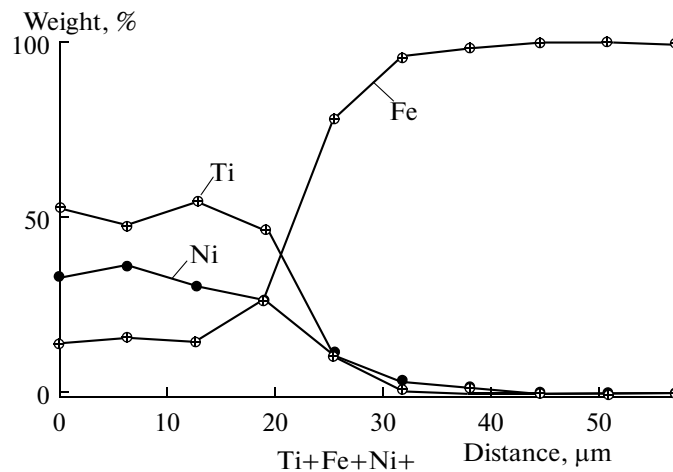**Fig. 5.** Microstructure of the transition zone (the base is steel 20).

Fig. 6. Concentration distribution of elements in the transition zone.

solution of Ni in Fe [7]. According to XSMA (Fig. 4), the distribution of elements in the CC is uniform. At the points with a decreased titanium concentration, the amount of iron and nickel increases; this is consistent with the above conclusions.

The distribution of iron in the coating is nonuniform (see Figs. 3, 4). The presence of iron in the coating is indicative of the partial melting of the base. The concentration of iron increases while approaching the base. Iron is almost absent in the regions of the coating that contain titanium and nickel. According to the distribution of iron and titanium, we can assume that titanium mostly forms carbides of a round shape, and the dendrite-like carbides have a more complex composition; in addition to Ti, they partially contain Fe (see Figs. 2, 3).

At the coating−base interface, a small modified zone of the steel base is observed (Fig. 5); the presence of round fine particles of titanium carbide and mostly dendrite-like carbides is clearly seen. The pattern of the change in the content of titanium in the CC and in

the base metal suggests that titanium is present both in the composition of the carbide and in the form of a solid solution in iron.

A decrease in the concentration of nickel and titanium with a simultaneous increase in the content of iron occurs at the coating−base interface (see Fig. 6). Unlike titanium, the decrease in the amount of nickel is more gradual, which is indicative of the presence of nickel in the form of a solid solution in iron.

Figure 7 shows the cross sectional images of the upper portion of the coating formed on a substrate of steel 45. It is clearly seen in the microstructure that the surface layer of the CC contains mostly large round grains of titanium carbide. The structure of the coating is similar to that of the electrode (see Fig. 1). However, small particles of TiC are shifted to the lower portion of the coating. This suggests that the coating was formed in the presence of an abundant liquid phase for a long time interval. The long period of time was provided by the repeated hitting of the electrode at one
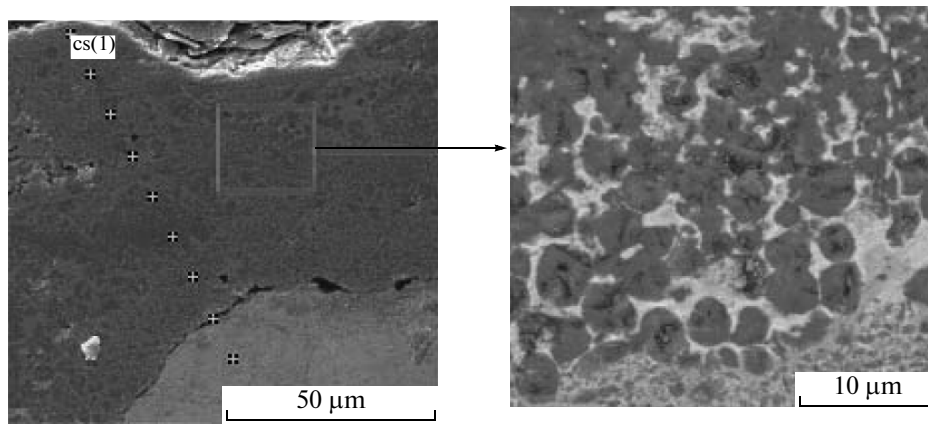
Fig. 7. Microstructure of the central portion of the CC (the base is steel 45).
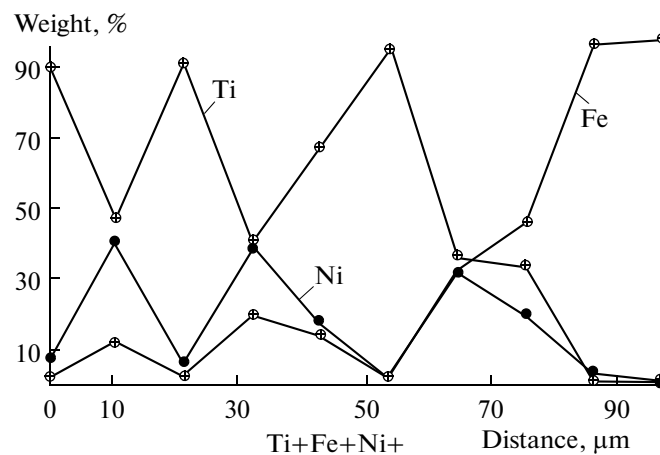

Fig. 8. Concentration distribution of elements in the CC.

point during the ESA. A bilayer coating was formed as a result.

The main elements of the dark structural components are titanium and carbon, which implies that they are grains of titanium carbide, whose reflections are present in the diffraction patterns (Fig. 8). According to the XSMA, the gray region that surrounds the particles of titanium carbide contains Ni and Fe.

In the central portion (the transition zone) of the coating, a gradual transition from large (~5–7 μm) to smaller carbide particles (≤1 μm) is observed (Fig. 9). Small particles of titanium carbide are located in the lower portion of the coating. Generally, an ultrafine structure of a CC is formed in the presence of an abundant melt and at a high cooling rate owing to the heat removal deep into the substrate. Iron and nickel are located in the same zones between carbide particles and form a solid solution. According to XSMA, a gradual decrease in the content of titanium and nickel

in the direction of the substrate is observed in the central portion of the coating (Fig. 10).

The substrate layer adjacent to the coating (steel 45) has a quenching dendrite-like structure derived under conditions of rapid cooling.

Figure 11 shows the microstructure of the cross section of the coating formed on steel U8. Photography in characteristic X-ray radiation showed that titanium carbide is almost uniformly distributed throughout the entire thickness of the coating. Along with large round particles, small dispersed particles of titanium carbide are observed. Large particles with a size of 3–5 μm are concentrated in the central portion of the CC.

The concentration distribution of the elements over the cross section of the coating (Fig. 12) is similar to that of the above described samples: TiC is uniformly distributed over the entire coating.

The study of the transition zone (Fig. 13) showed a decrease in the concentration of titanium carbide and
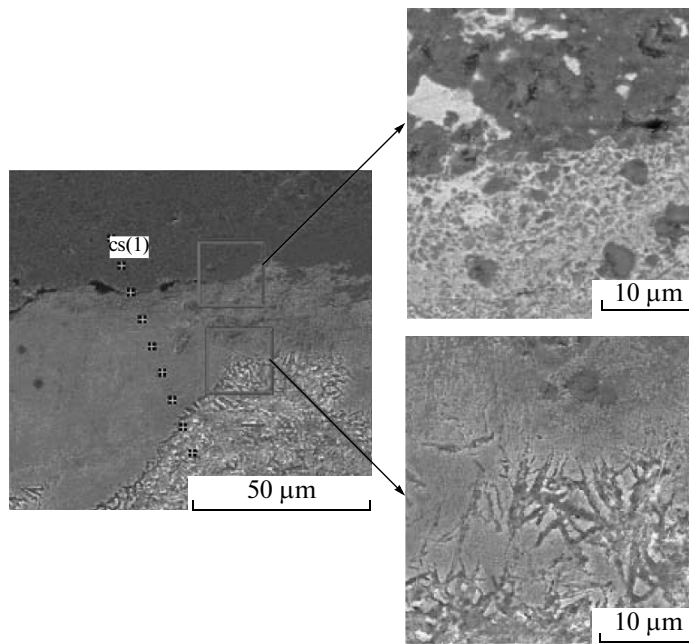
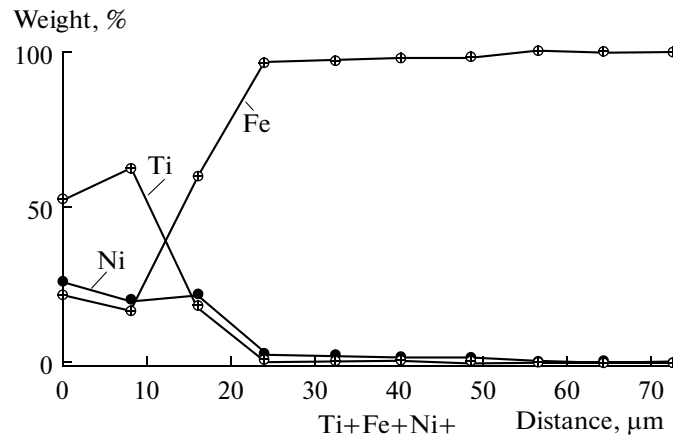**Fig. 9.** Microstructure of the transition zone (the base is steel 45).

Fig. 10. Concentration distribution of elements in the transition zone.

nickel with a simultaneous increase in the amount of iron (Fig. 14). A pronounced transition zone is formed from the partially melted substrate and the molten electrode material. The presence of fine grains of titanium carbide with an elongated needle-like shape is revealed in the transition zone.

An insignificant amount of titanium—no more than 5%—is observed in the material of the base.

The structure and composition of the coating (Figs. 15, 16) formed on steel 9KhSA are similar to the above discussed coatings. In this case, large particles of titanium carbide with a round shape are also formed in the central portion of the coating. At high magnification, the formation of agglomerates of small particles

is revealed. This fact can be indicative of a slow cooling of the sample during formation, which allows the carbide particles to grow to large sizes.

While approaching the transition zone, the number of large particles decreases (Fig. 17). The comparison of the distributions of the titanium and carbon showed that the concentration of titanium is higher than that of carbon. This fact suggests that titanium is present in the central portion of the coating both in the form of carbides and in its pure form. The central portion of the coating hardly contains iron at all (see Fig. 16). Nickel is uniformly located both in the form of a solid solution in iron and independently between the particles of titanium carbide.
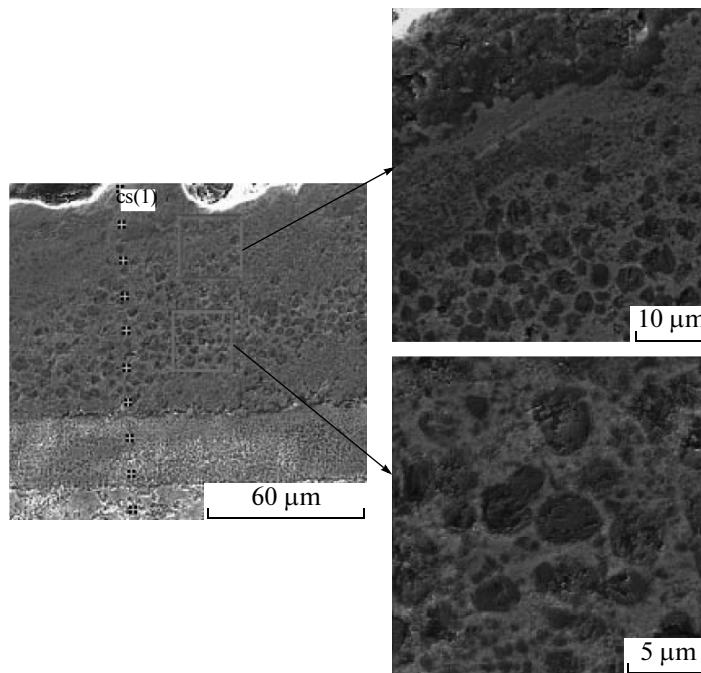
Fig. 11. Microstructure of the central portion of the CC (the base is steel U8).
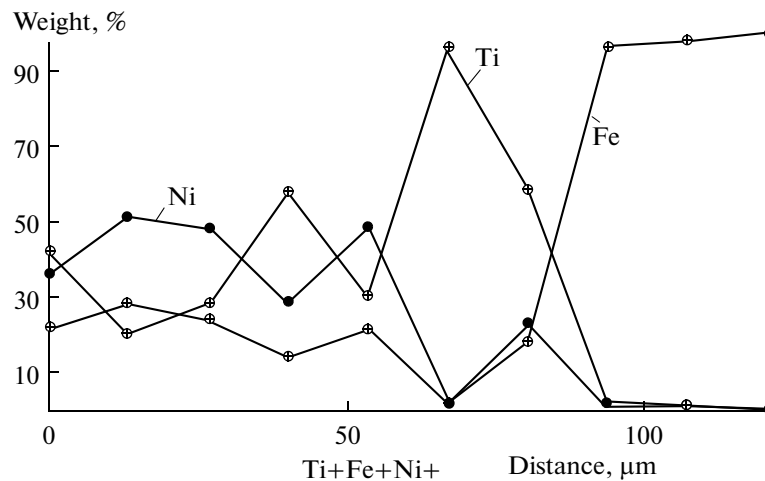

Fig. 12. Concentration distribution of elements in the CC.

Figures 17 and 18 show the structure and distribution of the elements in the transition zone. At the coating−base interface, a monolithic continuous layer is formed. Upon the superposition of the distribution of iron on the coating's structure, it was found that, along the coating with the base, there is a thin layer with the maximum concentration of iron. This structure is characteristic of the material that contains alloying elements; in this particular case, they are Cr, Ti, Si, and Ni, which penetrated from the base.

CONCLUSIONS

For the coatings formed via ESA using STIM-2/30 SHS electrodes, there was found the following:

—A continuous dense CC with a thickness of 80 to 100 μm without micro- and macrocracks is formed in one pass.

—The deposition of a coating is accompanied by the partial melting of the substrate material (iron) and its intermixing with the electrode material; in addition, the diffusion of nickel into the base is almost

Fig. 13. Microstructure of the transition zone (the base is steel U8).

Fig. 14. Concentration distribution of elements in the transition zone.

Fig. 15. Microstructure of the central portion of the CC (the base is steel 9KhSA).

Fig. 16. Concentration distribution of elements in the CC.
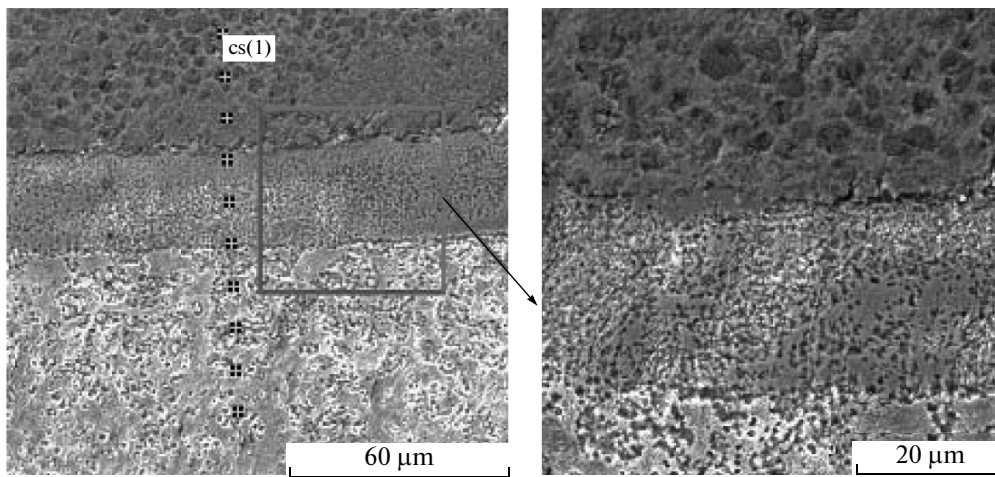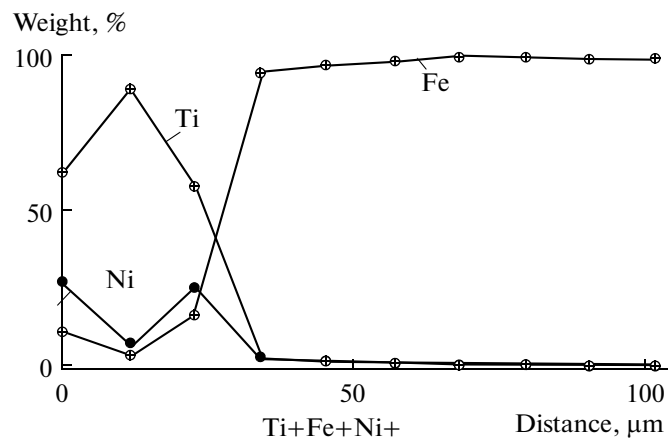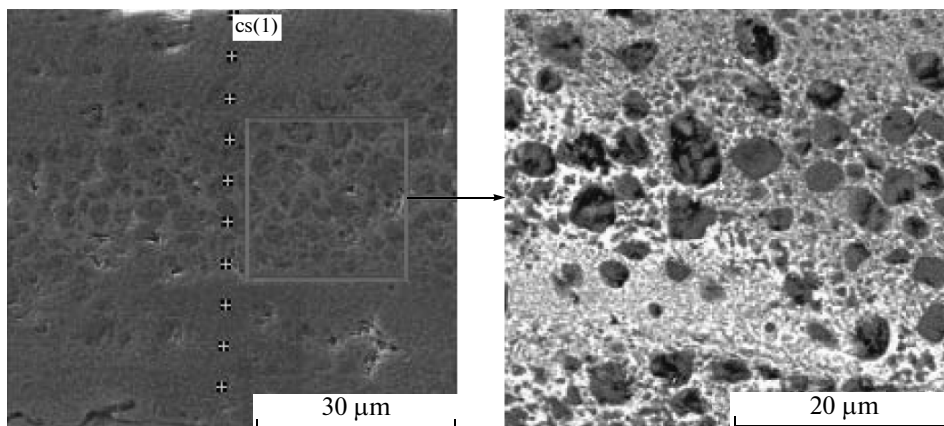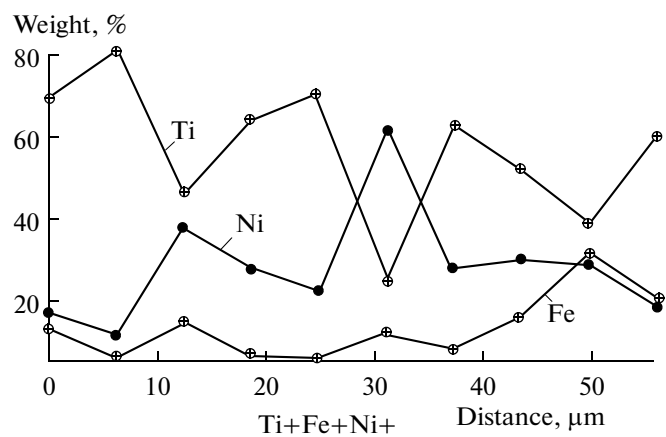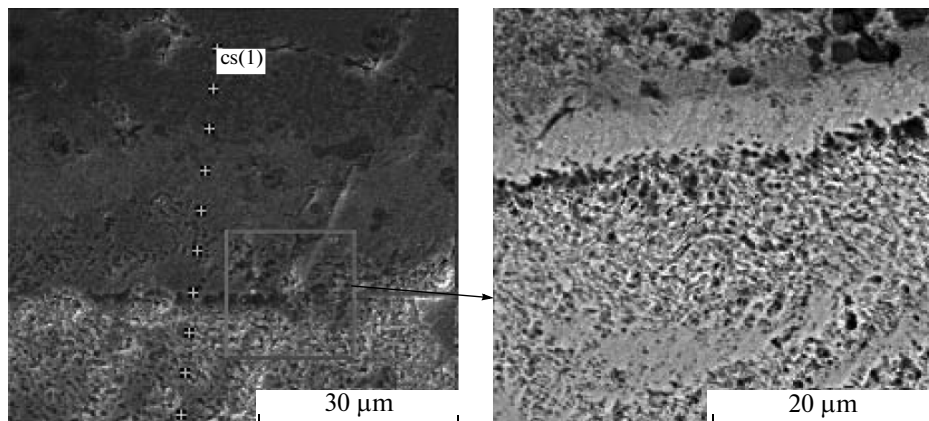

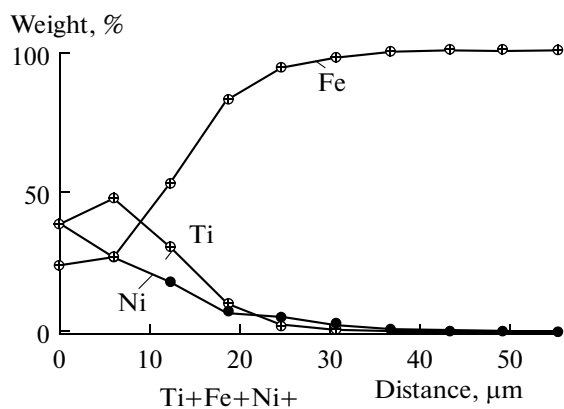**Fig. 17.** Microstructure of the transition zone (the base is steel 9KhSA).

Fig. 18. Concentration distribution of elements in the transition zone.

entirely absent; a small amount of titanium diffuses and alloys the material of the substrate.

—The composition of the substrate has an effect on the size of the transition and diffusion zones. It ranges from 17 μm for steel 9KhSÀ to 26 μm for steel 20; that is, the higher the degree of alloying, the less the depth of the modified layer.

—The CC is formed from carbides and a solid solution of nickel in iron and contains both large (4–5 μm) and small carbides (less than 1 μm); in addition, large grains of titanium carbide are formed in the central portion of the coating, and the grain size decreases to 100 nm while approaching the transition zone. Large grains of titanium carbide in the coating consist of dispersed carbides with sizes less than 1 μm.

REFERENCES

1. Sarantsev, V.V., A Technology for the Preparation of Composite Coatings via the Electrospark Machining of Lubricants of SHS Reagents, *Remont, Vosstanovlenie, Modernizatsiya*, 2007, no. 2, pp. 13–17.

2. Reut, O.P., Khina, B.B., Sarantsev, V.V., and Markova, L.V., The Use of Self-Propagating High-Temperature Synthesis and Electrospark Machining for the Deposition of Composite Coatings, *Uprochnyayushchie Tekhnol. Pokrytiya*, 2007, no. 1, pp. 49–56.

3. Podlesov, V.V., Stolin, A.M., and Merzhanov, A.G., SHS Extrusion of Electrode Materials and Their Application in Electric-Spark Alloying of Steel Surfaces, *J. Eng. Phys. Thermophys.*, 1993, no. 5, pp. 1156–1165.

4. Bazhin, P.M. and Stolin, A.M., Preparation of Electrodes for Electrospark Alloying via SHS–Extrusion: Properties and Prospects of Use, *Trudy GOSNITI*, 2010, vol. 106, pp. 125–127.

5. Safronov, I.I. et al., *Elektroerozionnye protsessy na elektrodakh i mikrostrukturno-fazovyi sostav legirovannogo sloya*, (Electroerosion Processes on Electrodes and the Microstructure–Phase Composition of the Alloyed Layer), Dorozhkin, N.N., Ed., Chisinau: Shtiintsa, 1999.

6. Novikov, N.P., Borovinskaya, I.P., and Merzhanov, A.G., A Thermodynamic Analysis of the Self-Propagating High-Temperature Synthesis, in *Protsessy goreniya v khimicheskoi tekhnologii i metallurgii* (Combustion Processes in Chemical Technology and Metallurgy), Chernogolovka: Otd. Inst. Khim. Fiz. Akad. Nauk SSSR, 1975, pp. 174–188.

7. Kiparisov, S.S. and Libenson, G.A., *Poroshkovaya metallurgiya: uchebnik dlya tekhnikumov* (Powder Metallurgy: a Handbook for Colleges), Moscow: Metallurgiya, 1991.

ELECTRICAL SURFACE
TREATMENT METHODS

Effect of Pressure on the Electric Properties
of Passivating Coatings Based on Lead Borosilicate Glasses

S. I. Vlasov and F. A. Saparov

National University of Uzbekistan, Vuzgorodok, Tashkent, 100174 Republic of Uzbekistan
e-mail: vlasov@uzsci.net
Received December 6, 2010

Abstract—The effect of pressure on the electric properties of dielectric $PbO-SiO_2-B_2O_3-Al_2O_3-Ta_2O_5$ coatings has been studied. The dependence of the parameters of the coatings on the value of the uniform compression has been found.

In this work, we describe the research results on the effect of uniform hydrostatic compression on the electric properties of dielectric coatings. The coating under study was lead borosilicate glass of the $PbO-SiO_2-B_2O_3-Al_2O_3-Ta_2O_5$ type (47% PbO, 34% SiO_2, 15% B_2O_3, 3% Al_2O_3, and 1% Ta_2O_5) deposited on the surface of silicon wafers (KEF-10 with the $\langle 111 \rangle$ crystallographic orientation) from a fine mixture with the subsequent fusion ($T = 680°C$) and annealing ($T = 470°C$) [1]. The thickness of the glass layer was 200–250 nm. The choice of the glass was caused by its extensive use for sealing high-current semiconductor devices. The main research method was the technique of isothermal relaxation of the high-frequency (1 mHz) capacitance of a metal–insulator–semiconductor (MIS) structure during an increase in the charge of the inversion layer [2]. The MIS structures were prepared via the vacuum deposition of aluminum on the surface of the glass. The diameter of the control electrodes was 3 mm. The resulting structures were subjected to uniform compression to pressures of 2–8 kbar (a step of 2 kbar with an exposure of 20 min in each interval) using a Gidrostat LG-16 setup.

Figure 1 depicts the experimental relaxation dependences of one of the structures under study; they were measured (in the dark at a temperature of 20°C) before (curve *1*) and after the impact of pressure (curves *2–6*) after the switching of the voltage from V_1 to V_2 ($V_1 = 8$, $V_2 = 18$ V). These dependences show that the impact of pressure with a value higher than 4 kbar leads to an increase in the time of the formation of the inversion layer charge. The analysis of the contribution of the surface and bulk generation currents to the total generation rate carried out via the methods described in [2, 3] showed that the value of the bulk generation currents hardly changes after the impact of the pressure. At the same time, the value of the surface components of the generation currents significantly decreases. Moreover, the control measurements of the

structures subjected to pressure, which were performed according to the technique [4, 5] based on Schottky diodes (the diodes were prepared after the chemical removal of the glass layer and the vacuum deposition of Au), showed the absence of generation–recombination centers with concentrations higher than 10^{11} cm^{-3}. Therefore, the above pressure modes do not change the parameters of the semiconductor substrate and have an effect on the glass layers adjacent to the interface with the semiconductor. An increase in the time of the formation of an inversion layer in the studied structures can be caused by the formation of an acceptor center in the glass layers adjacent to the interface with the semiconductor [6]. At fairly high inversion voltages, this center captures holes from the
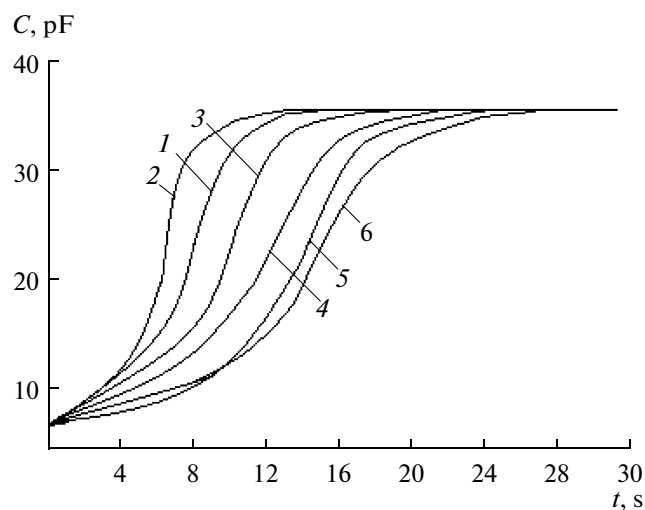

Fig. 1. Relaxation dependences of the structures under study measured (*1*) before and (*2–6*) after the impact of pressure, kbar: (*1*) 0, (*2*) 2, (*3*) 4, (*4*) 6, (*5*) 7, and (*6*) 8; $T = 20°C$.
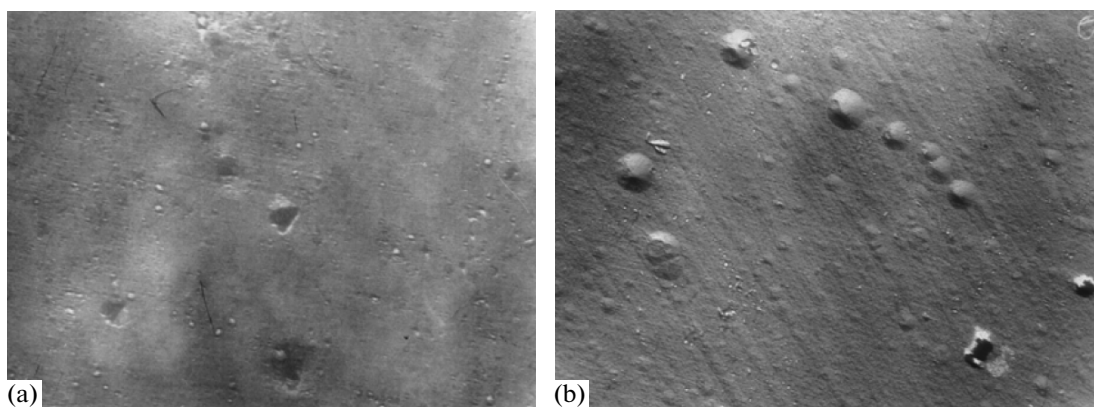
Fig. 2. Microphotographs of the structures under study measured (a) before and (b) after the impact of a pressure of 4 kbar.

increasing charge of the inversion layer and decreases the rate of its formation.

To verify this assumption, the aluminum layer that served a control electrode was chemically removed from some MIS structures and the surface layers of glass were removed in vapors of hydrofluoric acid. After that, the microphotography of the glass surface was performed. Figure 2 depicts the micrographs of the glass surfaces for two structures (before and after the impact of a pressure of 4 kbar). The comparison of these photographs shows that the structures subjected to the pressure contain additional inclusions, which can be responsible for the observed changes in the relaxation dependences.

REFERENCES

1. Parchinskii, P.B., Vlasov, S.I., and Turgunov, U.T., Properties of Passivating Coatings Based on Lead Borosilicate Glass, *Inorg. Mater.*, 2002, vol. 38, no. 6, pp. 621−624.

2. Zerbst, M., Relaxation Effekts on Holbeiter Isolator Grenzflochen, *Z. Angew. Phys.*, 1962, no. 30, pp. 22−29.

3. Abdurakhmanov, K.P., Berman, L.S., Vlasov, S.I, and Kotov, B.A.., A Study of Residual Deep Centers in Metal−Insulator−Semiconductor Structures via the Capacitance Method, *Fiz. Tekh. Poluprovodn.*, 1979, vol. 13, no. 7, pp. 1447−1450.

4. Berman, L.S., *Emkostnye metody issledovaniya parametrov poluprovodnikov* (Capacitance Methods for Studying the Parameters of Semiconductors), Leningrad: Nauka, 1981.

5. Berman, L.S. and Lebedev, A.A., *Emkostnaya spektroskopiya glubokikh tsentrov v poluprovodnikakh* (Deep-Level Capacitance Spectroscopy of Semiconductors), Leningrad: Nauka, 1982.

6. Vlasov, S.I., Nasirov, A.A., Mamatkarimov, O.O.., and Ergasheva, M.A., Nonmonotonous Capacitance−Voltage Characteristics in Metal−Glass−Semiconductor Structures, *Surf. Eng. Appl. Electrochem.*, 2008, vol. 44, no. 3, pp. 250−251.

ELECTRICAL PROCESSES
IN ENGINEERING AND CHEMISTRY

Condensation of a Gas–Vapor Mixture under the Conditions of a Corona Discharge

M. K. Bologa[a], F. P. Grosu[b], A. A. Polikarpov[a], and O. V. Motorin[a]

[a]*Institute of Applied Physics, Academy of Sciences of Moldova, ul. Akademiei 5, Chisinau, MD 2028 Republic of Moldova*
[b]*State Agrarian University, ul. Mirchesht' 44, Chisinau, MD 2049 Republic of Moldova*
e-mail: mbologa@phys.asm.md, f.grosu@mail.ru
Received December 12, 2010

Abstract—The experimental data on the condensation of vapor from a gas–vapor mixture in the presence of an electric field are discussed. It is assumed that a corona discharge or, to be more accurate, its accompanying phenomena such as the unipolar charging of the medium and the electric wind, which produces intense mixing both of the medium and the condensate film, is the main factor influencing the intensification of the condensation in an electric field. The criteria of the similarity of the process, among which the main attention is drawn to the "electric" Reynolds number, which characterizes the interaction of the electric field with the medium, are considered. We also discuss the parameters of vapor–air mixtures, such as their density, viscosity, and ion mobility. A simplified method of the generalization of the experimental data on condensation in the presence of an electric field based on the concepts of a corona discharge is proposed.

INTRODUCTION

The problems of the effect of electric fields on the condensation processes are presented in sufficient detail in works [1–3]. The emphasis is on the field's effect on the condensate film's interface and its deformation and destruction. A physical consideration of the phenomena is proposed based on the concept of ideal dielectrics (the force $f \sim E^2 \cdot \nabla\varepsilon$) [4] without allowance for the possible appearance of free electric charges in the medium ($\rho \neq 0$). Such an approach may be thought reasonable as high-ohmic liquid dielectrics of the Freon type and almost uniform fields are considered. However, there are no data on the influence of electric fields on the condensation of vapors of comparatively conducting liquids, for example, water, when its conducting properties and the possibility of the electric charging of the medium as a whole should be taken into account. This gap has been to some extent compensated for in work [5], in which the results of the experimental investigations of the influence of an electric field on the process of condensation of steam from a vapor–air mixture are presented.

The experiments were carried out using an experimental setup being a vapor condenser in the form of a vertical tube and a copper wire with notches in the form of rings in its varnish insulation being stretched along its axis with a mean distance of 5 mm between the notches. The notches were made intentionally to cause a corona discharge, as, in this case, the greatest effect of the field on the condensation should be

expected. A constant high voltage was supplied to the wire, and the tube served as a grounded electrode. Vapor and air were supplied from the tube's lower end and, mixing, they form a working medium from which the vapor was condensed. The tube condenser was cooled outside by an air flow from a fan.

The results have been processed in the form of the diagram relationships between the condensate mass ratio and the air mass concentration $G_E/G_0 = f_1(c)$ at different current intensities I and the current intensity at different velocities v of the external airflow— $G_E/G_0 = f_2(I)$. The third relationship $G_E/G_0 = f_3(v)$ has been established by the previous two ones. The tests show that, with the air concentration growing, the condensate mass ratio decreases, and the increase of the current intensity and the tube airflow velocity cause the enhancement of the condensation process. These results, which are quite reasonable from the physical point of view, are inconvenient from the point of view of engineering design. Thus, there is required the criteria generalization of them with that being the aim of this work.

PARTIAL DEPENDENCES

It is well known that the generalized dependences are searched for in the form of exponential functions of the generalized parameters called the similarity criteria [6]. The exponents of these dependences can be
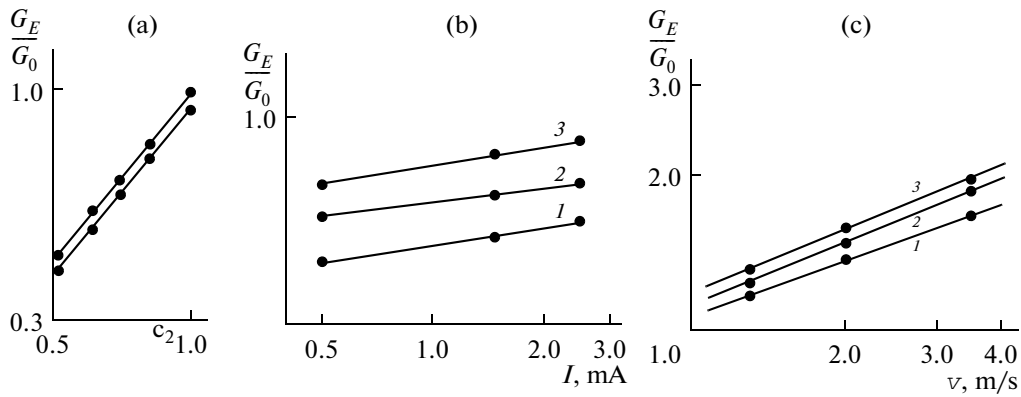
Fig. 1. The dependences $f_1(c_2)$, $f_2(I)$, and $f_3(v)$.

found by partial dependences within logarithmic coordinates:

$$\log \frac{G_E}{G_0} = \begin{cases} \log f_1(c_2); & f_1 \sim c_2^n; & I, v = \mathrm{const}; \\ \log f_2(I); & f_2 \sim I^m; & v, c_2 = \mathrm{const}; \quad (1) \\ \log f_3(v); & f_3 \sim v^p; & I, c_2 = \mathrm{const}. \end{cases}$$

As $f_1(c)$ is a decreasing function of the air concentration, it is expedient to pass to the increasing function $f_2(c_2)$ of the vapor concentration $c_2 = 1 - c$ being reflected in the first line of formulas (1). In view of this and by the data of work [5], in Fig. 1 there are presented dependences (1) constructed within the logarithmic net in which the rectification of the curves occurs. We find the exponents by the slope ratios of the constructed right lines (Fig. 1): $n = 1.14$; $m = 0.15$; $p = 0.42$.

SIMILARITY CRITERIA

To construct the generalized dependence, we need the similarity criteria corresponding to every independent variable of system (1). The vapor concentration c_2, being a dimensionless quantity, is a similarity criterion itself. The Reynolds number naturally will be the similarity criterion for the airflow velocity:

$$\mathrm{Re} = \frac{vd}{v_0}, \quad (2)$$

where v_0 is the kinematic viscosity of the air at room temperature. The natural convection around the tube also favors cooling the air, but this effect is small in comparison with the forced airflow, and it is taken into account by the condensate mass without naturally field.

The accounting for the electric field's effect on the condensation is the most complicated. At first, it is necessary to elucidate the physical essence of the field–medium interaction mechanism. In work [4], this interaction is considered from the point of view of ideal dielectrics, in particular, considering the vapor–

liquid interface's deformation by polarization forces. However, not disputing the significance of this effect, we think that the corona discharge [7] is more important with the following consequences of the unipolar charging of the medium and the phenomenon of the electric wind. Both these factors favor the turbulization of the vapor–air mixture and the enhancement of the processes of the heat and mass transfer. A forceful argument in support of this assumption is the experimental fact that the substantial influence of an electric field on these processes arises simultaneously with the discharge current in the high voltage circuit with this current being unequivocally of corona nature as it originates from the regions with very small dimensions ("scratches"). Thus, in order to characterize the effect of an electric field, we need a criterion allowing for the electric wind's intensity. Such a criterion was established previously [8] and is of the form of

$$\mathrm{Re}_E = \left(\frac{j \gamma l^3}{k \eta^2} \right)^q, \quad (3)$$

where j is the corona discharge current density, γ is the medium's (gas mixture) density, η is the coefficient of dynamic the viscosity, l is the characteristic dimension of the corona's region, and k is the coefficient of the ion mobility of the corona electrode's sign.

As is shown in [8], the exponent q is within the limits $1 > q > 0.5$, reducing from unity to 0.5 as the electric wind develops from a laminar mode to a turbulent one. Expression (3) later named the "electric" The reynolds number [9] is successfully employed to treat the experimental data on the heat transfer of a corona wire to different gases (air, carbon dioxide, argon, or helium) under different pressures (from 0.1 to 20 at). We also try to use this number to generalize the data on condensation under the conditions of a corona discharge as the physical essence of the interactions under examination is in many respects the same. Specifying the parameters included in formula (3), we should primarily note that the current density will depend, apart from the electric voltage, on the geo-
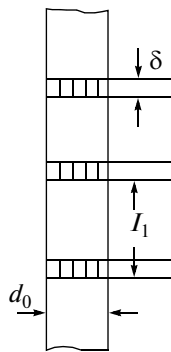
Fig. 2. The pattern of notches.

metric factors. A pattern of notches in the form of crosshatched rings is presented in Fig. 2.

As the corona discharge originates from them, it is clear that the notch width $l \equiv \delta$, which in the calculation is assumed to be about the blade edge width (10 μk), should serve as a characteristic dimension in formula (3). In this case, the electric current density will be determined by the chain of equalities

$$j = \frac{I_1}{S_1}; \quad I_1 = \frac{I}{N}; \quad S_1 = \pi d_0 \delta;$$
$$N = \frac{L}{l_1}; \Rightarrow j = \frac{Il_1}{\pi d_0 L \delta}. \tag{4}$$

By criterion (3), the air–vapor mixture is characterized by a thermodynamic parameter equal to the relation γ/η^2, which (as can be demonstrated in the context of the kinetic theory of an ideal gas) is a quantity depending on the pressure p, the temperature T, and the molecular dimensions. Genuinely, assuming the mixture to be an ideal gas, we will have for the density

$$\gamma = \frac{p}{RT} M, \tag{5}$$

where M is the molar mass of the mixture.

On the other hand, the ideal gas's viscosity is given by the formulas

$$\eta = \frac{1}{3}\gamma \bar{u} \lambda = \frac{1}{3} m_0 n \sqrt{\frac{3RT}{M}} \frac{1}{\sqrt{2}\pi d_*^2 n}$$
$$= \frac{1}{\pi d_*^2 N_A} \sqrt{\frac{RTM}{6}},$$

where d_* is the molecule's diameter, m_0 is its mass, and the other notations are conventional.

With allowance for these equalities, we obtain

$$\frac{\gamma}{\eta^2} = 6p \left(\frac{\pi d_*^2 N_A}{RT} \right)^2,$$

a parameter which at these p and T depends only on the dimensions of the molecules. For air and steam, the diameters of the molecules are nearly the same, so the fraction in the left member can be assumed constant and referred only to one component (air is more convenient).

Moreover, in actual practice, we deal with real gas mixtures for which the viscosity depends in a complicated way on the partial coefficients of the viscosity and other physical parameters [10]. Thus, it is desirable to employ more adequate quantities in the calculation using tables of the experimental data for mixtures. However, for the density, formula (5) is quite plausible, in which the molar mass is determined by a universally accepted expression:

$$M = \frac{m_1 + m_2}{(m_1/M_1) + (m_2/M_2)}, \tag{6}$$

where M_1 and M_2 are the molar masses, and the indices "1" and "2" correspond to the air and vapor, respectively. Considering the definitions of the concentrations $c_1 = m_1/m$; $c_2 = m_2/m$; $m = m_1 + m_2$, we obtain

$$\gamma = \frac{p}{RT} \frac{M_1}{1 + \gamma' c_2} = \frac{\gamma_1}{1 + \gamma' c_2}; \quad \gamma' = \frac{M_1}{M_2} - 1. \tag{7}$$

As might be expected, the mixture's density reduces as the vapor's density rises.

As mentioned above, the coefficients of the viscosity η [10] and the mobility k depend in a complicated way on the values of these coefficients for the separate components, so, in the first approximation, we will determine them as statistically average values:

$$\eta = c_1 \eta_1 + c_2 \eta_2 = \eta_1 (1 - \eta' c_2);$$
$$\eta' = 1 - (\eta_2/\eta_1);$$
$$k = c_1 k_1 + c_2 k_2 = k_1 (1 - k' c_2);$$
$$k' = 1 - (k_2/k_1). \tag{8}$$

These formulas are applicable only owing to the closeness of the sought-for coefficients η and k for the air and vapor. It follows from them that the presence of the air with its viscosity and mobility being larger than those of the vapor causes the growth of both coefficients leading to the degradation of the condensation process.

Substituting the last formula of (4) into (3), in terms of (7) and (8), we obtain

$$\mathrm{Re_E}$$
$$= \left(\frac{Il_1 \delta^2 \gamma_1}{\pi d_0 L k_1 \eta_1^2} \right)^q \left[\frac{1}{(1 + \gamma' c_2)(1 - k' c_2)(1 - \eta' c_2)^2} \right]^q. \tag{9}$$

GENERALIZED DEPENDENCE

Thus, there are three similarity criteria: c_2, Re_E, and Re. We search for the generalized dependence in a standard exponential form:

$$G_E/G_0 = ac_2^n Re_E^m Re^p. \qquad (10)$$

Substituting formula (9) into this expression, we find

$$\frac{G_E}{G_0}$$
$$= ac_2^m Re_{E1}^m \left[\frac{1}{(1+\gamma'c_2)(1-k'c_2)(1-\eta'c_2)^2} \right]^m Re^p, \qquad (11)$$

where there is separated out a criterion corresponding only to the air:

$$Re_{E1} \equiv \left[\frac{Il_1\delta^2\gamma_1}{\pi d_0 L\gamma_1\eta_1^2} \right]^q. \qquad (12)$$

As the expression in the square brackets of (11) for this composition of the mixture is a function of only the vapor concentration c_2, in the initial simplified version of the experimental data's generalization, we will combine this function with the multiplier c_2 and, in this very form, we will search for the final dependence on c_2. Then, in (10), there remains the dependence on (12) instead of the dependence on (9); we use for simplicity the notation m for the exponent mq; and the sought-for criteria's dependence becomes

$$\frac{G_E}{G_0} = ac_2^n Re_{E1}^m Re^p$$
$$= ac_2^n \left(\frac{Il_1\delta^2\gamma_1}{\pi d_0 Lk_1\eta_1^2} \right)^m \left(\frac{vd}{v_0} \right)^p, \qquad (13)$$

where the constant a should be found on the basis of the experimental data. As $Re_E \sim I$, $Re \sim v$, m and p we consider found (see above). Then, for equation (13), we find

$$G_E/G_0 = ac_2^{1.14} Re_{E1}^{0.15} Re^{0.42}. \qquad (14)$$

The coefficient a can be found as the arithmetic mean value of the expression

$$a = (G_E/G_0)(c_2^{1.14} Re_{E1}^{0.15} Re^{0.42})^{-1}. \qquad (15)$$

The processing of the experimental data gives the value of $a \approx 0.018$ and the final generalized dependence:

$$G_E/G_0 \approx 0.018 c_2^{1.14} Re_{E1}^{0.15} Re^{0.42}. \qquad (16)$$

It should be noted that the small value of the exponent of the "electric" Reynolds number points to the intensive mixing of the medium by an external electric field, as the exponent of this criterion contains one more indicator ($q \to 0.5$) reducing as the electroconvection develops.

This work should be considered as one of the first attempts to process experimental data on condensation from the point of view of corona discharge concepts. The parameters of the medium in the course of the condensation process in the presence of a field should be refined. The results allow one to reach a common conclusion concerning the validity of these concepts.

REFERENCES

1. Bologa, M.K., Smirnov, G.F., Didkovskii, A.B., and Klimov, S.M., *Teploobmen pri kipenii i kondensatsii v elektricheskom pole* (Heat Transfer at Boiling and Condensation in Electric Field), Kishinev: Shtiintsa, 1987.

2. Gidwani, A., Molki, M., Ohadi, M., EHD-Enhanced Condensation of Alternative Refrigerants in Smooth and Corrugated Tubes, *HVAC&R Res.*, 2002, vol. 8, no. 3, pp. 219–237.

3. Shigefumi Nishio and Ichiro Tanasawa, Enhancement of Condensation Heat Transfer on a Finned Tube Using an Electric Field Ren Cai, C. Chu, *J. Enh. Heat Trans.*, 2001, vol. 8, no. 4, pp. 215–229.

4. Bologa, M.K., Korovkin, V.P., and Savin, I.K., *Dvukhfaznye sistemy zhidkost'-par v elektricheskom pole* (Liquid-Vapor Two-Phase Systems in Electric Field), Kishinev: Shtiintsa, 1992.

5. Bologa, M.K., Grosu, F.P., Polikarpov, A.A., and Motorin, O.V., Condensation of a Gas-Vapor Mixture in an Electric Field, *Surf. Eng. Appl. Electrochem.*, 2009, vol. 45, no. 2, pp. 125–127.

6. Kaptsov, N.A., *Elektricheskie yavleniya v gazakh i vakuume* (Electric Phenomena in Gases and Vacuum), Moscow: Gostekhizdat, 1950.

8. Bologa, M.K., Grosu, F.P., and Kozhuhar', I.A., *Elektrokonvektsiya i teploobmen* (Electroconvection and Heat Transfer), Kishinev: Shtiintsa, 1977.

9. Grosu, F.P. and Bologa, M.K., Electroisothermal Convection and its Role in the Process of Heat Exchange, *Surf. Eng. Appl. Electrochem.*, 2008, vol. 44, no. 3, pp. 187–194.

10. Golubev, I.F., *Vyazkost' gazov i gazovykh smesei* (Viscosity of Gases and Gas Mixtures), Moscow: Fizmatgiz, 1959.

ELECTRICAL PROCESSES
IN ENGINEERING AND CHEMISTRY

Electrodischarge Method for Synthesizing Nanocarbon from Gaseous Raw Hydrocarbons

L. Z. Boguslavskii[a], N. S. Nazarova[a], D. V. Vinnichenko[a], A. D. Rud'[b], and I. V. Urubkov[b]

[a]*Institute of Pulse Processes and Technologies, National Academy of Sciences of Ukraine,*
pr. Oktyabrskii 43a, Nikolaev, 54018 Ukraine

[b]*Institute of Metal Physics, National Academy of Sciences of Ukraine, pr. Vernadskogo 36, Kiev, 03142 Ukraine*

e-mail: boguslavsky@mail.ru

Received July 5, 2010

Abstract—A new method for electrodischarge synthesizing nanocarbon has been elaborated, which provides high gradients of temperatures and pressure at the expense of a high rate of energy input into the plasma channels. The morphological structure of the produced nanocarbon is uniform, the characteristic dimensions of the particles are in the range from 9 to 50 nm, and the content of chemically pure carbon amounts up to 97% (with the balance being O_2), so it is possible to avoid the labor-consuming operation of clearing nanocarbon when producing it through the electrodischarge method.

INTRODUCTION

The search for new efficient methods for synthesizing nanocarbon materials of different allotropic forms and sizes at plasma chemical synthesis remains up till now a topical problem as the majority of the known methods [1] have some shortcomings in their quality, productivity, and economic indices. For example, the well-known method of producing nanocarbon from gaseous raw hydrocarbons through pyrolysis demands substantial expenditures of energy.

The main line of investigation and elaboration of new methods for producing nanocarbon structures is obviously connected with the search for synthesis conditions peculiar to the construction of strictly specified allotropic forms of nanocarbon. As some authors suppose, for instance [2], not only high temperatures necessary for the destruction of the initial carbon materials but also high gradients of the temperature and pressure on the way from the evaporation of carbon up to the condensation of its molecules should be assigned to the main factors determining the formation of the spatial carbon structures. For example, the growth of the fullerene yield greatly depends on the process techniques [3] to increase this gradient, among them are the gas expansion and reduction of the path of fullerene with a mandatory and considerable drop of the substrate temperature to condensate it.

High temperature and pressure gradients can be achieved in the case of the explosive methods of generation of energy. High rates of energy input into the reaction volume to destroy the carbonaceous raw materials are provided by electrodischarge methods. The methods of electroexplosive decomposition of hydrocarbonic liquids and the electroexplosion of graphite conductors proposed previously in the IPPT of the National Academy of Sciences of Ukraine [4–6] have, alongside with the main advantages connected with the rapid production of the largest macroquantities of nanocarbon in comparison with other approaches, a principal shortcoming—laborious operations in order to dry and clean the obtained product and to separate it by its qualitative and fractional composition.

Though the arc method used to produce different allotropic forms of carbon is conventional, new results have been obtained in [7, 8] under other conditions of the reaction. Thus, in [7], there are described the investigations in order to produce nanocarbon with the help of high frequency arcs (with a frequency of more than 10 kHz) within the flow of carbon—helium plasma generated from the carbonic condensate of the evaporating graphite electrodes. It is shown that the production of carbonic nanotubes (CNT) and other modifications of nanocarbon within high frequency arcs with a nickel catalyst is the most efficient method of synthesis (the CNT yield under certain modes is up to 72%).

In [8], there is shown the treatment of ethanol aerosol in the secondary discharge plasma brought into some region separated from the electrodes (plasma is moved away from the electrodes, d.c. arc). A wide variety of nanocarbons have been obtained using the source parameters and external conditions (the pressure, the temperature, and the contents of the cushion gas and catalyst).
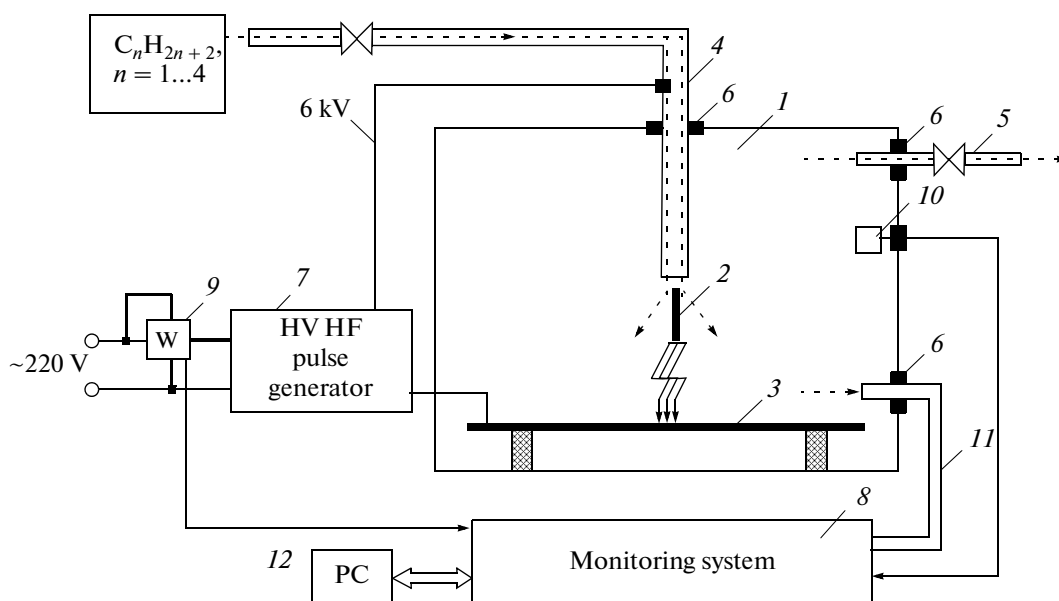
Fig. 1. Block diagram of the experimental setup for the electrodischarge synthesis of nanocarbon materials from gaseous carbonaceous raw material.

The aim of this work is to elaborate an electrodischarge method for synthesizing nanocarbon with a direct electrodischarge effect on gaseous hydrocarbons by high voltage pulse discharges with a recurrence frequency within the kilohertz range. It is shown by the example of treatment of propane and butanol that high gradients of temperature and pressure, as the necessary conditions for nanocarbon synthesis, are provided at the expense of a large rate of energy input into plasma channels. Nonequilibrium plasma (generated by discharges with a kilohertz recurrence frequency) allows involving sufficiently large volumes of gas into the process of the synthesis; thus, it is possible to consider it as a three-dimensional effect on a gaseous medium.

EXPERIMENTAL SETUP
FOR THE ELECTRODISCHARGE SYNTHESYS
OF NANOCARBON MATERIALS

A block diagram of the experimental setup for the electrodischarge synthesis of nanocarbon materials from gaseous carbonaceous raw material is shown in Fig. 1.

The diagram contains the following blocks:

—reactor (*1*) for the electrodischarge synthesis, in which the moving (*2*) and fixed (*3*) electrodes are arranged;

—channels to supply the initial raw material (*4*) and to remove the gaseous reaction products (*5*) mounted in the tank with the help of sealed leads (*6*);

—a high voltage and high frequency impulse generator (*7*) to strike discharges that are the source of nonequilibrium plasma;

—a system to monitor (*8*) the dynamic characteristics of the chemical reaction in reactor (*1*) (the pressure and temperature in the reactor and the energy consumed by the setup);

—a meter of the electric energy (*9*);

—the temperature gage in the reactor (*10*);

—a channel to measure the pressure (*11*) mounted in the tank with the help of a sealed lead (*6*);

—a personal computer (PC) (*12*).

A high voltage high frequency impulse generator with adjustable output voltage in the range from 3 to 10 kV and a frequency up to 40 kHz has been developed for the experimental setup for the electrodischarge synthesis of nanocarbon. The generator's block diagram is presented in Fig. 2.

A general view of the experimental setup is depicted in Fig. 3 with the following elements: *1*—the reactor model; *2*—wires to supply power to the upper moving (point or many-point) electrode and to the lower fixed (plane, point, or many-point) one; *3*—a balloon with gaseous raw material to carry out the reaction; *4*—a channel to supply raw material to the reactor; *5*—a channel to remove the reaction products; *6*—a high voltage high frequency generator; *7*—a system to monitor the dynamic characteristics of the chemical reaction (3.1) in reactor (1) (the pressure and temperature in the reactor, the power consumed by the setup); *8*—an electric power meter; *9*—the
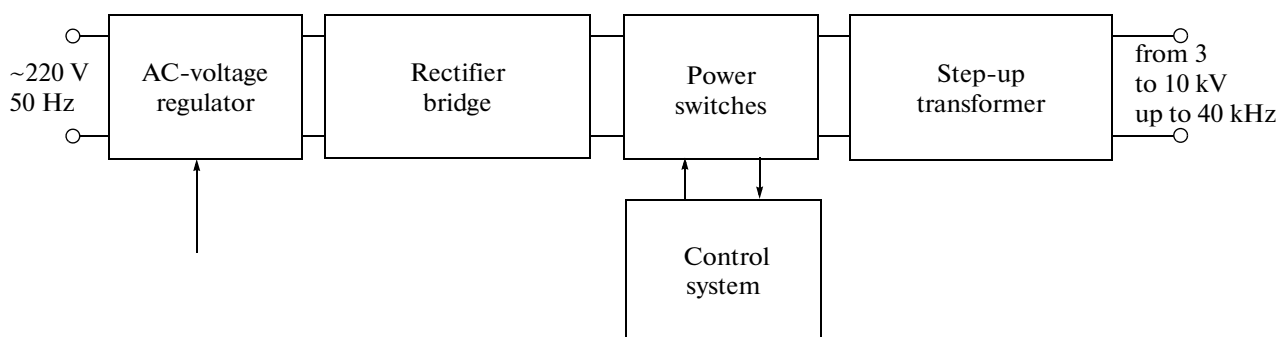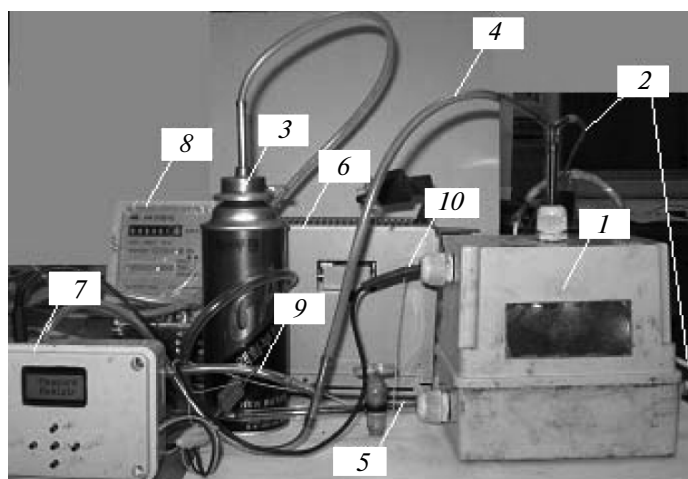
Fig. 2. Block diagram of the generator.

Fig. 3. Experimental setup for the electrodischarge synthesis of nanocarbon materials.

channel to measure the pressure; *10*—the channel for the signal's transmission from the temperature gage.

EXPERIMENS ON THE ELECTRODISCHARGE SYNTHESIS OF NANOCARBON FROM GASEOUS RAW HYDROCARBONS

The elaborated experimental setup makes possible the visual checking and automatic recording of the temperature and pressure of the mixture of raw material and reaction products in the reactor.

After the monitoring system and the reactor are switched on, the reactor is filled with gaseous raw material ensuring the residual air concentration is not more than 1 percent. Then, the recording regime within the monitoring system and the power supply are switched on. The control system allows carrying out the synthesis of nanocarbon according to the pre-scribed algorithm.

After the generator's power supply is switched on, the recorded data are written down into text files and then the monitoring system is switched off. Nanocarbon is gathered some time after the setup is switched off in order that the synthesis products sediment. The produced nanocarbon is put into insulated vessels to be preserved and analyzed.

The experiments were carried out with the recurrence frequency of the output voltage impulses in the range from 1 to 40 kHz. The electrodischarge synthesis was conducted in a medium of butane and isobutane for different configurations of the electrode systems under atmospheric pressure and slightly increased pressure and the temperature in the reactor up to 60°C. The gas mass under atmospheric pressure and the mentioned temperatures is a heat carrier sufficient to cool and condensate the carbon vapors. The gas density and high rate of power input provide a great temperature gradient within the region of synthesis.

Visual observations show that the reaction products condense in a gaseous medium over a distance of one or more centimeters from the plasma channel.
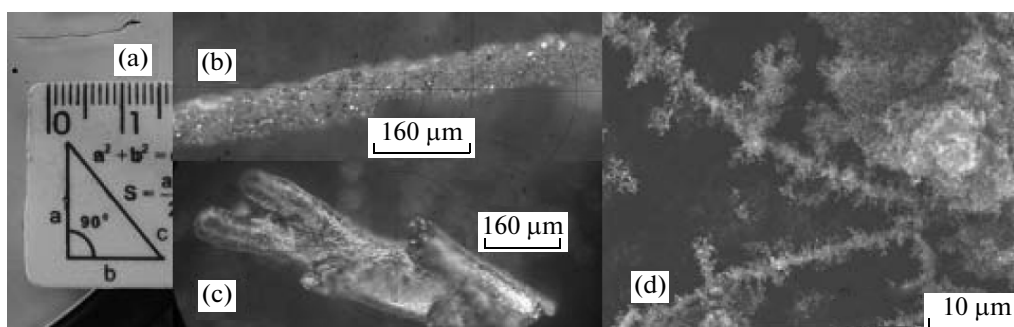
Fig. 4. Macroscopic types of synthesized nanocarbon in the form of nanocarbon "trees" with diameters from 80 to 160 μm and lengths up to 20 mm (a, b, c) and weblike carbon (d).

The electrodes were made of copper, tinned copper, iron, nickel, titanium, silver, and platinum.

EXAMINATION OF THE PRODUCED NANOMATERIALS

As a result of the carried out experiments, there were produced under almost all the considered conditions materials whose macroscopic properties included a small bulk weight (13.4 kg/m^3) and a surface in the form of "poplar wool" under 1000× magnification (which indicates their nano- and microdimensions).

The developed method is distinguished for the extremely easy gathering of the synthesis products: one should simply pour the produced nanomaterial out into a vessel to store it. In this case, there is no need to clean the synthesis products from noncarbonic impurities. The morphological composition of the electrodischarge synthesis products is almost uniform (up to 90%) under the prescribed electric parameters of the treatment.

As a result of the electrodischarge synthesis, there are produced materials of two types with two macroscopic structures: thin firm needles (or "trees") (Fig. 4a at full scale; b, c with magnification) and weblike carbon (Fig. 4d). As the further investigation with the help of an electron microscope shows, the composition of both structure types is the same. Both types of compositions consist of nanoparticles with the same (within the limits of the statistical distribution) forms and dimensions. The formation of the nanomaterials of the "tree" type can be explained by the clinkering of the weblike carbon in the area close to the arc. The compositions shown in the figures are like large molecules of fullerenes and short nanotubes that stopped growing. The characteristic dimensions of the synthesized nanoparticles (Fig. 5) are in the range from 9 to 50 nm.

The web composition also includes microtubes (Fig. 6a), microdiamonds (Fig. 6b), and multilayer nanofilms (Fig. 6c). Some of the produced powdered materials exhibit magnetic properties.

Of special interest is the synthesis of carbon nanotubes from a gaseous medium. There is obtained a large variety of materials outwardly resembling multilayer nanotubes. Images of such objects at different magnifications are presented in Fig. 7.

There are also some objects being nanotubes packed into bands presented with different magnification in Fig. 8. As it is shown in [1], such objects can appear when nanotubes are compacted.

The study of the structure and dimensions of the nanomaterials presented in Figs. 4b, 4c, 6a, and 6b were carried out with the help of a microscope (Niophot-555).

The study of the structure and dimensions of the nanomaterials presented in Figs. 8 and 9 were carried out with the help of a scanning electron microscope (JSM-6490LV).

The other microphotos were obtained with the help of a transmission electron microscope (JSM-6700F).
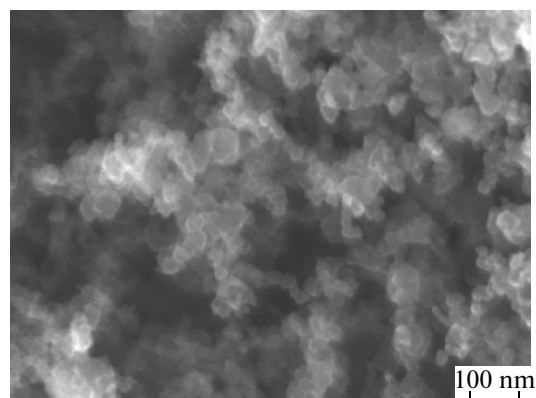
Fig. 5. Nanostructures of the synthesized carbon materials.
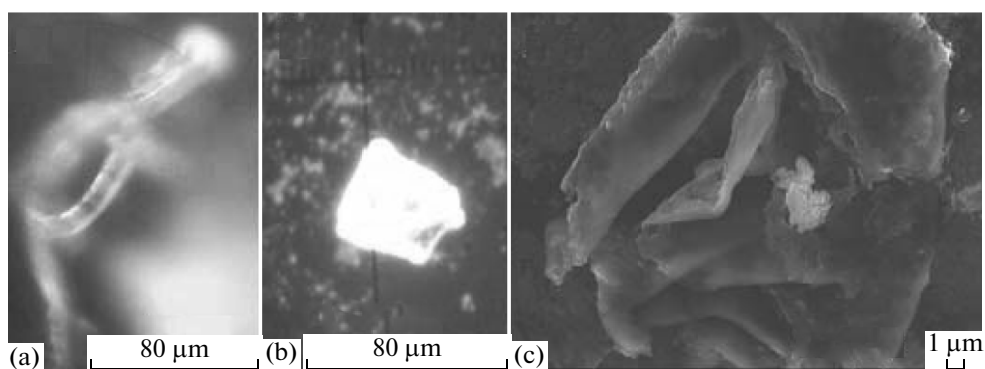
Fig. 6. Microtubes (a), microdiamonds (b), and multilayer nanofilms (c) produced through electrodischarge synthesis in a gaseous medium.
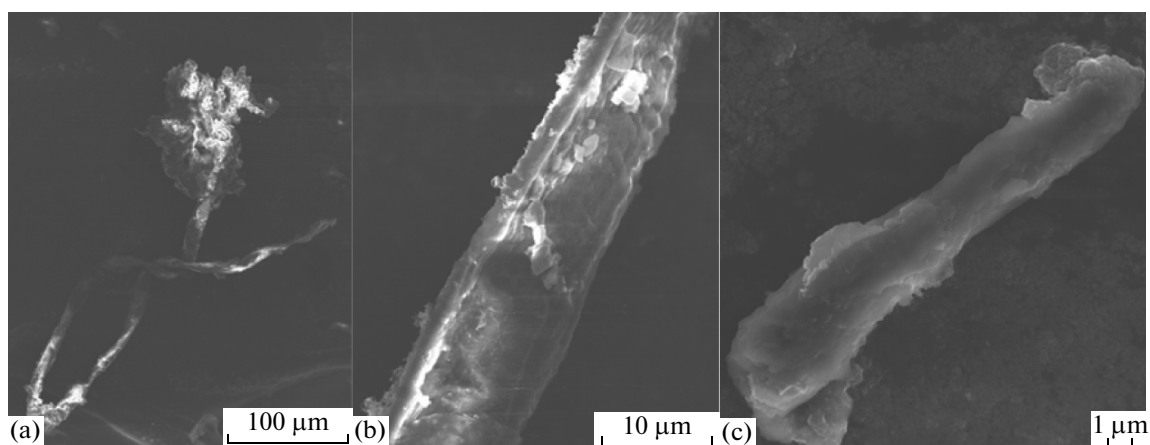
Fig. 7. Multilayer nanotubes.

INVESTIGATION OF THE MICROSTRUCTURE OF THE SYNTHESIZED NANOCARBON MATERIALS

The investigation of the microstructure was carried out with the help of a scanning electron microscope (JSM-6490LV) produced by the JEOL Ltd. Company (Japan) equipped with an energy dispersive spectrometer (EDS) (INCA Energy 350 Premium) with a silicone drift detector, a spectrometer with wavelength dispersion (INCA Wave 500), and a diffraction detec-
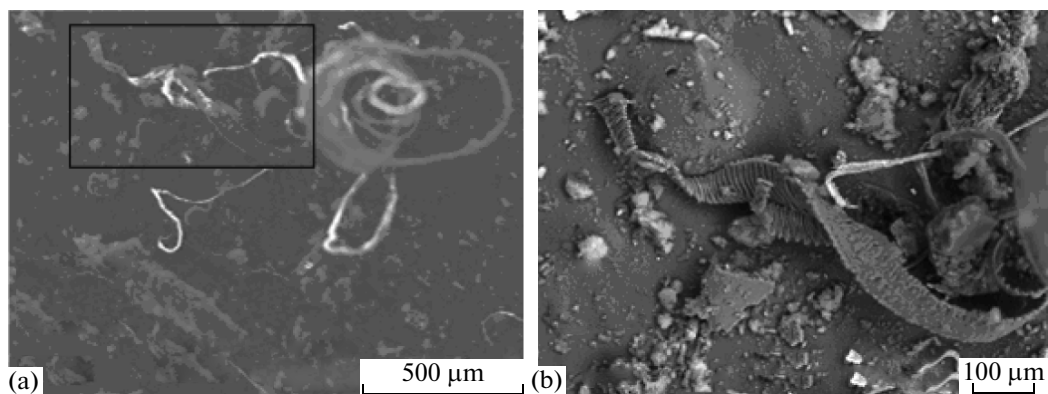
Fig. 8. Conglomerate of nanotubes (a); a magnified fragment (b) where some nanotubes are seen packed into a band.

tor of retroreflected electrons (HKL Channel 5 EBSD) produced by OXFORD Instruments Analytical LTD (Great Britain). The investigations were carried out with an accelerating voltage of 20 kV and a beam current of about 5 nA, the working distance was 10 mm, and the size of the focal spot was 60 arbitrary units. These operational factors ensured a sufficient resolution capability and a high-quality signal of the EDS. The image in the mode of secondary electrons was recorded to study the morphology of the specimens. The uniformity of the specimens in elemental composition was estimated in the mode of recording the reflected electrons. The regions rich in light elements correspond to the darker plots in these photos and the heavy ones to the pale plots. Then, the examination of the elemental composition of some rectangular plots or separate points of one or another phase was performed using EDS. The calculation of the element concentrations by the obtained spectra was conducted through the matrix correction method (the so-called XPP method recently elaborated by OXFORD Instruments Analytical Ltd.).

The investigation of the produced material's microstructure has shown the presence of a negligible amount of water, aluminum, and silicone and some more percentage of titanium in the specimens presented in Figs. 8 and 9, being nanotubes packed into bands. The catalytic effect of titanium is believed to be the reason for the form of nanotubes.

The examination of the produced material's microstructure demonstrated the presence of a negli-
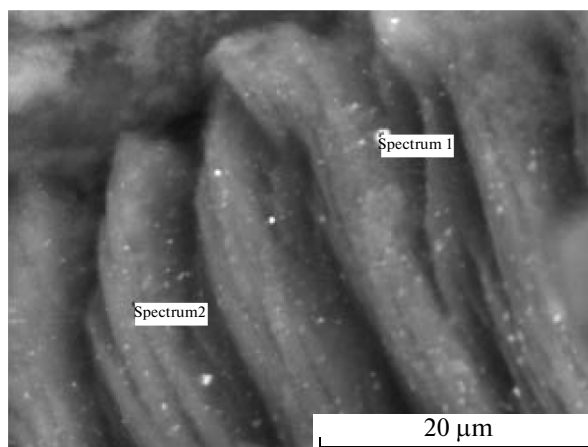
Fig. 9. Nanotubes packed into a band (a fragment of Fig. 8 with larger magnification).

gible amount of water (Table 2) in the specimens depicted in Fig. 4 being weblike carbon. In this case, the total content of chemically pure carbon runs up to 97%, thus confirming the possibility to avoid the laborious operation of cleaning nanocarbon.

The survey on the diffractometer (DRON-3) in Mo K_α radiation was performed to calculate the structure factor and the functions of the radial distribution of the atoms (FRDA). A diffractogram of the synthesis products obtained through the electrodischarge method is presented in Fig. 10, where there is seen a wide asymmetric peak in the range of $2\theta = 5°-13°$. Such a diffraction pattern is typical for amorphous

Table 1. Spectral distribution of the nanomaterial for the specimen presented in Fig. 9

Spectrum	C	O	Al	Si	Ti	Total
Spectrum 1	81.37	10.06	0.07	0.17	8.33	100.00
Spectrum 2	95.49	4.10			0.41	100.00
Max.	95.49	10.06	0.07	0.17	8.33	–
Min.	81.37	4.10	0.07	0.17	0.41	–

Table 2. Spectral distribution of the nanomaterial for the specimen presented in Fig. 4

Spectrum	C	O	Total
Spectrum 1	95.66	4.34	100.00
Spectrum 2	97.09	2.91	100.00
Spectrum 3	93.74	6.26	100.00
Spectrum 4	97.14	2.86	100.00
Average	95.90	4.10	100.00
Standard deviation	1.60	1.60	–
Max.	97.14	6.26	–
Min.	93.74	2.86	–
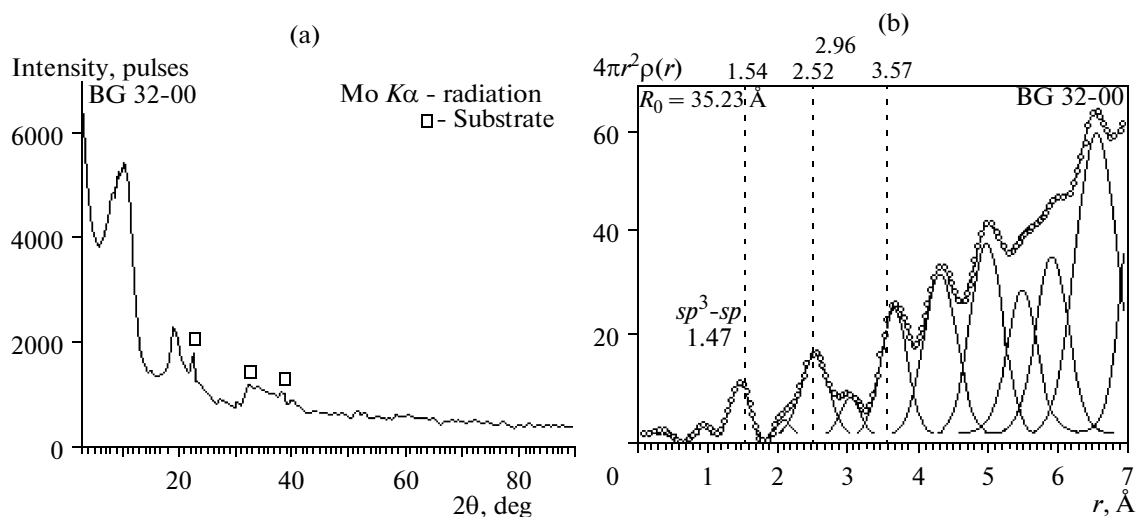
Fig. 10. Diffractogram (a) and FRDA (b) of the products of the electrodischarge synthesis of carbon.

structures. In order to accurately restore the type of the close-range order, there was calculated the FRDA of the blocks with dimensions of about 30 Å, and one can conclude that the specimens have a diamond-like type of close-range order.

CONCLUSIONS

There has been elaborated a new method for electrodischarge synthesizing nanocarbon providing high gradients of the temperatures and pressures at the expense of a large rate of energy input into the plasma channels. The composition of the synthesis products obtained through the developed method is almost uniform; up to 90% of the particles have the same form and their dimensions are in the range from 9 to 50 nm. The FRRA method demonstrates that the specimens have a diamond-like type of close-range order. The high content of chemically pure carbon (up to 97%, the balance being O_2) confirms the possibility to avoid the laborious operation of cleaning carbon when it is produced through the electrodischarge method.

ACKNOWLEDGMENTS

We express our thanks to the Tokio Boeki firm for the kindly furnished equipment needed to carry out our research work.

REFERENCES

1. Tkachyov, A.G. and Zolotukhin, I.V., *Apparatura i metody sinteza tverdotel'nykh nanostruktur*, (Apparatus and Methods for Synthesizing Solid Nanostructures), Moscow: Mashinostroenie, 2007.

2. Kharlamov, A.I., Kirillova, N.V., Zaitseva, Z.A., et al., New State of Carbon: Transparent Filamentous Anisotropic Crystals, *Dokl. Nats. Akad. Nauk Ukr.*, 2007, no. 5, pp. 148–154.

3. Trefilov, V.I. and Shchur, D.V., *Fullereny—osnova materialov budushchego* (Fullerenes as the Basis of Future Materials), Kiev: ADEF, 2001, p. 148.

4. Boguslavskii, L.Z., Kuskova, N.I., Dyupin, V.O., Petrichenko, V.M., and Khainatskii, S.O., Ukraine Patent 45181, *Byull. Izobret.*, 2004, no. 7, p. 3.

5. Kuskova, N.I., Boguslavskii, L.Z., Rud', A.D., et al., Electroexplosive Methods for Synthesizing Carbon Nanomaterials, *Metallofiz. Nov. Tech.*, 2008, vol. 30, no. 6, pp. 833–847.

6. Baklar, V.Yu, Zubenko, O.O., Boguslavskii, L.Z., Smal'ko, A.O., and Kuskova, N.I., Ukraine Patent 43714, *Byull. Izobret.*, 2004, no. 16, p. 4.

7. Osipova, I.V., Vnukova, N.G, Glushchenko, G.A., et al., Nickel-Bearing Carbon Nanotubes and Nanoparticles Produced in High Voltage Arc Plasma, *Fiz. Tverd. Tela*, 2009, vol. 51, no. 9, pp. 1857–1859.

8. Veremii, Yu.P., Chernyak, V.Ya., and Filatov, S.A., Production of Carbon Nanomaterials in Secondary Discharge Plasma, *Ukr. Fiz. Zh.*, 2008, vol. 53, no. 4, pp. 395–399.

ELECTRICAL PROCESSES
IN ENGINEERING AND CHEMISTRY

Electrokinetic Effects under the Action of Ultrasound in Liquid Media

V. L. Lanin

State University of Informatics and Radioelectronics of Belarus, ul. P. Brovki 6, Minsk, 220013 Republic of Belarus
e-mail: vlanin@bsuir.by
Received December 14, 2010

Abstract—The electrokinetic phenomena under the influence of ultrasound (US) on aqueous solutions and melts of fusible metals are experimentally investigated. It is established that the combined action of the ultrasonic and electric fields on the liquid media intensifies the processes of diffusion and dissolution of substances. This allows one to accelerate the processes of ultrasonic clearing in media of polar liquids and to raise the durability of the soldered connections.

INTRODUCTION

The action of powerful ultrasound (US) induces well-known effects in liquid media: the acoustic cavitation [1] associated with pulsations and the collapse of cavitation bubbles, the ultrasonic capillary effect [2], the sonoluminescence [3], the vortex effects as micro- and macrostreams [4], the enhancement of diffusion processes [5], etc. When the intensity of the ultrasound exceeds 10^5 W/m^2, the kinetic energy of the collapsing bubbles concentrated in a negligibly small volume transforms partly into force pulses and partly into heat energy. In liquid media under the action of ultrasonic vibrations, electric phenomena are also induced in the form of short pulses due to the negative electric charges of cavitation bubbles [3] and due to the electrokinetic phenomena related to the directed motion of the charged particles.

The elecrokinetic phenomena are observed in disperse systems and capillaries. They manifest themselves in the form of the relative motion of one phase with respect to another phase under the action of an external electric field (electroosmosis, electrophoresis) or as the appearance of a potential difference in the direction of the relative motion of the phases owing to the mechanic forces (the Dorn effect, the flow potential).

The electrokinetic phenomena in liquid media appear also owing to the increasing of the mobility of the charge carriers and the appearance of their directed mass transfer directed from the radiator under the action of the pressure of the ultrasonic wave. When cavitation bubbles collapse, the formation of additional carries—negatively charged cavitation bubbles—also taking part in the mass transfer is possible.

EXPERIMENTAL

Longitudinal ultrasound oscillations were excited using an immersed piston radiator with the aim to detect and investigate the electrokinetic phenomena of the second type. Ultrasonic oscillations with a frequency of 22–44 kHz were supplied to a piezoelectric transducer consisting of two piezoceramic rings with their diameter being 30 mm and two frequency lowering cover plates connected with thread studs. The amplitude was registered using a sensor located near the oscillating waveguide surface and connected to a vibrometer. The value of the electric current induced in the liquid owing to the directed motion of ions under the action of the ultrasonic field was registered using an F116/1 microammeter connected between the radiator and the stainless steel electrode located at the bottom of the bath with the liquid investigated (Fig. 1).

We also inserted a third gridlike electrode near the radiator to which a constant voltage of 400–500 mV was applied from an external source with the aim to check the hypothesis related to the influence of the polarity of the ions involved in the current formation.

A schematic view of the experiment on the combined action of ultrasonic and electric fields on liquid media at the treatment of metallic (*a*) and nonmetallic (*b*) materials is shown in Fig. 2. Sample (1) was immersed in the liquid at the distance *h* from the bottom of bath (2) and it was connected with a wire to one of the poles of external power source (3). The second pole of the source was connected with the bath. When electric oscillations were supplied from the US generator to transducer (4), mechanical oscillations were induced in it and transferred to the bath via diaphragm radiator (5). Under the action of the direct electric current, the hydrogen ions move in the direction from the radiator to the sample; the reduction of the ions
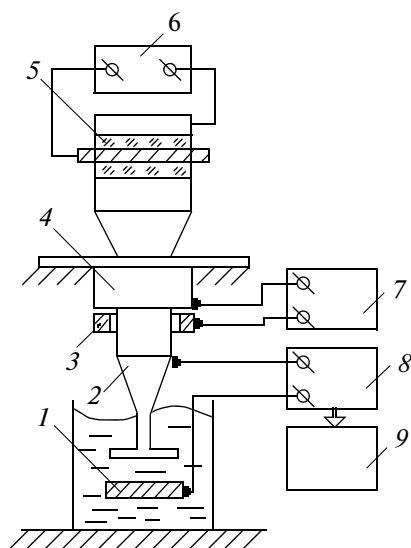
Fig. 1. Scheme of the experiment for the investigation of the electrokinetic effect in liquid media. (*1*) Electrode, (*2*) radiator, (*3*) amplitude sensor, (*4*) waveguide, (*5*) transducer, (*6*) US generator, (*7*) vibrometer, (*8*) current-sensing device, (*9*) automatic recorder.

and the formation of gas nuclei occur in the liquid, which facilitates the cavitation process.

At the local introduction of the US oscillations in the bath, the sample (1) was located in the bath (2) at a distance *h* from the working end of the radiator. The nonmetallic bath (2) has a hole in its bottom where a concentrator type radiator is fixed using gasket (6). The contact ring (7) was connected to one of the poles of external source (3), and the other pole was connected to radiator (5). The mechanical oscillations induced in transducer (4) were amplified by the con-

centrator and transmitted to the liquid medium. This increased the intensity of the cavitation phenomena owing to the deposition of cavitation nuclei on the treated sample and the local introduction of US oscillations.

During the investigations of the electrokinetic phenomena of the first kind, owing to the combined action of the energy of the US and electric fields on the melts and the durability of the formed metal connections, the value of the direct current through the melt changed in the range of 0–15 A. It was registered using an M2020 device connected in an electric circuit with a shunt with an accuracy of 0.5 mA. The US oscillations were supplied to the melt over 20–30 s after the current was switched on with the aim to eliminate the measurement errors owing to the heating of the wires and ballast resistor.

EXPERIMENTAL RESULTS AND DISCUSSION

The analysis of the data (see the table) shows that the most pronounced manifestation of the electrokinetic phenomenon of the second type (as the appearance of the potential difference and the increasing of the direct current value) was observed in the liquids with the least resistance and viscosity [6]. The time needed for the current to reach the equilibrium in a liquid is proportional to the liquid's viscosity. The maximal effect of the current increasing was registered for the interelectrode distance of 5 mm, since, in this case, the entire interelectrode zone is occupied with the cavitation bubbles. For less interelectrode distances, the current carries are partly pushed out from the zone owing to microstreams. When the distances exceed 5 mm, the electrokinetic effect in the liquids
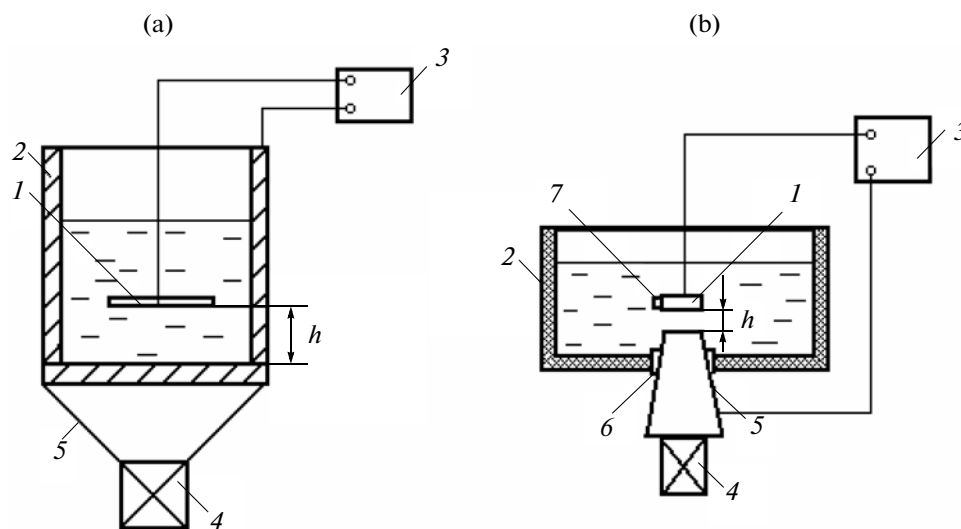

Fig. 2. Scheme of the experiment for the investigation of the combined activation by the energy of US and electric fields.

Characteristics of the electrokinetic effect in liquid media

Liquid medium	Resistance of the medium, Ω m	Viscosity, Pa s	Current variation ΔI, mA	Time needed to reach equilibrium, s
Mineral oil	10^{13}	3.2–3.3	0	–
Glycerin	10^{12}	1.5–1.6	0.06	70
Distilled water	10^{4}	0.32–0.33	0.6	50
Tap water	10^{2}	0.32–0.33	1.0	10
Ethanol	10^{4}	0.24–0.25	1.4	10
Organic acid	10	0.25–0.26	2.0	5
Water with Cl ions	0.3	0.32–0.33	3.4	3

becomes weaker, since the cavitation region does not occupy all the interelectrode zone.

The greatest potential increasing and the increasing of the direct current owing to this were observed in the liquids with the least electric resistance and viscosity. The time needed for the current to reach the equilibrium in a liquid is proportional to the liquid's viscosity (Fig. 3).

The maximal current increasing was registered for the interelectrode distance of 5 mm, since, in this case, the entire interelectrode zone is occupied with cavitation bubbles. For less interelectrode distances, the current carries are partly pushed out from the zone owing to microstreams. When the distances exceed 7 mm, the electrokinetic effect in liquids becomes weaker owing to the absorption of the US energy and the mass transfer weakening.

The appearance of the potential difference and the increasing of the current through the liquid can be explained owing to the fact that the US vibrations increase the mobility of the charge carriers in the liquid; a mass transfer appears directed from the radiator. When the cavitation bubbles collapse, additional carries, negatively charged cavitation bubbles, are generated. The time needed to reach the maximal current value depends on the amplitude of the US oscillations and the polarity of the molecules of the liquid. When the amplitude of the US oscillations does not exceed 5 μm, the formed microstreams are insufficient to induce the necessary mobility of the ions and the process of the current increasing is extended in time. At the amplitude of 7−8 μm, the time needed to reach the current maximum reduces and its value increases, since the maximal quantity of ions is involved in the mass transfer. When the amplitudes exceed 10 μm, the current extremum can be reached in the minimum time. The current amplitude decreases owing to the dissipative action of the cavitation cloud on the directionality of the ion stream.

The character of the temporal variation of the current in the liquid medium also depends on the potential of the grid electrode between the radiator and the main electrode. The current value increased on average by three times at the positive potential at the grid electrode. At the negative potential, the current changed its direction and its amplitide decreased. This can be explained by the fact that the positive ions of the liquid medium are mainly involved in the charge transfer.

Investigations of the US action on weakly ionized liquids (liquid glass) showed that, when a potential is applied to the radiator, the current between the electrodes increases by 20%. The current maximun was reached during the time of 130 s. The amplitude of the current through the liquid increased by 1.6 times when zink microparticles, which acquire a positive charge in the process of the US activation, were introduced. When formic alcohol containing negative OH ions was used, the initial current level was 3 times lower, and the current's amplitude exhibited a more pronounced extremum. We could not observe the electrokinetic effect in metallic melts owing to their high conductivity and the lack of free current carriers. However, a current variation was registered.
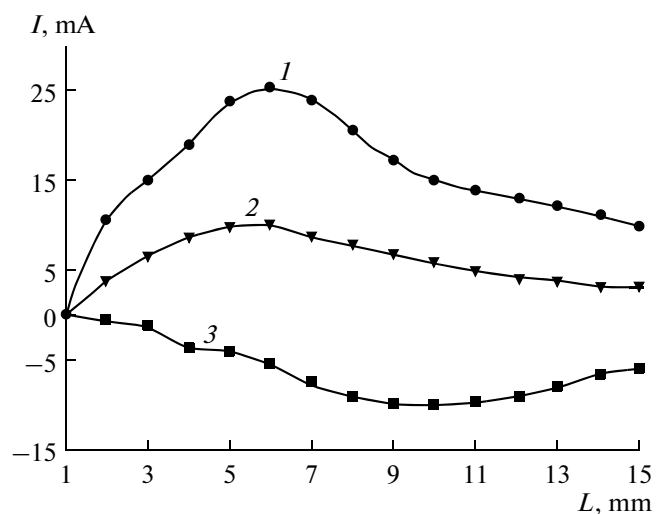

Fig. 3. Dependences of the current variation in the liquid in the US field versus the interelectrode distance. (*1*) Water with Cl ions, (*2*) organic acid, (*3*) distilled water.

Since charged particles with various concentrations and mobility are present in the liquid medium simultaneously, the total density of the flux of the particles in a of unit time amounts to

$$J_{el} = \sum_{i=1}^{n} B_i C_i F,$$ (1)

where B_i is the ion mobility, C_i is the concentration of the ions of the active reaction component in the melt, and F is the strength of the US field.

The current's value due to the electric field induced in the liquid medium is as follows:

$$I = \sum_{i=1}^{n} B_i C_i Q_i F S,$$ (2)

where Q_i is the ion charge, and S is the flux's cross section.

The appearance of an electric field in the liquid medium and the activating action of the US field influence the mass transfer processes. One should add to the diffusion flux owing to the gradient of the concentration of the diffusing substance J_d the flux of particles arising owing to the action of the pressure of the US field J_{US} and the flux of the ions under the action of the forces of the electric filed J_{el}. Then, the total flux of the diffusing particles amounts to

$$J = J_d + J_{US} + J_{el}$$

$$= -D\frac{\partial C}{\partial x} + UC_1 \cos\beta + \left(\sum_{i=1}^{n} B_i C_i\right) F,$$ (3)

where C_1 is the concentration of the mobile particles, U is the velocity of the particles in the US field, β is the angle between the forces of the US field and the diffusion flux, and α is the angle between the vectors of the electric field and the diffusion flux.

The force of the US field, which acts on the flux of the particles with the cross section S, is

$$F = \rho c \omega A S.$$ (4)

Substituting Eq. (4) in (3), we obtain

$$J = -D\frac{\partial C}{\partial x} + \upsilon \pi c \varpi A S C_1 \cos\beta.$$ (5)

The combined action of the US and electric fields when the directions of their vectors coincide intensifies the diffusion processes of the active reaction components in the liquid medium. However, since the intensity of the electric field induced in the liquid medium is low, the electric transfer currents are insignificant and do not exert considerable activation action on the mass transfer processes.

With the aim to increase the intensifying factors and the intensity of the cavitation processes in the liquid media, it was proposed to pass using an external power source an electric current with a density of 10−100 A/m^2 from the US radiator to the workpiece or to a contact element on the workpiece [7]. In a polar liquid under the action of a direct electric current, the mass transfer of ions increases. The reduction occurs of the hydrogen ions in the form of gas bubbles with dimensions of 50−100 μm, which are the cavitation nuclei. The continuous accumulation of the cavitation nuclei in the working zone and their collapse under the action of the US oscillations increase the intensity of the cavitation processes. This facilitates the process of the destruction of grease films on the workpiece's surface and increases the cleaning quality owing to the more uniform distribution of the cavitation nuclei over the entire surface under the action of the current force lines.

With the aim to increase the locality and productivity, the electric field is oriented so that the hydrogen ions move to the radiator and reduce in the form of gas bubbles. When the amplitudes of the oscillations are considerable, near the radiator's surface, a rapid growth of the bubbles to the critical dimensions and their collapse occur; this is accompanied by intensive cavitation effects. The value of the current passing through the liquid depends on the liquid's polarity and the dimensions of the treated workpiece. The greatest increasing of the cavitation pressure by a factor of 2−2.5 measured using a cavitometer was registered at the optimal current density of 10−100 A/m^2.

Under the combined action of the US and electric fields on melts, the appearance of the electrodiffusion process depends on the correlation of the forces, which act on the thermally excited metal ion, both in the direction opposite to the electric flux (the action of the external field) or in the direction of the electron flux (electron wind). The influence of the electric field is small owing to the shielding influence of the electrons; therefore, the force of the electron wind prevails; it increases with the current density increasing. Consequently, there is a greater probability for the excited ion to transform into a vacancy when it moves in the direction of the electrons than when it moves in the opposite direction. Therefore, the vacancies move to the negative pole, and the metal ions move to the positive pole; this increases the width of the diffusion zone.

When the current densities exceed 1−1.5 A/mm^2, the directional diffusion of the solder components or the diffusion of the connection material into the solder owing to the electromigration of the particles of easily diffusive metals increases the width of the diffusion zone and the durability of the connections [8].

When the currents are lower than 10 A, the short range order of the particles in the melt becomes distorted owing to the microstreams and cavitation effects. This increases the resistance of the melt and, respectively, decreases the current through it by 50−80 mA (Fig. 4). When the current exceeds 10 A, a consider-
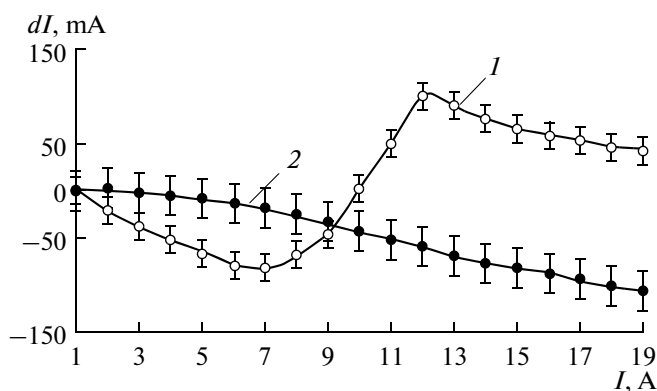
Fig. 4. Dependences of the current variation in the melt under the US activation versus the current value for various amplitudes of oscillations A, μm: (*1*) 5 and (*2*) 15.

type in them owing to the increasing of the mobility of the charge carriers and the appearance of their directed mass transfer from the radiator under the action of the pressure of the US wave. The combined action of the US and electric fields on the liquid media owing to the action of the electrokinetic effects of the first type and the directed motion of the cavitation nuclei creates conditions for the intensification of the diffusion processes and dissolution and emulgation in the treatment zone. This allows one to facilitate the processes of the US cleaning of the surfaces of workpieces in polar liquid media. The combined action of the US and electric fields provide the possibility to increase the durability of soldered connections owing to the enhancement of the diffusion processes at the melt—solid body interface.

able mass transfer of charge carriers and their ordered motion between the electrodes arise. This increased the current through the melt to 100 mA at the amplitude of 15 μm. When the current exceeded 12 A, the solder intensively heated; this increased its resistance and, consequently, the current variation through the melt decreased.

The durability of the connections of the POS 61 solder with the aluminum samples versus the direct current in the direction from the radiator to the workpiece (frequency of 22 kHz, amplitude 10 μm, temperature 240°C, and time 10 s) increases for the currents exceeding 10 A and decreases when the current exceeds 15 A [9].

The electrical stimulation of the diffusion of the solder components into the material of the workpiece, which can be associated with the electrotransfer in the melted solder at high current densities [10], is a probable cause that the durability increases.

The passing of the current through the zone of interaction in the direction from the solder to the base increases the durability of the connection by 1.5—1.8 times, since the width of the diffusion zone increases owing to the electromigration of aluminum to the solder. The width of the diffusion zone registered using a scanning electron microscope in this case amounted to about 4 μm for the POTs 10 and POS 61 solders.

CONCLUSIONS

The action of an intensive US field on polar liquid media induces electrokinetc phenomena of the second

REFERENCES

1. Leighton, T.G., *The Acoustic Bubble*, London: Academic, 1994.

2. Prokhorenko, P.P., Dezhkunov, N.V., and Konovalov, G.E., *Ul'trazvukovoi kapillyarnyi effect* (Ultrasonic capillary effect), Minsk: Nauka i Tekhnika, 1981.

3. Margulis M.A., *Sonochemistry and Cavitation*, London: Gordon and Breach, 1996.

4. Abramov, O.V., *High-intensity Ultrasonics: Theory and Industrial Applications*, Amsterdam: OPA, 1998.

5. Mason, T.J., and Lorimer, J.P., *Applied Sonochemistry: Uses of Power Ultrasound in Chemistry and Processsing*, New York: Wiley, 2002.

6. Rumak, N.V., Bondarik, V.M., and Lanin V.L., Electrical Effects in Liquids and Melts under the Action of Ultrasonic Oscillations, *Dokl. Akad. Nauk. Belar.*, 1994, vol. 38, no. 2, pp. 115—118.

7. Anufrief, L.P., and Lanin, V.L., Belarus Patent no. 7318, *Afits. Byul. Dzyarzh. Pat. Ved. Resp. Belarus*, 2005, no. 46, p. 135.

8. Lanin, V.L., Electrical Phenomena in Liquids and Melts by Ultrasound Processing, *Proc. 3rd Conf. on Applications of Power Ultrasound in Physical and Chemical Processing,*, Paris, 2001, pp.143—146.

9. Lanin, V.L., Activation of Soldered Connections in the Process of Formation Using the Energy of Ultrasonic and Electric Fields, *Surf. Eng. Appl. Electrochem.*, 2008, vol. 44, no. 3, pp. 235—240.

10. Mikhailov, V.A., and Bogdanova, D.D., *Electroperenos v zhidkikh metallakh. Teoria i prilozheniya* (Electrotransfer in Liquid Metals. Theory and Applications), Novosibirsk: Nauka, 1978.

ELECTRICAL PROCESSES
IN ENGINEERING AND CHEMISTRY

Study of the Possibility to Synthesize Nanocarbon at Electric Discharge in Solutions of Organic Acids. Part I: Choosing the Working Fluid and Generator Parameters

L. Z. Boguslavskii, N. I. Kuskova, S. A. Khainatskii, and A. N. Yushchishina

Institute of Pulse Processes and Technologies, National Academy of Sciences of Ukraine,
pr. Oktyabrskii 43a, Nikolaev, 54018 Ukraine
e-mail: boguslavsky@mail.ru, defr@iipt.com.ua, iipt@iipt.com.ua

Received December 23, 2010

Abstract—The conditions necessary for performing a pulse corona discharge with a continuous plasma mass in a liquid containing carbon are determined. The organic compositions used as electrolytes have been chosen. There is proposed an approach to calculate the external controlled parameters of the pulse generator.

DOI: 10.3103/S1068375511040053

INTRODUCTION

The advancement of nanotechnologies and the wide use of nanomaterials in commercial production make the problem of the development of new effective methods of their synthesis more and more topical. After the nanocarbon materials have been discovered, the methods for synthesizing them are permanently studied and improved. The majority of the known synthesis methods are based on the processing of graphite and other solidphase carbon raw materials. Pyrolysis is the most used procedure employing gaseous raw material. In the IPPT of the National Academy of Sciences of Ukraine, there was previously proposed a way of processing a liquid raw material based on the method of the electroexplosive decomposition of carbon liquids [1] permitting one to rapidly produce record-setting macroquantities of nanocarbon in comparison with other approaches.

The synthesis of nanocarbon materials in an electric discharge plasma in organic liquids is the principle of this method, though it has some limitations along with its high efficiency and productivity. As all liquids used for that purpose [2] are dielectric ones, the resistivity of which is more than 10^{10} Ohm cm, the discharge in them is characterized by the formation of a unit single-path plasma channel with its length nearly coinciding with the interelectrode gap's length. The increase of the discharge channel's plasma volume in order to increase the nanomaterial's synthesis productivity within a unit pulse is possible only with a significant growth of the field intensity in comparison with the breakdown one while having a substantial impact on the energy expenditures. A solution of the problem is to increase the liquid's volume subjected to the three-dimensional electrodischarge effect, which should in this case be searched for in a considerable growth of the electric

conduction of the processed media, as a strong dependence of the lieder system's structure on the solution's conductivity (branching, the number of leaders) is a well known and old established fact [3].

Producing electrolytes on the basis of very soluble (for instance, in water) carbonaceous compounds (for example, organic acids) or organic solvents can be one of the possible ways to solve this problem. Thus, the purpose of this work is to determine some working carbon media and ranges of parameters of electric devices necessary for producing carbon nanomaterials with the three-dimensional electrodischarge processing of carbon media. This work is aimed at the solution of an important research problem—the search for new physicotechnical ways for synthesizing pure nanocarbon on the basis of a three-dimensional electrodischarge effect on liquid hydrocarbon media with the help of pulse discharges.

SOME PECULIAR FEATURES OF A PULSE ELECTRIC DISCHARGE IN LIQUID

As the system's main structure, as was mentioned above, depends in a rather complicated way on the solution's conductivity, the electrode system, and such parameters of the discharge circuit as the initial voltage and capacity of the bank of capacitors, for definiteness we assume that hereafter all the processes should be considered in the neighborhood of the so called critical field intensity [4], whose value for water is $\cong (4-6) \times 10^6$ V/m. In such cases, it is possible to determine some conventional ranges of the electric conduction characterizing the level of the leader system's branching. Thus, the discharge in distilled water ($\sigma_0 \approx 10^{-6}$ S/m) is characterized by a unit single-path leader (in tap water ($\sigma_0 \approx 10^{-3}$ S/m) by a branched

leader system, while in sea water ($\sigma_0 \approx 2$ S/m) by a powerful brush corona. Such a pulse corona in water is a developed system of leaders with a bushlike spatial orientation. It appears in the discharge gap with a non-uniform and sharply nonuniform field and is characterized by the fact that no leader, growing deep into the gap, reaches the opposite electrode. Therein lies an essential difference between the underwater pulse corona and "linear" underwater spark discharge.

Thus, as the external conditions change, in particular the electrolyte's electric conduction σ_0 increases, the number of leaders grows; their diameter at the basis becomes larger; and, at some electric conductions, they cover the whole free surface of the electrode forming a continuous plasma mass (CPM). At some critical values of σ_0, the leaders merge together from the very start of the discharge, and the CPM fully copies the electrode's shape. If the end of the noninsulated part of the electrode has the form of a hemisphere, then the plasma around it has the shape of a hemisphere too. Owing to the considerable electric conduction of the medium, the discharge current can run up to dozens of kiloamperes [4]. The dense low-temperature plasma of a corona discharge in electrolytes with a temperature of about 10^4 K should decompose any organic molecules, and, due to the branched plasma corona, a much larger mass of liquid can be affected in comparison with the known electroexplosive methods.

A pulse corona discharge (PCD) in liquid, having stable electric characteristics, also possesses a number of other merits. For instance, its ignition is possible on 100 and more points in order to increase the volume of the processed liquid. Such an approach is realized in multiflamed PCD [5]. There is also possible an extended (linear) PCD. In general, the PCD properties allow one to create plasma regions with any prescribed geometry. Considering all these facts, it may be concluded that the conditions for the realization of PCD with CPM should be developed in order to synthesize carbon nanomaterials with an electric discharge in a liquid.

Usually PCD is realized in aqueous solutions of electrolytes with sodium chloride solutions being the best studied ones. The data on the effect of the chemical composition of different impurities on the discharge development process are rather contradictory. Thus, the discharge in aqueous solutions of different chemical substances with electric conduction in the range from 5×10^{-3} to 74 S/m has been studied in [6]. It has been established through oscillographic testing that the behavior of all the solutions at high field intensity depends only on the σ_0 of the solutions but not on the chemical composition of the impurities. Thus, there is noted the dominant influence of the conductivity on the high voltage behavior of a solution. A similar conclusion is reached in [7] too.

However, in [8], it is noticed that, at the same value of σ_0, the leaders appear earlier when atoms with comparatively small critical potentials and ionization potentials (Na and K) are present in the liquid. The differences in the discharge's development depending on the type of ions and their concentration in the aqueous solution at the value of σ_0 in the range from 0.1 to 13.5 S/m were also observed in [9]. With the chemical composition changing, the discharge's character can change too (transiting from a discharge with breakdown into a corona discharge ([8])). In the case of a corona discharge in solutions with $\sigma_0 = 13.5$ S/m, though the current oscillograms were almost the same, differences were observed in the glow's duration from the maximum intensity to its complete attenuation. Besides, unlike alkalis and a neutral medium where the polarity is slightly expressed, in an acid medium the discharge develops mainly from the positive electrode [7]. All these factors should be taken into account when choosing working liquids and calculating the parameters of a power center.

CHOOSING A WORKING LIQUID

As mentioned above, high electric conduction in the range from 1 to 10 S/m is one of the main requirements imposed upon organic liquids to realize a corona discharge in them. However, organic substances are for the most part nonpolar or low polar in nature. Formamide is an exception with its permittivity $\varepsilon = (109 \pm 1.5)$ F/m being larger than that of water and its electric conduction being $\sigma_0 = 26.3$ S/m.

Nevertheless, there are known some organic compositions used as electrolytes. For example, among these are the aluminizing electrolytes including 1,2,4,5-tetramethylbenzol, aluminum bromide, and xylene. Aqueous solutions of organic acids (oxalic, citric, antiscorbutic, amber, and acetic ones) have conducting properties too. One might expect that aqueous solutions of sugar, soluble starch, gelatin, and surface-active agents should have some electric conduction.

However, alongside the required conductivity, an organic substance—a raw material to produce carbon nanomaterials—should be relatively available, safe under the conditions of an electric discharge, and contain a big mass fraction of carbon atoms. We think the composition for aluminizing is rather exotic; besides, the method of its production is laborious and energy-consuming. Other mentioned substances possess a complex of the desired qualities to a greater or lesser extent. The properties of some organic substances—possible raw materials to produce CNM in a corona discharge—are presented in Table 1 [10]. It follows from the tabulated data that the surface-active agents (SAA) have the greatest content of carbon; moreover, many ionogenic SAA are readily soluble in water and alcohols. A lot of them are safe and available, so they are the most promising raw materials to produce

Table 1. Properties of some organic substances

Organic material's name	Chemical formula	Solvability	σ_0, S/m	Dipolar moment, C m	Mass fraction of carbon atoms, %
Formamide	$HCONH_2$	Water + Benzol − Ethanol +	26.3	11.24×10^{-30}	27
Oxalic acid	HOOCCOOH	Water + Benzol − Ethanol +	5.08 (3.5%$_{(mass)}$, 18°C), 7,83 (7%$_{(mass)}$, 18°C)	0.1×10^{-30}	27
Acetic acid	CH_3COOH	Water + Benzol +/− Ethanol +		5.6×10^{-30}	40
Amber acid	$C_4H_6O_4$	Water + Benzol − Ethanol +		5.5×10^{-30}	40.7
Citric acid	$(HOOCCH_2)_2C(OH)COOH$	Water + Benzol − Ethanol +		−	37.5
Antiscorbutic acid	$C_6H_8O_6$	Water + Benzol − Ethanol +		−	41
Glucose	$C_6H_{12}O_6$	Water + Benzol − Ethanol +/−		47×10^{-30}	40
Sodium dodecyl sulphate (SAA)	$C_{12}H_{25}NaO_4S$	Water + Benzol − Ethanol +		−	50

Note: In column 3, the sign (+) denotes that the substance is soluble in the indicated solvent, (−) not soluble, and (+/−) slightly soluble.

CNM. Besides, they can be by-products (wastes) of a number of industries with their utilization through conventional methods being often rather difficult and energy consuming.

The majority of the tabulated compounds are soluble in ethanol, being itself a source of carbon for synthesizing nanocarbon when PCD is ignited in it.

The solutions of organic substances presented in the table are weak electrolytes with the degree of dissociation $\alpha \ll 1$. The conductivity of weak electrolytes is considerably lower than the conductivity of strong electrolytes with the same concentration determined by the little degree of dissociation of a weak electrolyte. With its concentration growing, the number of molecules capable of dissociating increases simultaneously, but the degree of the dissociation reduces. As is seen, the information on the specific and molar electric conductivity of the solutions of weak electrolytes is quite poor in the literature. For oxalic acid, only data for two solution concentrations are presented in [11], and there is no information for citric acid and other acids. The comparison of the data for oxalic acid and the dependence of the electric conduction of aqueous solutions of sodium chloride on the

mass concentration of the solutions show that, within the presented range of values, the electric conduction of an oxalic acid solution is half less than that of an NaCl solution. For other acids, this ratio is even smaller. Nevertheless, the range of values of the initial conductivity of the saturated solutions of organic acids with special parameters of the discharge circuit and electrode system makes it possible to realize PCD with CPM with breaking of organic compounds' molecules into atoms.

The calculation of the external controlled parameters of a pulse generator as part of an electrodischarge setup for the plasma chemical synthesis of nanocarbon materials can be at least performed through two methods. The first one is the "direct" method: based on the physically self-consistent model of PCD phenomenon, it is possible to calculate the dependence of the CPM characteristics on the external parameters and to determine by it the combinations of them for "extreme" states of CPM with the maximum volume of the discharge plasma. There have been proposed a lot of such models including complex systems of nonlinear integro-differential equations in partial derivatives that in sufficiently accurate approximations describe the processes within the discharge gap: the

dynamics of the CPM and the plasma–liquid transition layer and the nonuniform energy dissipation in the electrolyte (see, for example, [12]). A shortcoming of this method is its high complexity and that the obtained results are insufficiently illustrative, as such systems can be solved only through numerical ways.

The second method—the indirect one—is based on the approximate analytic calculations of a number of PCD operational parameters, such as the maximum pressure at the boundary of the CPM and its radius, the maximum pressure on the compression front over a distance from the CPM, and the electroacoustic efficiency of the discharge, while knowing that their "extreme" values correspond strictly to the states of CPM with the maximum discharge plasma volume. We have carried out such an approximate calculation of the PCD parameters for one-point, many-point, and extended electrode systems; the design procedure is presented in [13–15].

A number of simplifying assumptions when setting up the problem, although they somewhat lower the accuracy of the description of the discharge processes, allow one to obtain analytic relations for the highest parameters of the PCD and its electroacoustic efficiency when the maximum power is attained. To estimate the external controlled parameters in a system with one point anode by the design procedure proposed in [13], it is essential to be primarily guided by the production conditions for PCD with CPM:

$$\beta = \frac{\sigma_0 U_0^2 (LC)^{3/2}}{\rho_0 r_{el}^4},$$

where σ_0 is the electrolyte's electric conduction, U_0 is the voltage of the capacitor storage's charge, C is the storage capacity, L is the discharge circuit's inductance, r_{el} is the electrode point's rounding radius, and ρ_0 is the electrolyte's density. The criterion β is the ratio set for the flow densities of the electric field energy and the power of the dynamic liquid medium's head to the unity of length both of the point's linear dimension and of the length of the disc electrode's circle. The production of PCD with CPM is possible only at $\beta > 0.2$; otherwise, it is necessary to change the external controlled parameters. This criterion is the same for extended electrode systems, but, in the case of many-point systems with n electrodes, (nr_{el}) is written instead of (r_{el}).

The calculation of the electric discharge mode by the damping decrement value should be the next step. Expressions for the damping decrement dependence for PCD with CPM with different geometries of the electrode system are presented in Table 2.

Here, δ is the logarithmic damping decrement, h is the length of the protruding (noninsulated) part of the electrode, l is the point's length, and R is the disc's radius. In the case when $\delta < 1$, the discharge will be oscillatory; at $\delta \approx 1$, the discharge is critical; and, at

Table 2. The dependence of the damping decrement for PCD with CPM with different geometries of the electrode system [13–15]

Electrode system		
One point anode	Linear point	Disc electrode
$\delta = \dfrac{1}{4\pi\sigma_0 r_{el}}\sqrt{\dfrac{C}{L}}$	$\delta = \dfrac{\ln\left(\dfrac{h}{r_{el}}\right)}{2\pi\sigma_0 l}\sqrt{\dfrac{C}{L}}$	$\delta = \dfrac{\ln\left(\dfrac{h}{r_{el}}\right)}{4\pi\sigma_0 R}\sqrt{\dfrac{C}{L}}$

$\delta > 1$, the discharge is aperiodic. Critical and aperiodic modes of discharge are mainly realized with PCD. With CPM being simultaneously ignited on n identical points, it is necessary to consider one more condition determining the largest number of points on which PCD will be reliably ignited with CPM [14]:

$$n \ll \frac{\alpha}{\rho_0 c_p} \frac{U_0^2 C}{r_{el}^3}.$$

Here, α is the temperature coefficient of the electric conduction, and c_p is the liquid's heat capacity.

In the case of a long point, it should be considered that there exists the largest linear size l_m of it on which will be reliably ignited PCD along its whole length [15]:

$$l_m = \frac{0.1\alpha}{\rho_0 c_p} \frac{U_0^2 C}{\pi r_{el}^2 \ln\dfrac{h}{r_{el}}},$$

and, for a disc electrode, the value of the largest disc radius is

$$R_m = \frac{0.1\alpha}{\rho_0 c_p} \frac{U_0^2 C}{2\pi^2 r_{el}^2 \ln\dfrac{h}{r_{el}}}.$$

When calculating the external controlled parameters, it should also be considered that, in the case of a one-point electrode system, the CPM radius corresponding to the maximum power grows with an increase of the stored energy $W_0 = C U_0^2/2$, the liquid conduction σ_0, with the decrease of the induction L, and the initial electrode radius r_{el}. Among the external controlled parameters, the initial voltage on the storage battery and its capacity—$a_m \sim U_0^{1/2}$, $C^{1/2}$; respectively, the volume $\sim U_0^{3/2}$, $C^{3/2}$—have the most significant effect on the CPM's largest volume in the case of a one-point electrode system. The same dependence also holds for each electrode within a many-point electrode system.

In the case of extended plasma plungers—a linear semicylinder and an external sesquicylinder—the character of the dependence of the plasma plunger's maximum radius on the external controlled parame-

ters is the same. The difference is in the total value of the coefficients and the character of their dependence on the linear parameters of the electrode system determined by their different geometries. At the same time, in comparison with a one-point electrode system, in the case of an extended plasma plunger, the dependence of its largest radius and the volume on the external controlled parameters is the most significant. If in the first case $a_m \sim U_0^{3/2}$, $C^{1/2}$ and, respectively, the volume $\sim U_0^{3/2}$, $C^{3/2}$, then, in the second case, $a_m \sim U_0^{2/3}$, $C^{2/3}$ and, respectively, the volume $\sim U_0^2$, C^2. If the plasma continuity coefficient is taken into account [16], then, for any electrode system, the actual volume of the plasma at high liquid conductions, PCD forming with CPM, there may appear some times larger than that calculated according to [13–15].

CONCLUSIONS

Thus, the conditions required to produce a pulse corona discharge with a continuous plasma mass in a carbonaceous liquid are only realized when all the particular features of such a discharge are taken into account, the working media are selected correctly, and the external controlled parameters of the power center are preliminarily calculated. The creation of an electrode system with a sharply nonuniform field at the positive point (edge, etc.) is the first necessary condition with the field intensity at the point exceeding the critical one ($\sim 10^7$ V/m). The conditions should be created for PCD with CPM in order to obtain the most efficient synthesis of carbon nanomaterials at an electric discharge in liquid. Thus, one should choose a solution of electrolytes with the highest conductivity and, when possible, with the presence of ions with little potential for excitation and ionization as the working medium. In addition, the organic substance—the raw material to produce carbon nanomaterials—should be relatively available, safe under the conditions of an electric discharge, and contain a large mass fraction of carbon atoms.

When estimating the external controlled parameters of a generator, one should be guided by the conditions of producing PCD with CPM: the calculation of the electric discharge mode by the damping decrement value for electrode systems with different geometries and conditions determining the largest amount of points on which will be reliably ignited PCD with CPM or the largest length of the point for a linear plunger or the value of the maximum radius of a disc for a disc electrode on which PCD will be ignited along the whole edge.

Considering the stronger dependence of the plasma's volume on the external controlled parameters for extended electrode systems and the fact that the linear size of the electrode system (greatly exceeding in most cases the plasma mass's radius) is included

into the expression for the plasma plunger's volume as the third dimension, one should expect that a system with an extended plasma plunger appears to be more efficient.

The results of the experimental investigations on synthesizing nanocarbon at an electric discharge in solutions of organic acids are presented in the second part of the work.

REFERENCES

1. Kuskova, N.I., Boguslavskii, L.Z., Rudi', A.D., Uvarov, V.N., Ivashchuk, L.I., Perekos, A.E., and Oreshkin, V.I., Electroexplosive Methods of Synthesis of Carbon Nanomaterials, *Metallofiz.. Nov. Tekh.*, 2008, vol. 30, no. 6, pp. 833–847.

2. Kuskova, N.I., Boguslavskii, I.Z., Smal'ko, A.A., and Zubenko, A.A., Obtaining Nanocarbon Using the Electric Discharge Treatment Method of Organic Liquids, *Surf. Eng. Appl. Electrochem.*, 2007, vol. 43, no. 4, pp. 269–275.

3. Naugol'nykh, K.A. and Roi, N.A., *Elektricheskie razryady v vode,* (Electric Discharges in Water), Moscow: Nauka, 1971, p. 155.

4. Boguslavskii, L.Z., Krivitskii, E.V., and Petrichenko, V.N., Corona Discharge in Strong Electrolytes, in *Teoriya, eksperiment, praktika elektrorazryadnykh tekhnologii* (Theory, Experiment, Practical Application of Electrodischarge Technologies), no. 1, Kiev: Naukova Dumka, 1993, pp. 8–12.

5. Boguslavskii, L.Z., Bristetskii, E.V., Krivitskii, E.V., and Petrichenko, V.N., Investigation of Ignition of Multi-Flamed Corona Discharge in Low Conducting Electrolytes, in *Teoriya, eksperiment, praktika elektrorazryadnykh tekhnologii* (Theory, Experiment, Practical Application of Electrodischarge Technologies), no. 4, Kiev: Naukova Dumka, 2002, pp. 7–15.

6. Brodskaya, B., Eiskop, R., and Payu, A., Peculiar Features of Pulse Discharge Development in Strongly Conducting Liquids, *Izv. Akad. Nauk ESSR, Khim. Geol.*, 1968, vol. 17, no. 3, pp. 251–256.

7. Krivitskii, E.V., Petrichenko, V.N, and Bondarets, L.M., Investigation of Energy Characteristics of Pre-Breakdown Stage of Underwater Spark Discharge, *Zh. Tekh. Fiz.*, 1977, vol. 47, no. 2, pp. 319–325.

8. Trofimova, N.B., Investigation of Breakdown of Conducting Nondegassed Liquids, in *Proboi dielektrikov i poluprovodnikov* (Breakdown of Dielectrics and Semiconductors), Moscow–Leningrad: Energiya, 1964, pp. 219–224.

9. Brodskaya, B., Trapido, G., and Gubergrits, M., Intensity of Light Flashes and Electric Characteristics of High-Current Discharges in Electrolytes with Different Compositions, *Izv. Akad. Nauk ESSR, Khim. Geol.*, 1972, vol. 21, no. 4, pp. 375–378.

10. Chemistry. http://www.xumuk.ru; Wikipedia. http://ru.wikipedia.org

11. *Spravochnik po elektrokhimii*, (Electrochemistry), Reference book, Sukhotin, A.M., Ed., Leningrad: Khimiya, 1981, p. 485.

12. Shamko, V.V. and Boguslavskii, L.Z., Mathematical Simulation of Corona Discharge in Strong Aqueous Electrolytes, in *Teoriya, eksperiment, praktika elektrorazryadnykh tekhnologii* (Theory, Experiment, Practical Application of Electrodischarge Technologies), no. 4, Kiev: Naukova Dumka, 2002, pp. 34–44.

13. Boguslavskii, L.Z., Engineering Methods of Calculating the Technological Parameters of a Pulse Corona Discharge in Strong Electrolytes: 1. Single-Point Electrode Systems, *Surf. Eng. Appl. Electrochem.*, 2009, vol. 45, no. 5, pp. 390–396.

14. Boguslavskii, L.Z., Engineering Methods of Calculating the Technological Parameters of a Pulse Corona Discharge in Strong Electrolytes and for a Multipoint Electrode System, *Surf. Eng. Appl. Electrochem*, 2009, vol. 45, no. 6, pp. 492–494.

15. Boguslavskii, L.Z., Engineering Methods of Calculating the Technological Parameters of a Pulse Corona Discharge in Strong Electrolytes and for an Extensive Plasma Piston, *Surf. Eng. Appl. Electrochem.*, 2010, vol. 46, no. 2, pp.131–137.

16. Boguslavskii, L.Z., Kucherenko, V.V., and Krivitskii, E.V., Dynamics of Pulse Corona Discharge in Aqueous Electrolytes, *Preprint of Inst. of Pulse Processes and Technologies, Nat. Acad. Sci. Ukr.*, Nikolaev, 1993, no. 22, p. 41.

ELECTRICAL PROCESSES
IN ENGINEERING AND CHEMISTRY

Effect of the Spreading of the Contact Spot
on the Pulsed Heating of Electrodes

O. M. Pavleino, V. A. Pavlov, and M. A. Pavleino

St. Petersburg State University, Electrophysics Research and Education Center, Faculty of Physics,
ul. Ul'yanovskaya 3, St. Petersburg, Petrodvorets, 198504 Russia
e-mail: pavleyno@mail.ru
Received November 15, 2010; in final form, January 19, 2011

Abstract—A numerical calculation of the pulsed heating of electrical contacts in a wide temperature range up to the melting point is carried out on the basis of experimental oscillograms of the electrode voltage and current. The change in the radius of the contact spot is determined taking into account the softening of the material. It is shown that even a slight spreading of the spot can lead to a significant decrease in the contact temperature. The dynamics of the heating of the contact area are analyzed, and the distributions of the temperature and heat flows are plotted.

DOI: 10.3103/S1068375511040119

INTRODUCTION

The processes that accompany the flow of current through electrical contacts are discussed in a large number of works: from the fundamental work of R. Holm [1] and to present-day studies, a fairly complete review of which has been made, for example, in [2]. Nevertheless, a number of problems are not fully understood. This primarily concerns transient modes of the heating of contacts to significant temperatures close to the melting point and specifically the cases of high-current contacts with currents of a few tens of kiloamperes. This is particularly attributed to the complexity of the performance of experiments in a range of high currents [3]. This work concerns the simulation of these heating modes.

The most complete formulation of the problem of the heating of electrical contacts by a flowing current is a joint thermoelectromechanical contact problem. Attempts to solve it were repeatedly made [5–8]. However, it is not always possible to obtain reliable results. First of all, this is attributed to the fact that the mechanical properties of the materials of the contacts in a wide temperature range (up to the melting point) often are not known with a reasonable degree of accuracy, which can lead to errors in determining the sizes of the contact spots, which greatly change the pattern of the heating of the electrodes [3].

We propose a method of numerical calculations based on the experimentally derived time dependence of the contact voltage, which makes it possible to calculate the heating of electrodes without solving the mechanical part of the problem. In this work, we analyze the dynamics of the heating of the contact area and show the strong localization of the region of the power release and, as a consequence, the nonunifor-

mity of the temperature distribution in the contact spot. The effect of the softening of the material and the resulting spreading of the contact spot on the heating of the electrodes is revealed.

NUMERICAL CALCULATION TECHNIQUE

The numerical calculations were based on data derived during a set of experiments on the passing of pulse currents through contacts of the simplest form at which the contacts are heated up to melting. To explain the nature of the phenomena that accompany the heating of the contacts by the flowing current, the shape of the electrodes was chosen so that one circular contact spot was formed upon compression. The force of the compression of the electrodes must be sufficiently large to consider that the contact spot is not fragmented. In the case discussed below, it was 250 kg. The compression of the electrodes was carried out using a pneumatic cylinder; the force of the compression was measured with a pressure sensor. In each experiment, we derived oscillograms of the current and voltage across the sample, the resistance of the sample before and after the passage of the current, the force of tear of the contacts, and a micrograph of the contact area. The experiment is described in more detail in [3].

The algorithm for the numerical calculations was as follows. In the simulation, we assumed that the current passes through one continuous contact spot of a circular shape located along the axis of symmetry of the electrodes. The heating of the electrodes by the flowing current is described by a system of equations that includes a transient heat conduction equation and a continuity equation for the current density. We
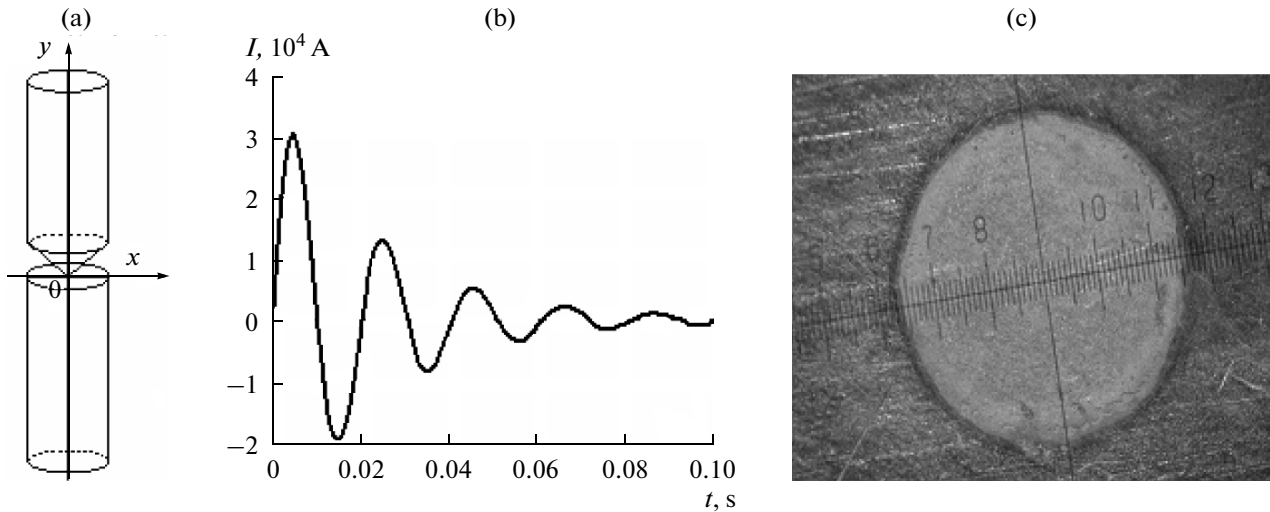
Fig. 1. (a) Schematic representation of the electrodes, (b) an oscillogram of the current, and (c) a micrograph of the contact spot.

assumed that the shape of the contact spot remains unchanged, and its radius varies during the heating. A transient problem was solved; in this case, at each instant of time, the radius of the contact spot was selected so that the numerically derived value of the voltage coincided with the experimental value with a reasonable degree of accuracy. The initial radius of the contact spot was determined from the value of the contact resistance measured before the passing of a current pulse through the electrodes taking into account the proximity of the electrode boundaries to the spot [4]. The result of the solving was the distributions of the temperature, the heat flow, the current density, the released power, and other quantities at different instants of time. The calculations were performed until the contact temperature achieved its maximum value.

The numerical calculations carried out below describe the processes that accompany the passage of a sinusoidal current with an aperiodic component through two cylindrical copper electrodes (Fig. 1a) with a height of 180 mm and a diameter of 20 mm. The base of one of them is skewed at a skew angle of 3°. The maximum value of the current in the first half-period is 30.2 kA. The respective current oscillogram is shown in Fig. 1b. Figure 1c depicts a micrograph of the region of the contact spot after the contacts are moved apart. The radius of the contact spot in the given case was approximately 0.75 mm.

NUMERICAL CALCULATION RESULTS

Figures 2a and 2b show the time dependences of the radius of the contact spot and the maximum temperature of the contact area derived via the numerical calculations. The radius of the contact spot almost preserves its constant value up to a temperature of $T \approx 600$ K and then begins to increase. This increase is

attributed to the softening of the material. The temperature dependence of the yield strength of copper, which is shown in Fig. 2c, exhibits a singularity at the same temperature value.

This brings up the question to what extent does the spreading of the contact spot affect the heating of the electrodes, and can we disregard it in numerical calculations assuming the radius of the contact spot to be constant?

Compare the results of solving the problem of the heating of electrodes by the same current (Fig. 1b) using two models. In the first model, we assume that the radius of the contact spot is constant and equal to the initial radius $a_0 = 1.05$ mm; in the other model, the spreading of the spot is taken into account. Let us see how the maximum temperature of the electrodes changes in time (Fig. 3). In the approximation of a constant radius, the melting point is achieved at the instant of 4.15 ms. By this time, taking into account the spreading of the spot, we derive a temperature value that is lower by 500 degrees. Note that, within this time, the radius of the spot has increased by only 15%. The maximum temperature in the contact area in the second case is achieved by the time of 6 ms and is 1050 K; that is, this current does not cause the melting of the electrodes.

Thus, the spreading of the contact spot caused by the softening of the material leads to a significant change in the temperature. Let us analyze why this occurs.

APPROXIMATION OF A CONSTANT RADIUS OF THE CONTACT SPOT

Consider first the heating of the electrodes for a constant radius of the spot. The contour diagram of the temperature distribution in the contact-spot
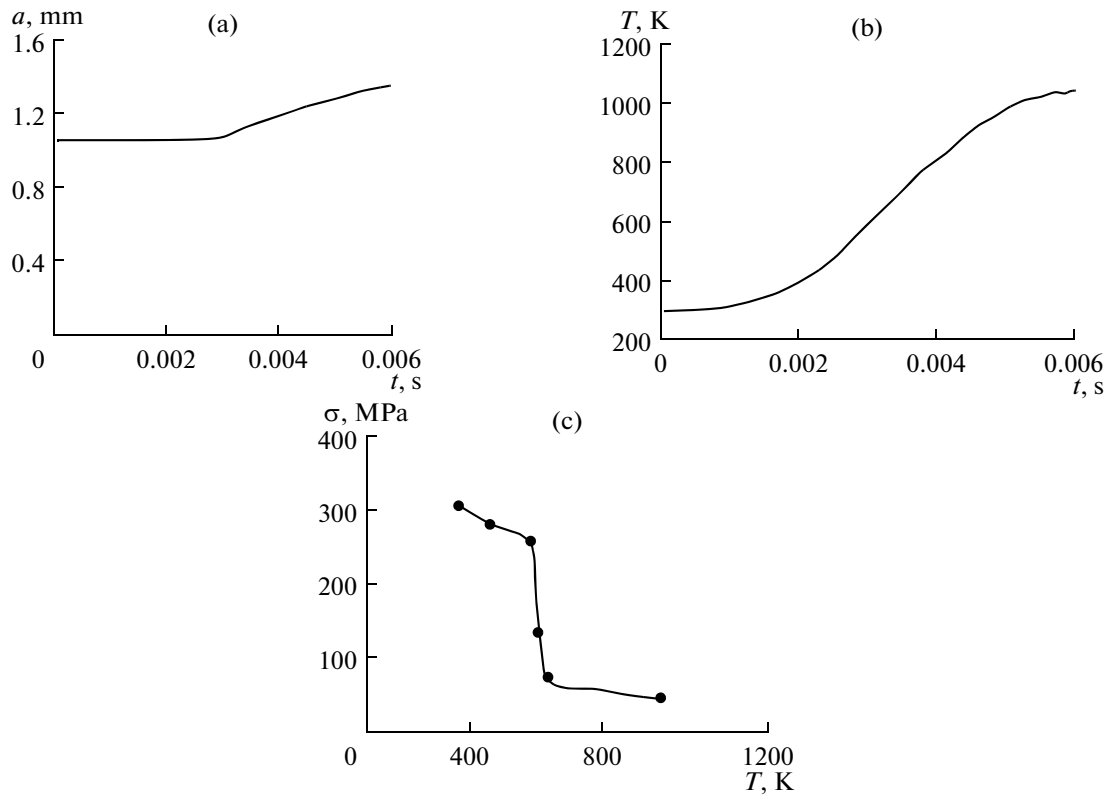
Fig. 2. (a) The time dependence of the radius of the contact spot, (b) the time dependence of the maximum temperature, and (c) the temperature dependence of the yield strength of copper.

region at $t = 4.15$ ms (when the maximum temperature is close to the melting point) is presented for one of the electrodes in Fig. 4.
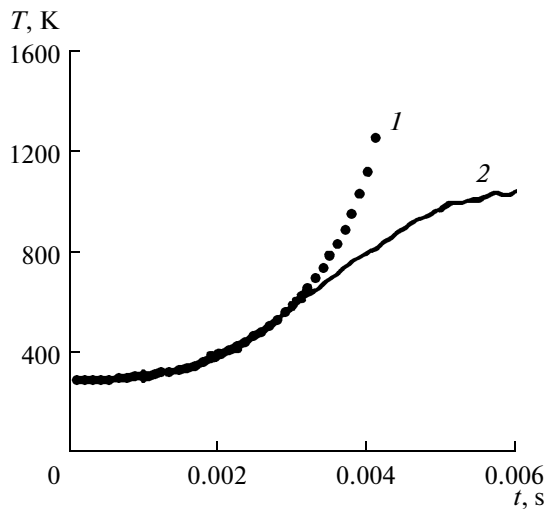
The origin of the coordinates corresponds to the center of the contact spot, the X axis lies on the surface of the spot, and the Y axis is perpendicular to it and coincides with the axis of symmetry of the electrodes. The heated area has a size of about two radii of the contact spot. The maximum temperature is achieved at the edge of the contact.

Fig. 3. Time dependence of the maximum temperature in the contact area. The solid line corresponds to the case of a constant radius of the contact spot; the dashed line denotes the case of a variable radius: (*1*) $a = $ const and (*2*) $a = a(t)$.
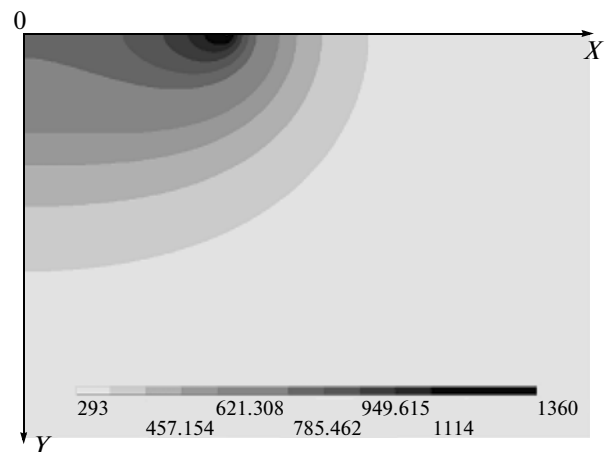

Fig. 4. Contour diagram of the temperature distribution in the region of the contact spot at $t = 4.15$ ms. The case of a constant radius of the contact spot.
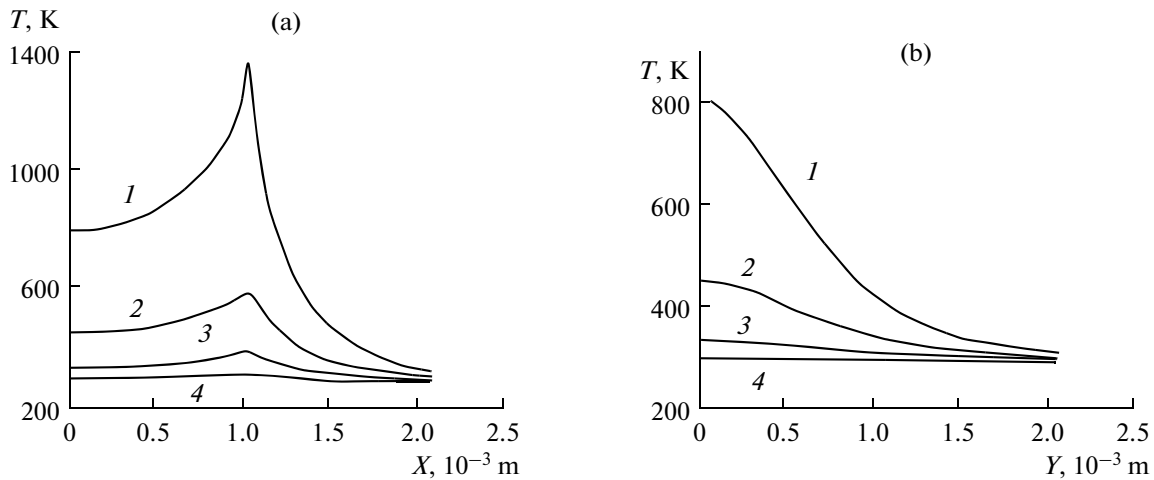
Fig. 5. Graphs of the temperature distribution at different instants of time. The case of a constant radius of the contact spot. *t*, ms: (*1*) 4.15, (*2*) 3, (*3*) 2, and (*4*) 1.
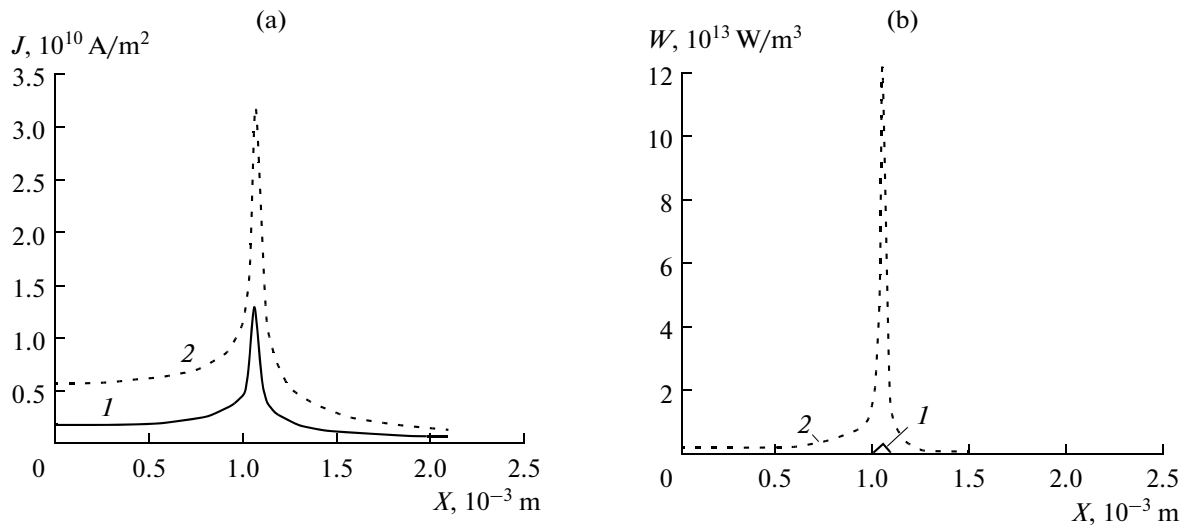

Fig. 6. Distributions of (a) the current density and (b) power at *t* = 1 and 4.15 ms. The case of a constant radius of the contact spot. *t*, ms: (*1*) 1 and (*2*) 4.15.

The dynamics of the heating are depicted in Figs. 5a and 5b, which show the graphs of the temperature distribution along the 0*X* and 0*Y* axes at different instants of time.

The temperature along the 0*X* axis undergoes a nonmonotonic change. It is maximal at the edge of the contact spot and decreases towards its center and the surface of the electrode. With the distance from the center of the contact spot, along the axis of symmetry, the temperature monotonically decreases. The heating of the contact is nonuniform. Over time, the temperature difference at the center of the contact spot and at its edge increases and, by the instant of the beginning of the melting, exceeds 500 K.

This is attributed to the fact that the distribution of the current density and, consequently, the released

power over the contact spot is strongly nonuniform (Fig. 6). The maximum current density is located at the edge on the contact spot, and its value is about 7 times higher than at its center. The distribution of the power released during the passage of a current pulse through the electrodes is similar. The power is mostly released in a narrow ring in the vicinity of the edge of the contact spot.

We now consider heat flows. The linear graphs of the distribution of the *X*-component of the heat flow along the 0*X* axis and the *Y*-component along the 0*Y* axis at different instants of time are represented in Fig. 7. Along the horizontal path, the heat propagates in the opposite directions from the region of the maximum heat evolution; in addition, the heat flow inward
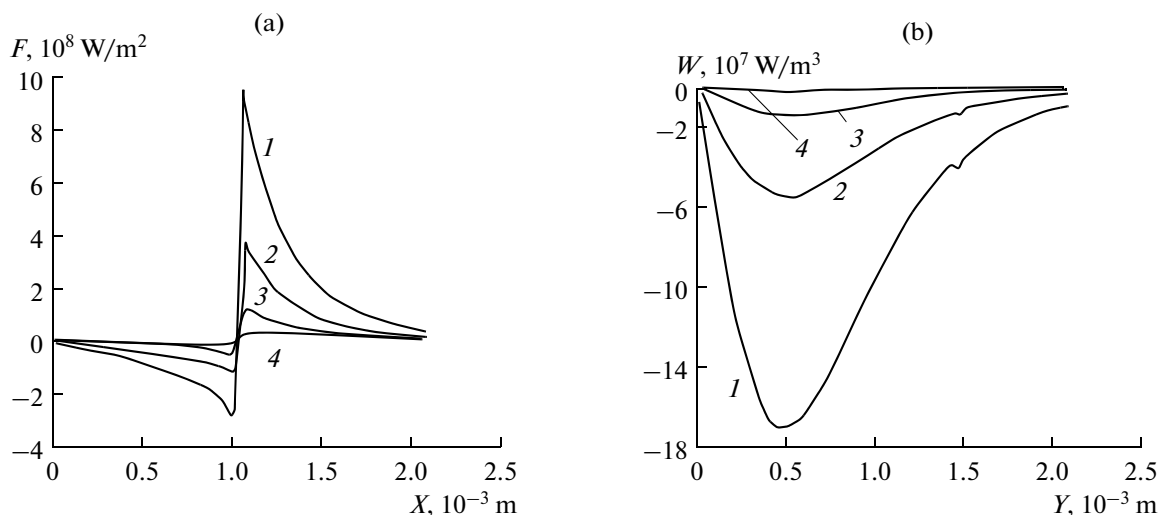
(a)

(b)

Fig. 7. Distributions of (a) the X-component and (b) Y-component of the heat flows at different instants of time. The case of a constant radius of the contact spot. t, ms: (*1*) 4.15, (*2*) 3, (*3*) 2, and (*4*) 1.

the contact spot is less than the outward heat flow at any instant of time.

REGARD FOR THE SPREADING OF THE CONTACT SPOT

We now take into account the spreading of the contact spot. The instant of the beginning of the increase in the radius corresponds to the heating of the contact area to the softening temperature. Figure 8 depicts the contour distribution of the temperature in the vicinity of the contact spot at the instant of 4.15 ms (the instant of the beginning of melting in the first case). The distribution pattern is qualitatively similar to the above case (Fig. 4); however, the contact is heated to a much lower temperature.
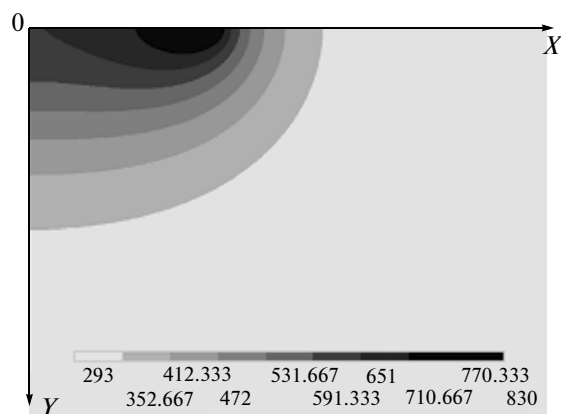

Fig. 8. Contour diagram of the temperature distribution in the region of the contact spot at $t = 4.15$ ms. The case of a variable radius of the contact spot.

For a more detailed analysis, we consider linear graphs. Figure 9 shows the temperature distribution along the $0X$ and $0Y$ axes at different instants of time.

If we compare the temperature distributions along the $0X$ axis for the two cases (Figs. 5a, 9a), we can see that, with increasing contact spot, the maximum temperature does not increase as rapidly as in the case of a constant radius, and the nonuniformity of the heating of the contact spot also decreases. In addition, the maximum temperature shifts from the center of the spot and remains on its boundary all the time. This is attributed to the respective changes in the distribution of the released power and the redistribution of the heat flows induced by the spreading of the spot.

The distribution of the current density along the $0X$ axis (Fig. 10a) has the following features. First, its maximum moves away from the axis of the electrodes after the displacement of the boundary of the contact spot and is located on the edge of the spot at any instant of time. Second, the ratio of the current density at the center of the contact spot to the value of the current density near the edge of the contact spot decreases. As in the previous case, the power (Fig. 10b) is mostly released in a ring near the edge of the contact spot, which is moving away from the center and thus contributes to the more uniform heating of the spot.

In addition, if we compare the distribution of the current density and power in the cases of a constant and variable radius of the contact spot (Figs. 11a, 11b) at the same instant of time, then we find that the maximum values of the current density and particularly the power are lower in the second case.

The above features of the distribution of the released power lead to respective distributions of the heat flows. Figure 12 shows the distributions of the X-component
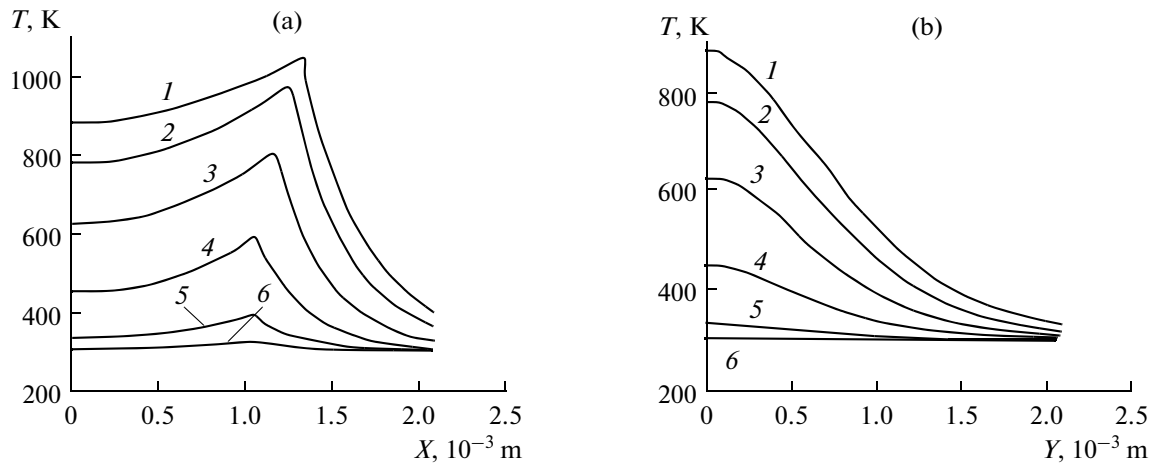
Fig. 9. Temperature distribution at different instants of time. The case of a variable radius of the contact spot: (*1*) 6, (*2*) 5, (*3*) 4, (*4*) 3, (*5*) 2, and (*6*) 1 ms.
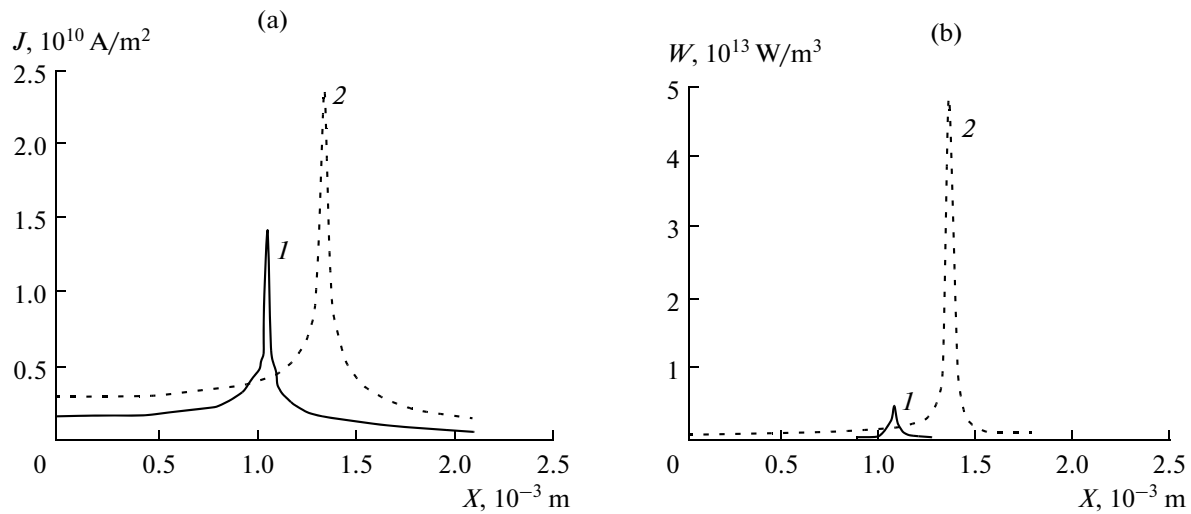
Fig. 10. Distributions of (a) the current density and (b) power at $t = 1$ and 6 ms. The case of a variable radius of the contact spot. t, ms: (*1*) 1 and (*2*) 6.
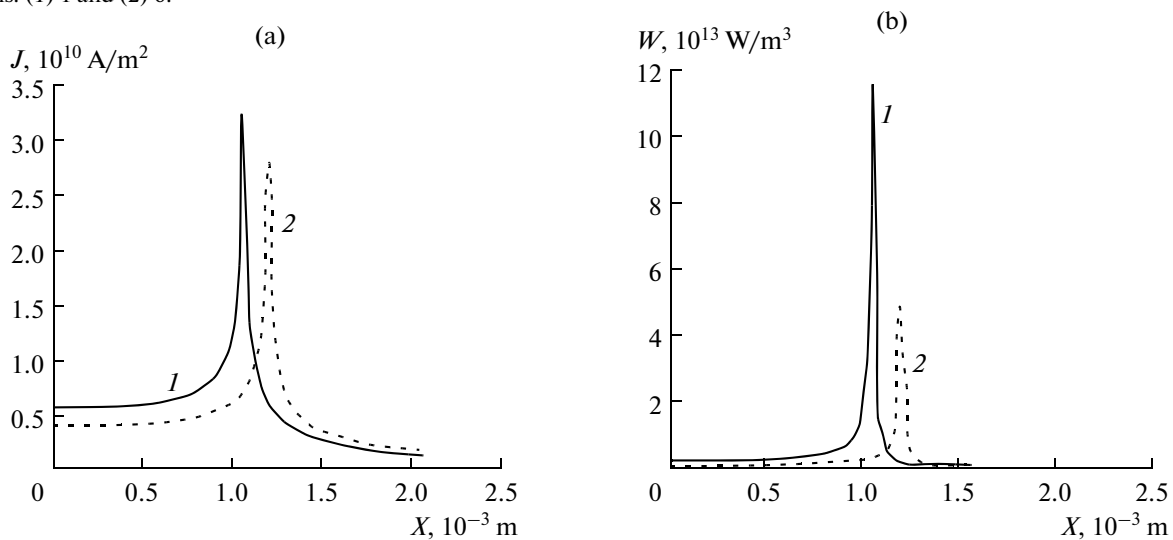
Fig. 11. Distributions of (a) the current density and (b) the power at the instant of 4.15 ms. The solid line corresponds to the case of a constant radius; the dashed line denotes the case of a variable radius: (*1*) $a = $ const and (*2*) $a = a(t)$.
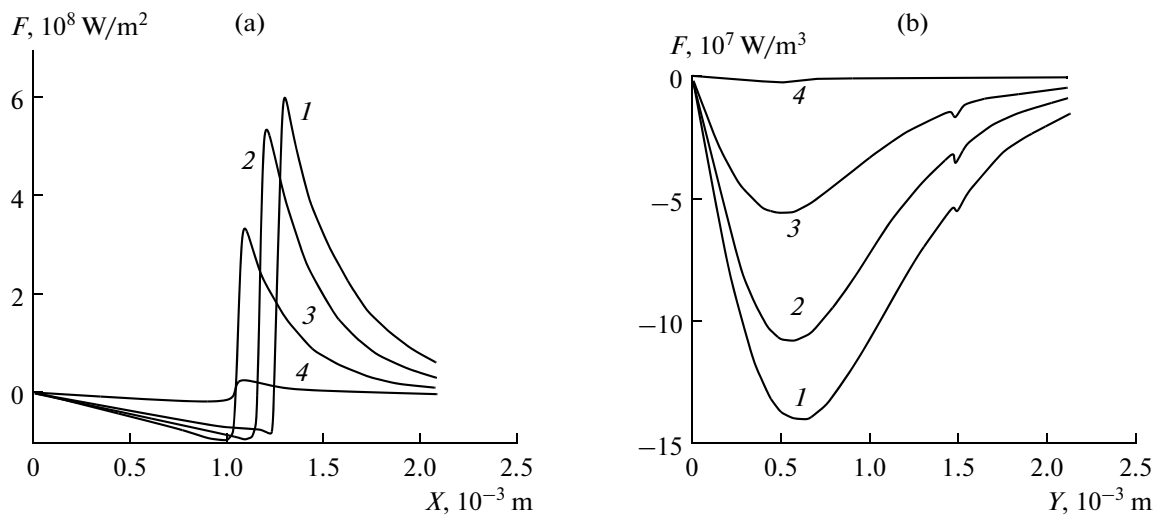
Fig. 12. Distributions of (a) the *X*-component and (b) *Y*-component of the heat flows at different instants of time: 1, 3, 4, and 5 ms. The case of a variable radius of the contact spot.
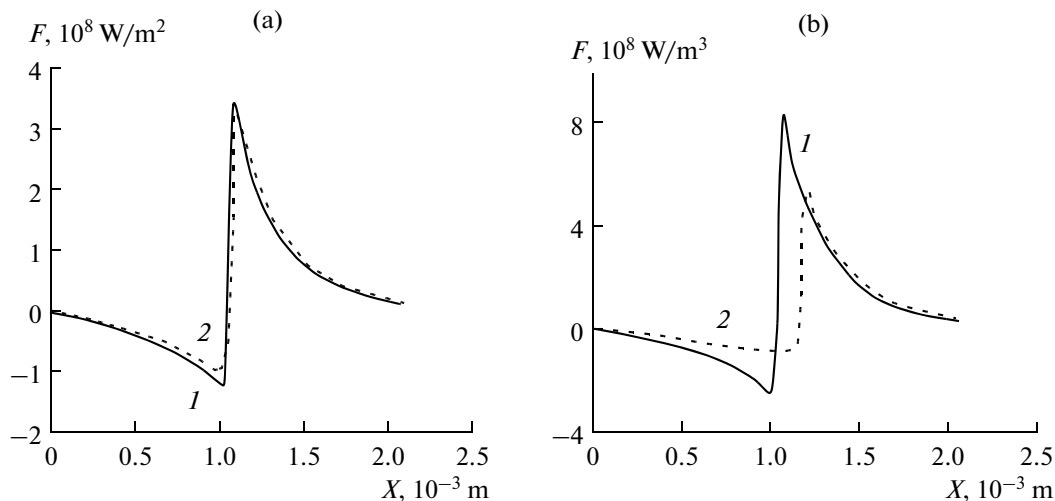
Fig. 13. Distribution of the *X*-component of the heat flow. The solid line corresponds to the case of a constant radius; the dashed line denotes the case of a variable radius: (a) $t = 3$ ms and (b) $t = 4$ ms.

of the heat flow along the $0X$ axis and the *Y*-component of the heat flow along the $0Y$ axis.

Compare the distributions of the *X*-component of the heat flow along the $0X$ axis for the cases of a constant and variable radius of the contact spot at different instants of time (Fig. 13). The solid line corresponds to the case of a constant radius; the dashed line denotes the case of a variable radius.

Before the achievement of the softening temperature of the material, the heat flows in the two cases almost coincide. After the radius of the contact spot begins to increase, the maximum values of the heat flow inward and outward the spot become lower in absolute magnitude than in the case of a constant radius. In addition, the relative magnitude of the heat

flow inward the spot, which leads to its heating, in the second case becomes lower than in the first. This leads to a significant slowdown in the heating of the spot during its spreading.

CONCLUSIONS

In this work, a numerical simulation of a pulsed heating of electrodes in a wide temperature range up to the melting point is performed. The calculation results showed that the effect of the increasing radius of the contact spot associated with the softening of the material has a significant effect on the dynamics of the heating. The regard for this effect leads to a considerable decrease in the maximum temperature in the

contact area. This is attributed to the fact that, during the spreading of the contact spot, the region of maximum heat evolution, which is highly localized, shifts after the boundary of the spot. The consequence is also the more uniform heating of the spot.

It is possible to carry out a numerical simulation of the current flow through electrical contacts in the approximation of a constant radius of the contact spot only in the case where the temperature of the contact area does not significantly exceed the softening temperature of the material.

REFERENCES

1. Holm, R., *Electrical Contacts Handbook*, Berlin: Springer, 1958.

2. Myshkin, N.K., Konchits, V.V., and Braunovich, M., *Elektricheskie kontakty* (Electrical Contacts), Moscow: Intellekt, 2008.

3. Chaly, A., Dmitriev, V., Pavleyno, M., and Pavleyno, O., Experimental Research and Computer Simulation Process of Pulse Heating High Current Contacts of Vacuum Interrupters, *Proc. 24th Int. Symp. on Discharges and Electrical Insulation in Vacuum*, Braunschweig, 2010, vol. 2, pp. 418−423.

4. Pavleino, O.M., Pavlov, V.A., and Pavleino, M.A., Verification of the Boundaries of the Applicability of the Holm Approximation for the Calculation of the Resistance of Electric Contacts, *Surf. Eng. Appl. Electrochem.*, 2010, vol. 46, no. 5, pp. 440−446.

5. Monnier, A., Froidurot, B., Jarrige, C., Meyer, R., and Teste, P., A Coupled-Field Simulation of an Electrical Contact during Resistance Welding, *Proc. 52nd IEEE Holm Conf. on Electrical Contacts*, 2006, pp. 95−102.

6. Monnier, A., Froidurot, B., Jarrige, C., Testé, P., and Meyer, R., A Mechanical, Electrical, Thermal Coupled-Field Simulation of a Sphere−Plane Electrical Contact, *Proc. 52nd IEEE Holm Conf. on Electrical Contacts*, 2006, pp. 787−795.

7. Abdi, El., Beloufa, R., and Benjemaâ, A.N., Contact Resistance Study of High-Copper Alloys Used in Power Automotive Connectors, *Proc. Inst. Mech. Eng., Part D: J. Automob. Eng.*, 2008, vol. 222, no. 8, pp. 1375−1383.

8. Pavleino, O.M., Pavleino, M.A., Pavlov, V.A., and Statuya, A.A., Numerical Simulation of the Pulsed Heating of Electrical Contacts, *Sbornik trudov IX Mezhdunarodnoi nauchnoi konferentsii "Sovremennye problemy elektrofiziki i elektrogidrodinamiki zhidkostei"* (Proc. IX Int. Sci. Conf. on Modern Problems of Electrophysics and Electrohydrodynamics of Fluids), St. Petersburg, 2009, pp. 292−297.

ELECTRICAL PROCESSES
IN ENGINEERING AND CHEMISTRY

Analysis of Electrostatic Ion-Cyclotron Instability Driven by Parallel Flow Velocity Shear[1]

R. K. Tyagi[a], K. K. Srivastava[a], and R. S. Pandey[b]

[a] *Department of Mechanical Engineering, Birla Institute of Technology Mesra Ranchi, Jharkhand, India*
[b] *Department of Applied Physics, Amity School of Engineering and Technology, Amity University Utter Pradesh, Noida, India*
e-mail: tyagi_rkl@rediffmail.com
Received September 2, 2010; in final form, March 14, 2011

Abstract—Analysis and study of parallel flow velocity shear and electrostatic ion cyclotron (EIC) instability performed in plasma containing massive positive ions and electron by using the method of characteristics solution and kinetic theory in the presence of homogeneous direct-current (DC) electric field perpendicular to ambient magnetic field. The calculation of growth rate and real frequency has been done by using the computational technique. The effect of many parameters like shear scale length, homogenous d.c.electric field, magnetic field, electron ion temperature ratio, angle between wave number $k_\perp$ and $k_\parallel$, on growth rate and also the effect of homogenous d.c.electric field, magnetic field on real frequency has been discussed by using the experimental data. Applications to possible laboratory plasmas and industries are also analyzed.

INTRODUCTION

In the recent past considerable attention has been given to the study of dynamics that governs the release of free energy associated with sheared flows in magnetohydrodynamics (MHD) and in plasma physics. Sheared flows are the dominant features found in space plasma. Simulation of ion-cyclotron mode in a magneto-plasma with transverse inhomogeneous electric field for a Maxwellian plasma suggested that electrostatic waves with the frequencies of the order of ion-cyclotron frequencies could be destabilized as a result of coupling of regions of positive and negative ion energy of waves [1−3]. A rigorous analytical treatment using MHD approach has established the existence of two modes (i) large wavelength Kelvin-Helmholtz (K-H) mode and (ii) shear wavelength ion-cyclotron mode.

In fusion plasma a sheared flow has been found to modify significantly the magneto-hydrodynamic equilibrium and ballooning stability of toroidal confinement devices [4, 5]. More importantly, shear driven turbulence can have a significant effect on particle, momentum and energy transport. Velocity shear has been recently identified as an important element in the transition from low confinement (L) to high confinement (H) mode in tokomak plasmas [6−9].

Parallel velocity shear (PVS) is a plasma configuration with ion flow parallel to the magnetic field, but with a velocity gradient transverse to B. PVS is commonly observed along the Earth's auroral field lines and in association with magnetic field-aligned current

may excites ion cyclotron instability. Ganguli et al. [10], using Ganguli et al. [1, 2] and Nishikawa et al. [3], Vlasov theory and particle-in-cell (PIC) simulation, have analyzed the effect of inhomogeneous parallel ion flow on the excitation of electrostatic ion cyclotron (EIC) waves in an attempt to understand in-situ observations of these waves in the presence of levels of field-aligned currents that were generally subcritical waveforms. They discovered that ion flow gradients could give rise to a new class of ion-cyclotron waves driven by "inverse cyclotron damping" even in the absence of field-aligned current.

Furthermore the ion flow gradient mechanism can drive the multiple cyclotron harmonics giving rise to "spiky" waveforms has been observed on FAST S/C [11]. Using an extension of the early work of D'Angelo [12] on shear driven (K-H) waves, Merlino [13] used a purely fluid treatment that also included a density gradient to show that the parallel velocity shear could excite EIC waves in plasma with no current.

In the result of a series of experiments, investigating the effect of a parallel velocity shear on ion-cyclotron waves, it has been demonstrated that PVS can be an important excitation mechanism of this plasma mode. It is important to note that in a Q-machine, EIC wave growth without shear has been observed in current free plasma when free energy due to parallel velocity shear was available. PVS is capable of generating a multiple EIC spectrum with high order harmonics having multitudes comparable to the fundamental. Electrostatic ion-cyclotron instability lead by magnetic field-aligned current was first observed in a narrows current channel (width < ion gyro-radius) in a Q-machine

---

[1] The article is published in the original.

[14]. Many of the characteristics of this instability that have been investigated experimentally were in agreement with the local theory of Drummond and Rosenbluth [15] appropriate to a uniform magnetized plasma, in which electron drift along B field lines with the same drift velocity at all points in plasma [16, 17]. The effect of a transverse gradient in the plasma flow velocity parallel to the magnetic field on the excitation of EIC waves has also been analyzed by Ganguli et al. [10]. They showed that ion flow gradients (parallel velocity shear) can give rise to a new class of ion cyclotron waves via inverse cyclotron damping, with a resulting spectrum of multiple cyclotron harmonics. The effect of parallel velocity shear on EIC wave excitation was studied experimentally by Agrimson et al. [18], who pointed out that the typical configuration used to study EIC wave production in the laboratory necessarily included the presence of parallel ion flow with transverse shear. These experiments provided clear evidence that parallel velocity shear does play a role in the excitation of EIC waves. Further observations of inverse ion-cyclotron damping induced by PVS have also been published by Teodorescu et al. [19].

Experimental results indicate that the presence of parallel velocity shear may lead to the excitation of the instability, even in narrow current filaments that would otherwise not sustain the instability [20]. The instabilities associated with velocity shear transitions separating plasmas moving in opposite directions have been considered [21]. From one semi-infinite plasma streaming with velocity $v < 0$ the transition can be of the so called ion dominated (ID) type where the confining current is only due to the ions and the typical width of the transition is of the order of a typical ion Larmor's radius. In this kind of transition the electrons are electrostatically confined. For $v > 0$ the transition can be of the so called electron dominated (ED) type where the confining current is only due to electrons while the ions are electrostatically confined. The ED transition has a typical width of the order of a mean electron Larmor's radius. It has been shown [22] that these two kinds of transition correspond to the two boundaries of a streaming finite plasma beam, one of the boundaries being of the ED type white the other boundary is of the ID type.

There has been considerable interest in recent years in studying the possibility of destabilizing space plasmas with velocity shears. There have, in particular been both direct and indirect evidence for sharp horizontal structures in field-aligned currents [23–26]. The two phenomena, intense bursts of field-aligned currents and large localized ion up flows have been shown to be on the edge of auroral arcs, where narrow but intense parallel current densities also exist.

Interest has also been created in the role played by horizontal shears in field-aligned flows in the excitation of plasma waves in ionospheric and magnetospheric plasmas. Earlier theoretical study suggested

and using of the fluid theory that in the presence of collisions, the horizontal shears in the field-aligned ion velocity could produce very low frequency modes in the frame of reference of moving F-region plasma at an angle very close to perpendicular to the magnetic field. Gavrishchaka et al. [27] concluded that the current driven electrostatic ion-cyclotron mode could be excited with parallel drifts significantly below the critical drift for homogenous EIC and also that infinitesimal shears could destabilize waves. Gavrishchaka et al. [28] explored the weak and strong shear limits of the earlier paper to conclude that for weak shears the minimum field-aligned currents were included much smaller than the critical currents for EIC instabilities. Within the fluid limit (requiring in particular that $T_c \gg T_i$), it was found that collisions and Larmor's radius corrections both acted to modify the threshold conditions in the regimes explored by Basu and Coppi [29] and Gavrishchaka et al. [27]. In particular, collisions usually meant that the plasma could no longer become unstable to infinitesimal shears, however, shears always introduced a new zero current mode for $\omega/k\alpha_s < 1$ (where α_s be the thermal velocity) for moderate shears.

In the case of parallel flow shear experiments performed in the Q-upgrade machine it is found that ion-cyclotron instability is originally excited by applying positive bias potentials to a small disc electrode adjusted at the centre of a magnetized plasma column. This instability is enhanced by shear and is suppressed by the larger shear. In the case of perpendicular flow shear experiments on the other hand the ion cyclotron instability is excited by the small disc electrode and suppressed by only the slight shear. The perpendicular shear is found to suppress both the current driven type and the potential driven type instabilities which can be excited by changing the bias voltage applied to the small disc electrode.

Three dimensional electrostatic particle simulations recently performed in order to investigate the effects of ion flow velocity shear, in detail have shown that the parallel velocity shear of the ion flow can excites these low frequency instabilities and the excited instabilities are localized at the velocity shear region. Parallel velocity shear is a plasma configuration with ion flow parallel to the magnetic field, but with a velocity gradient transverse to **B**. It is commonly observed along the Earth's auroral field lines and in association with magnetic field-aligned currents, may excite ion-cyclotron waves. In the present paper the effect of PVS on the excitation of electrostatic ion-cyclotron waves in plasma has been studied with and without field-aligned currents in laboratory conditions.

ANALYSIS

Spatially homogeneous anisotropic plasma subjected to an external magnetic field $\mathbf{B_0} = \mathbf{B_0}\hat{\mathbf{e}}_z$ and an inhomogeneous DC electric field $\mathbf{E_0(x)} = \mathbf{E_0(x)}\hat{\mathbf{e}}_x$ has

been considered. In order to obtain the dispersion relation, the Vlasov-Maxwell equations are linearized for inhomogeneous plasma by small perturbations of E_1, B_1 and f_{s1}. These are perturbed quantities and are assumed to have harmonic dependence as $\exp i(\mathbf{kr} - \omega t)$.

The linearized Vlasov equations obtained by separating the equilibrium and non equilibrium parts following the technique of Misra and Pandey [30] and Pandey et al. [31] in units of $c = 1$ (c is the speed of light) are given as:

$$v\frac{\partial f_{s0}}{\partial r} + \frac{e_s}{m_s}[E_0(x) + (v \times B_0)]\left(\frac{\partial f_{s0}}{\partial v}\right) = 0, \qquad (1)$$

$$\frac{\partial f_{s0}}{\partial t} + v\frac{\partial f_{s1}}{\partial r} + \left(\frac{F}{m_s}\right)\left(\frac{\partial f_{s1}}{\partial v}\right) = S(r, v, t), \qquad (2)$$

where the force is defined as $F = mdv/dt$.

$$F = e_s[E_0(x) + (v \times B_0)]. \qquad (3)$$

The particle trajectories are obtained by solving the equation of motion defined from Eq. (3) and $S(r, v, t)$ is defined as:

$$S(r, v, t) = \left(-\frac{e_s}{m_s}\right)[E_1 + v \times B_1]\left(\frac{\partial f_{s0}}{\partial v}\right). \qquad (4)$$

The method of characteristics solution is used to determine the perturbed distribution function f_{s1}. This is obtained from Eq. (2) by

$$f_{s1}(r, v, t) = \int_0^\infty S\{r_0(r, v, t'), v_0(r, v, t'), t - t'\}dt', \qquad (5)$$

where the index s denotes species.

We transformed the phase space co-ordinate system from (r, v, t') to $(r_0, v_0, t - t')$. The particle trajectories obtained by solving Eq. (3) for the given external field configuration by Misra and Tiwari [32] are given as:

$$x(t) = x_0 + \frac{v_\perp}{\Omega_s}\left(1 + \frac{\overline{E}(x)}{4\Omega_s^2}\right)[\sin(\theta - \Omega_s t) - \sin\theta],$$

$$y(t) = y_0 + \Delta + \frac{v_\perp}{\Omega_s}\left(1 + \frac{3}{4}\frac{\overline{E}(x)}{4\Omega_s^2}\right) \qquad (6)$$

$$\times [\sin(\theta - \Omega_s t) - \cos\theta],$$

$$z(t) = z_0 + v_\| t.$$

Here, θ is the angle between the vectors k and B_0. The values $E'(x)$, $E''(x)$ are the derivatives of $E(x) = E_{0x}(1 - x^2/a^2)$. Herewith:

$$\Delta = \frac{\overline{E}(x)t}{\Omega_s^2}\left[1 + \frac{E''(x)}{E(x)}\frac{1}{4}\left(\frac{v_\perp}{\Omega_s}\right)^2\ldots\ldots\ldots\right],$$

$$\overline{E}(x) = \frac{e_s E(x)}{m_s}, \quad \Omega_s = \frac{e_s B_0}{m_s}.$$

It should be noted that $\Delta' = \partial\Delta/\partial t$ represents the drift velocity. The value a is the scale length of electric field inhomogeneity. It is thought to be comparable to the mean ion gyro-radius, but larger than the Debye's length. When $x^2/a^2 < 1$, $E(x)$ becomes a constant uniform field.

After some lengthy algebraic simplifications following techniques out lined in Misra and Pandey [30] the time integration gives the perturbed distribution function as:

$$f_{s1}(r, v, t) = \frac{ie_s}{m_s\omega}\sum_{m, n, p, g} J_n(\lambda_1)J_m(\lambda_1)J_p(\lambda_2)J_g(\lambda_2)$$

$$\times e^{i(m-n)(\pi/2+\theta)}e^{i(g-p)(\pi/2+\theta)}$$

$$\times [E_{1x}U^* + V^*E_{1y} + W^*E_{1z}] \qquad (7)$$

$$\times \frac{1}{k_\| v_\| + n\Omega_s + p\Omega_s + k_\perp\Delta' - \omega},$$

where

$$U^* = Cv_\perp\frac{n}{\lambda_1} - Cv_\perp\frac{n}{\lambda_1}\frac{\overline{E}'(x)}{4\Omega_s^2}$$

$$+ k_\perp v_\perp\xi''\frac{n}{\lambda_1} + k_\perp v_\perp\xi''\frac{\overline{E}'(x)}{4\Omega_s^2}\frac{n}{\lambda_1},$$

$$V^* = iCv_\perp\frac{J_n'(\lambda_1)}{J_n(\lambda_1)} + \frac{3}{4}Cv_\perp\frac{\overline{E}'(x)n}{\Omega_s^2\lambda_1} - \Delta'C,$$

$$W^* = \omega\left(\frac{\partial f_{s0}}{\partial v_\|}\right) + Dk_\perp v_\perp\frac{n}{\lambda_1} + \frac{3Dk_\perp v_\perp}{4}\frac{\overline{E}'(x)}{\Omega_s^2}\frac{n}{\lambda_1},$$

$$C = (\omega - k_\| v_\|)\left(\frac{-2f_{s0}}{\alpha_{\perp s}^2}\right) + k_\|\frac{\partial f_{s0}}{\partial v_\|},$$

$$D = v_\|\left(\frac{2f_{s0}}{\alpha_{\perp s}^2}\right) - \frac{\partial f_{s0}}{\partial v_\|},$$

$$\lambda_1 = \frac{k_\perp v_\perp}{\Omega_s}, \quad \lambda_2 = \frac{3}{4}\frac{k_\perp v_\perp}{\Omega_s^2}\frac{\overline{E}'(x)}{\Omega_s^2},$$

$$J_n'(\lambda_1) = \frac{J_n(\lambda_1)}{d\lambda_1}.$$

Here, $J_n(\lambda_1)$ is the Bessel's function and the well-known Bessel identity $e^{i\lambda_1\sin\theta} = \sum_{n=-\infty}^{\infty} J_n(\lambda_1)e^{in\theta}$ is used.

The unperturbed bi-Maxwellian distribution function is written as:

$$f_{s0} = f_{sm0} + v_{0y}\xi'',$$

$$\xi'' = \frac{1}{\Omega_s}\left[\frac{2(v_\parallel - v_{0z}(x))}{\alpha_{\parallel s}^2}\frac{\delta v_{0z}(x)}{\delta x}\right]f_{sm0},$$

$$f_{m0}$$ (8)

$$= \frac{n_0(x)}{(\pi)^{1/2}\alpha_{\perp s}\alpha_{\parallel s}}\exp\left[-\frac{(v_{0x}^2 - v_{0y}^2)}{\alpha_{\perp s}^2} - \frac{(v_\parallel - v_{0z}(x))^2}{\alpha_{\parallel s}^2}\right].$$

Here, ξ'' is being the constant of motion and $n_0(x)$ is the plasma particle density.

$$\alpha_{\perp s} = \left(\frac{2k_B T_{\perp s}}{m_s}\right)^{1/2}, \quad \alpha_{\parallel s} = \left(\frac{2k_B T_{\parallel s}}{m_s}\right)^{1/2}.$$

Now simplifying $m = n$, $g = p$ and using the definitions of current density, conductivity and dielectric tensor, we get the dielectric tensor:

$$\|\varepsilon(k_1\omega)\| = 1 - \frac{4\pi e_s^2}{m_s\omega^2}$$ (9)

$$\times \int\frac{d^3v\sum J_p^2(\lambda_2)\|S_{ij}\|}{k_\parallel v_\parallel + n\Omega_s + p\Omega_s + k_\perp\Delta' - \omega},$$

where

$$\|S_{ij}\| = \begin{vmatrix} J_n^2 U^*\frac{n}{\lambda_1}v_\perp & J_n^2 V^*\frac{n}{\lambda_1}v_\perp & J_n^2 W^*\frac{n}{\lambda_1}v_\perp \\ -iJ_n J_n' U^* v_\perp & -iJ_n J_n' V^* v_\perp & -iJ_n J_n' W^* v_\perp \\ J_n^2 U^* v_\parallel & J_n^2 V^* v_\parallel & J_n^2 W^* v_\parallel \end{vmatrix}.$$

Now we consider the electrostatic ion-cyclotron instability.

$$\|\varepsilon_\parallel\| = N^2.$$ (10)

Here, N is the refractive index.

The required electrostatic dispersion relation can be obtained by using the approximation of Huba [33] and from Eqs. (8)−(10).

$$D(k, \omega) = 1 + \frac{2\omega_{ps}^2}{k_\perp^2\alpha_{\perp s}^2}\Gamma_n(\mu_s)$$

$$\times\sum J_P^2(\lambda_2)\left[1 - \frac{E'(x)}{4\Omega_s^2}\right]\frac{k_\perp}{k_\parallel}$$ (11)

$$\left[\left(\frac{\bar{\omega}}{k_\parallel\alpha_{\parallel s}} - \frac{1}{2}\varepsilon_n\rho_s\frac{\alpha_{\perp s}}{\alpha_{\parallel s}}\right)Z(\xi) - A_s\frac{\alpha_{\perp s}^2}{\alpha_{\parallel s}^2}(1 + \xi Z(\xi))\right.$$

$$\left. + A_T\frac{k_\parallel}{k_\perp}(1 + \xi Z(\xi))\right],$$

where

$$\xi = \frac{\bar{\omega} - (n+p)\Omega_s - k_\perp\Delta'}{k_\parallel\alpha_{\parallel s}},$$

$$A_s = \frac{1}{\Omega_s}\frac{\delta v_{0z}(x)}{\delta x}, \quad \varepsilon_n = \frac{\delta\ln n_0(x)}{\delta x},$$

$$A_T = \frac{\alpha_{\perp s}^2}{\alpha_{\parallel s}^2} - 1, \quad \bar{\omega} = \omega - k_\perp v_{0z}(x), \quad \lambda_{Ds}^2 = \frac{\alpha_{\perp s}^2}{2\omega_{ps}^2},$$

$$\Gamma_n(\mu_s) = \exp(-\mu_s)I_n(\mu_s), \quad \mu_s = \frac{k_\perp^2\rho_i^2}{2}.$$

Here, $Z(\xi)$ is the plasma dispersion function [34], ω_{ps}^2 is the plasma frequency and $I_n(s)$ is the modified Bessel's function of order n.

Above dispersion relation reduces to that of Huba [33] if inhomogeneous DC electric field is removed and further using $\alpha_{\perp s} = \alpha_{\parallel s}$ and following of the assumptions of Pandey et al. [35], in order to get the dispersion relation for electrons and ions ($s = i, e$) the approximation for electrons are assumed as $k_\perp\rho_e \ll 1$ and for ions no such assumption is done. Thus, above equation becomes:

$$D(k, \omega) = 1 + \frac{1}{k_\perp^2\lambda_{De}^2}\eta_e\frac{T_{\perp e}}{T_{\parallel e}} + \frac{1}{k_\perp^2\lambda_{Di}^2}\eta_i$$

$$\times\left[\frac{T_{\perp i}}{T_{\parallel i}}\Gamma_n(\mu_i)\frac{k_\perp}{k_\parallel}\left[\left(\frac{\bar{\omega}}{k\alpha_{\parallel i}}\times\frac{T_{\perp i}}{T_{\parallel i}} - \frac{1}{2}\varepsilon_n\rho_s\frac{\alpha_{\perp i}}{\alpha_{\parallel i}}\right.\right.\right.$$

$$\left.\left.+ \frac{n\Omega_i + k_\perp\Delta'}{k_\parallel\alpha_{\parallel i}}\left(1 - \frac{T_{\perp i}}{T_{\parallel i}}\right)\right)Z(\xi_i)$$ (12)

$$\left.\left. - A_i\frac{T_{\perp i}}{T_{\parallel i}}(1 + \xi Z(\xi_i))\right]\right].$$

Substitution of the asymptotic expansion of $Z(\xi_i) = -1/\xi_i - 1/2\xi_i^3$ for ions, $|\xi_i| \ll 1$ [34] and $n_{0i} = n_{0e}$ with further multiplying throughout by $k_\perp^2\lambda_{Di}^2/\eta_i$ leads to:

$$0 = \frac{\lambda_{Di}^2}{\lambda_{De}^2}\frac{\eta_e}{\eta_i}\frac{T_{\perp e}}{T_{\parallel e}} + \frac{T_{\perp i}}{T_{\parallel i}} - \Gamma_n(\mu_i)\frac{T_{\perp i}}{T_{\parallel i}} + \frac{\Gamma_n(\mu_i)k_\perp}{2k_\parallel}$$

$$\times\varepsilon_n\rho_i\frac{\alpha_{\perp s}}{\alpha_{\parallel s}}\frac{k_\parallel\alpha_{\parallel i}}{\bar{\omega} - n\Omega_i - k_\perp\Delta'} - \frac{\Gamma_n(\mu_i)k_\perp}{k_\parallel}$$

$$\times\frac{n\Omega_i + k_\parallel\alpha_{\parallel i}}{\bar{\omega} - n\Omega_i - k_\perp\Delta'} - \frac{\Gamma_n(\mu_i)k_\perp}{2(\bar{\omega} - n\Omega_i - k_\perp\Delta')^2}$$ (13)

$$\times\frac{T_{\perp i}}{T_{\parallel i}}(k_\parallel\alpha_{\parallel i})^2\left(1 - \frac{k_\perp}{k_\parallel}A_i\right),$$

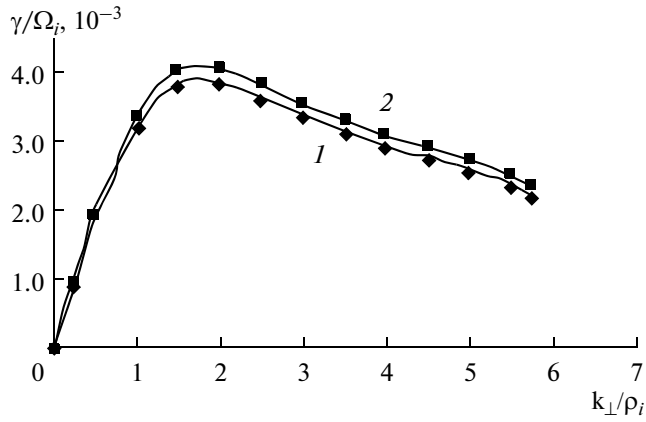**Fig. 1.** Variation of growth rate γ/Ω_i versus $k_\perp\rho_i$ for different values of A_i and other parameters are $B_0 = 0.24$ T, $T_e/T_i = 2$, $E_0 = 8$ V/m, $\theta = 88.5°$, $A_T = 1.5$, $\varepsilon_n\rho_i = 0.2$, $1—A_i = 0.5$; $2—A_i = 0.55$.
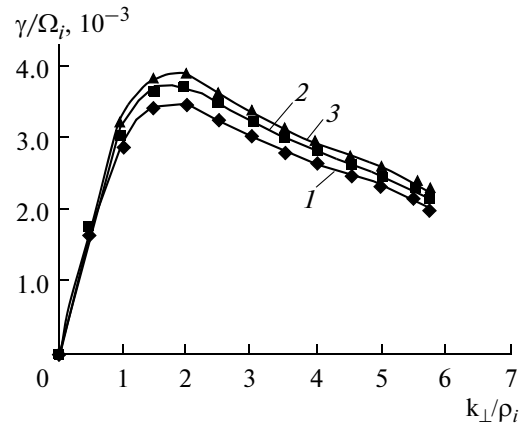

Fig. 2. Variation of growth rate γ/Ω_i versus $k_\perp\rho_i$ for different values of T_e/T_i and other parameters are $A_i = 0.5$, $B_0 = 0.24$ T, $E_0 = 8$ V/m, $\theta = 88.5°$, $A_T = 1.5$, $k_\perp\rho_i = 0.2$, $1—T_e/T_i = 2$; $2—T_e/T_i = 3$; $3—T_e/T_i = 4$.

where

$$\eta_i = 1 - \frac{\overline{E}'_i(x)}{4\Omega_i^2}, \quad \eta_e = 1 - \frac{\overline{E}'_e(x)}{4\Omega_e^2}.$$

Multiplying Eq. (13) throughout by $(\overline{\omega} - n\Omega_i - k_\perp\Delta'/k_\parallel\alpha_{\parallel i})^2$, we obtain a quadratic equation as:

$$a_1\left(\frac{\overline{\omega}'}{\Omega_i}\right)^2 + b_1\left(\frac{\overline{\omega}'}{\Omega_i}\right) + c_1 = 0, \tag{14}$$

where

$$a_1 = a_2\left(\frac{\Omega_i}{k_\parallel\alpha_\parallel}\right)^2, \quad a_2 = \frac{\eta_e}{\eta_i}\frac{T_{\perp i}}{T_{\parallel i}} + \frac{T_{\perp i}}{T_{\parallel i}} - \Gamma_n(\mu_i)\frac{T_{\perp i}}{T_{\parallel i}},$$

$$b_1 = \frac{\Omega_i}{k_\parallel\alpha_{\parallel i}}b_2 - \frac{2k_\perp\Delta'}{k_\parallel^2\alpha_{\parallel i}^2}a_2\Omega_i,$$

$$b_2 = \frac{\Gamma_n(\mu_i)k_\perp}{2k_\parallel}\varepsilon_n\rho_i\frac{\alpha_{\perp i}}{\alpha_{\parallel i}} - \frac{\Gamma_n(\mu_i)k_\perp}{2k_\parallel} - \frac{\Gamma_n(\mu_i)k_\perp n\Omega_i}{2k_\parallel^2\alpha_{\parallel i}},$$

$$c_1 = \frac{\Gamma_n(\mu_i)T_{\perp i}}{2T_{\parallel i}}\left(1 - \frac{k_\perp}{k_\parallel}A_i\right) - \frac{b_2k_\perp\Delta'}{k_\parallel\alpha_{\parallel i}} + \frac{k_\perp^2\Delta'^2}{k_\parallel^2\alpha_{\parallel i}^2},$$

$$\overline{\omega}_i = \overline{\omega} - n\Omega_i.$$

The solution of Eq. (14) is:

$$\frac{\overline{\omega}'}{\Omega_i} = -\frac{b_1}{2a_1}\left[1 \pm \sqrt{\left(1 - \frac{4a_1c_1}{b_1^2}\right)}\right]. \tag{15}$$

From this expression the dimensionless growth rate has been calculated by computer technique when $b_1^2 < 4a_1c_1$ and also the dimensionless real frequency has been calculated from above expression. Hence, this criterion gives a condition for the growth rate of wave with homogeneous DC electric field considering inhomo-

geneity in electric field is neglected. It means we have discussed the case of homogeneous DC electric field.

RESULTS AND DISCUSSION

In this section, we show the solution of the Eq. (15) for $x^2/a^2 < 1$ using parameters like a magnetic field, density gradient, thermal velocities and etc. which were representative of laboratory by Kim and Merlino [16] and Rosenberg, Merlino [17]. We consider plasma in which the heavy positive ions are produced due to ionization of K^+ and light electron are produced from SF_6^-. It is assumed that electron and ion temperature ratio T_e/T_i is varying between 2 to 4. It is further assumed that the plasma is immersed in a magnetic field whose strengths are varying from 0.24 to 0.32 T and homogeneous DC electric field strength from 4 to 12 V/m which is perpendicular to magnetic field. In this case the positive ions gyro-radius $\rho \sim 0.095$ cm having a temperature anisotropy $A_T = T_{\perp i}/T_{\parallel i} - 1$ varying from 0.5 to 1.5 with density gradient $\varepsilon_n\rho_i = 0.2$ has been considered. In this case we would expect that the electrostatic ion cyclotron instability could become excited by parallel velocity shear with scale length A_i varying from 0.5 to 0.55.

In Fig. 1 the variation of growth rate γ/Ω_i versus $k_\perp\rho_i$ for different values of velocity shear scale length A_i has been shown for other fixed plasma parameters. The growth rate increases with increasing value of shear scale length A_i and the bandwidth slightly increases with A_i but the maxima of band does not shift. The maximum peak value of growth rate is 4.05×10^{-3} at $k_\perp\rho_i = 2$, $A_i = 0.55$. The mechanism for instability of this mode is due to coupling of regions of positive and negative wave energy. This coupling occurs if velocity shear is non-uniform and hence velocity shear is the source of instability.

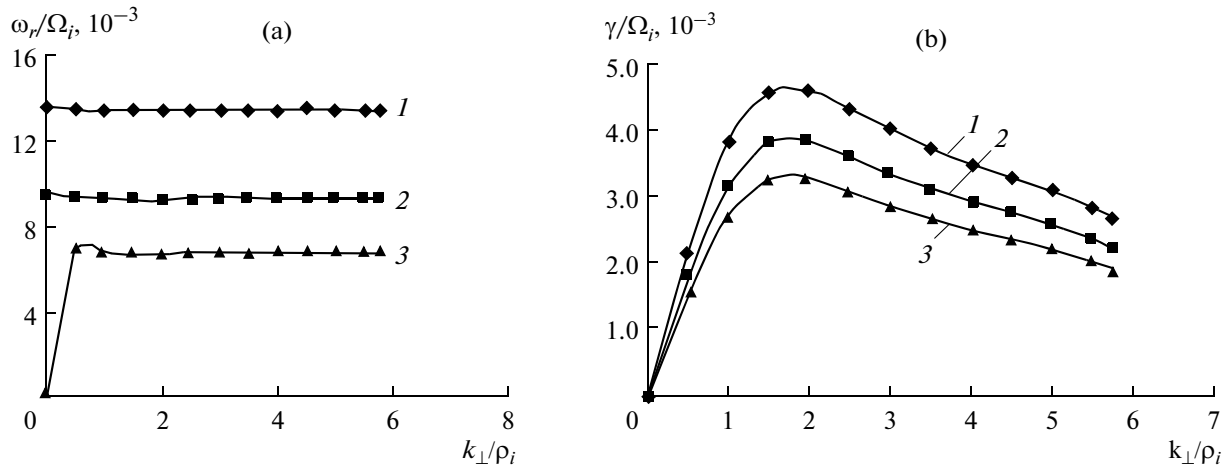Figure 2 shows the variation of growth rate γ/Ω_i versus $k_\perp\rho_i$ for various values of electron ion tempera-

Fig. 3. (a) Variation of real frequency ω_r/Ω_i versus $k_\perp\rho_i$ for different values of B_0 and other parameters are $A_i = 0.5$, $T_e/T_i = 2$, $E_0 = 8$ V/m, $\theta = 88.5°$, $A_T = 1.5$, $\varepsilon_n\rho_i = 0.2$, $1—B_0 = 0.2$ T; $2—B_0 = 0.24$ T; $3—0.28$ T. **(b)** Variation of growth rate γ/Ω_i versus $k_\perp\rho_i$ for different values of B_0 and other parameters are $A_i = 0.5$, $T_e/T_i = 2$, $E_0 = 8$ V/m, $\theta = 88.5°$, $A_T = 1.5$, $\varepsilon_n\rho_i = 0.2$. $1—B_0 = 0.2$ T; $2—B_0 = 0.24$ T; $3—B_0 = 0.28$ T.
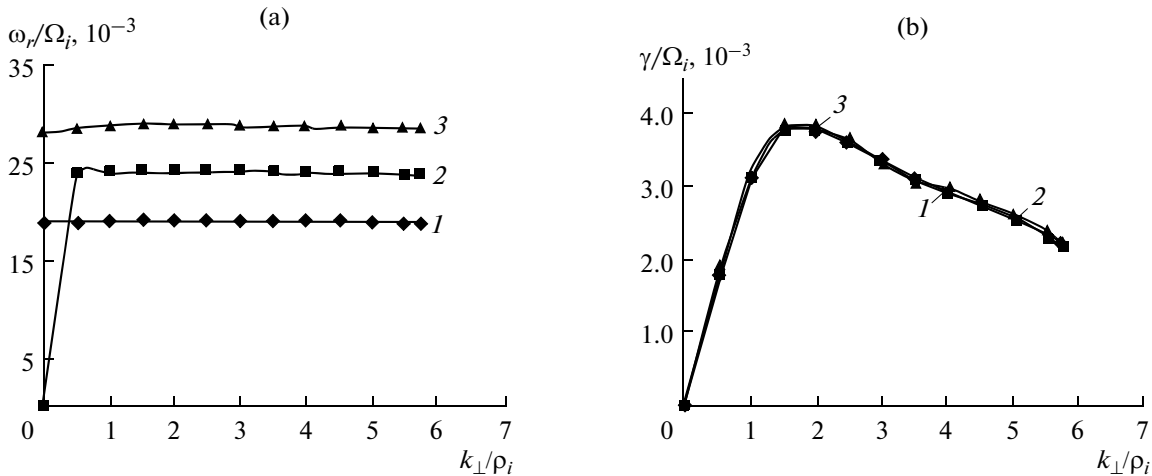

Fig. 4. (a) Variation of real frequency ω_r/Ω_i versus $k_\perp\rho_i$ for different values of E_0 and other parameters are $A_i = 0.5$, $B_0 = 0.24$ T, $T_e/T_i = 2$, $\theta = 88.5°$, $A_T = 1.5$, $\varepsilon_n\rho_i = 0.2$, $1—E_0 = 16$ V/m; $2—E_0 = 20$ V/m; $3—E_0 = 24$ V/m. **(b)** Variation of growth rate γ/Ω_i versus $k_\perp\rho_i$ for different values of E_0 and other parameters are $A_i = 0.5$, $B_0 = 0.24$ T, $T_e/T_i = 2$, $\theta = 88.5°$, $A_T = 1.5$, $\varepsilon_n\rho_i = 0.2$, $1—E_0 = 16$ V/m; $2—E_0 = 20$ V/m; $3—E_0 = 24$ V/m.

ture ratio T_e/T_i, on this figure the growth rate increases by increasing the values of electron ion temperature ratio because due to inhomogeneity in electron ion temperature that depends on the applied voltage of electrodes. The maximum peak values of growth rate is 3.85×10^{-3} at the $k_\perp\rho_i = 2$ with homogeneous DC electric field, as velocity shear term is proportional to electron ion temperature ratio T_e/T_i.

Figures 3a and 3b show the variation of real frequency ω_r/Ω_i (ω_r is a real frequency) and growth rate γ/Ω_i versus $k_\perp\rho_i$ for different values of magnetic field strength B_0 with other fixed parameters listed in figure caption. The growth rate and real frequency decrease

with increasing the magnetic field strength. Due to change in magnetic field gyro-frequency has been changed. The homogeneous magnetic field couples positive and negative energy waves thus changes the growth rate of the wave. The magnetic field strength is a useful parameter for required velocity of EIC wave. Hence, this is useful result for designing a machine for cold spray and metal cutting operations.

Figures 4a and 4b shows the variation of real frequency ω_r/Ω_i and growth rate γ/Ω_i versus $k_\perp\rho_i$ for various values of homogeneous DC electric field. The growth rate deceases with increasing of the value of homogeneous DC electric field from 4 to 12 V/m. But the real frequency increases with increasing the value
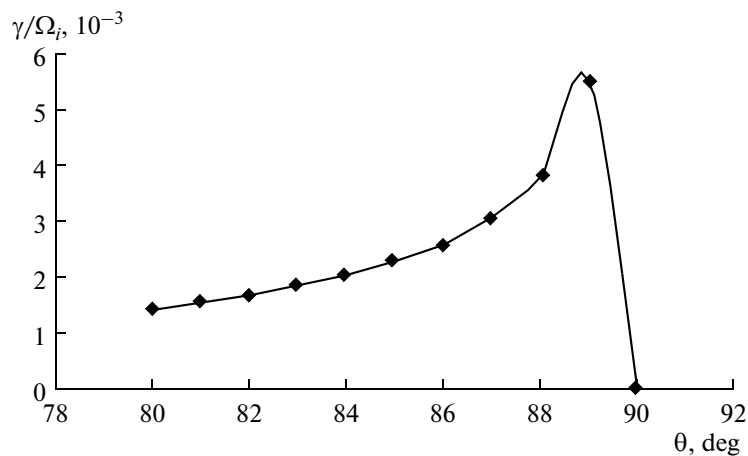
Fig. 5. Variation of growth rate γ/Ω_i versus θ for parameters like $k_\perp\rho_i = 2$, $A_i = 0.5$, $B_0 = 0.24$ T, $T_e/T_i = 2$, $E_0 = 8$ V/m, $A_T = 1.5$, $\varepsilon_n\rho_i = 0.2$.

of electric field. In general, this has a stabilizing effect introducing to the resonant and non-resonant interactions affecting on the growth rate and real frequency. This result will be helpful for designing the machine like a cold spray and metal cutting to control the frequency and velocity of the wave. The velocity of EIC wave is 1011 m/s for the value of homogeneous DC electric field 8 V/m and it is 2527 m/s for 20 V/m with other fixed parameters listed in figure caption.

Figure 5 shows the variation of growth rate versus angle between wave number $k_\perp$ and $k_\parallel$ like θ with parameter listed in figure caption. The maximum growth rate obtained for $\theta = 88.5°$. The parameters like a density gradient $\varepsilon_n\rho_i$ and temperature anisotropy $A_T = T_{\perp i}/T_{\parallel i} - 1$ have less effect on growth rate but the growth rate increases slightly with increasing the values of $\varepsilon_n\rho_i$ and A_T.

CONCLUSIONS

In this paper the effect of magnetic field, electric field, electron ion temperature ratio, temperature anisotropy of ions, shear scale length and density gradient on the growth rate and real frequency have been discussed separately. This result is useful for designing machine for cold spray & metal cutting operations with help of required velocity of generated and excited EIC wave.

ACKNOWLEDGMENTS

REFERENCES

1. Ganguli, G., Lee, Y.C., and Palmadesso, P., Electrostatic Ion-Cyclotron Instability Caused by a Nonuniform Electric Field Perpendicular to the External Magnetic Field, *Phys. Fluids*, 1985, vol. 28, no. 3, pp. 761–763.

2. Ganguli, G., Lee, Y.C., and Palmadesso, P.J., Kinetic Theory of Electrostatic Waves Due to Transverse Velocity Shears, *Phys. Fluids*, 1988, vol. 31, no. 4, pp. 823–838.

3. Nishikawa, K.-I., Ganguli, G., Lee, Y.C., and Palmadesso, P.J., Simulation of Ion-Cyclotron-Like Modes in a Magnetoplasma with Transverse Inhomogeneous Electric Field, *Phys. Fluids*, 1988, vol. 31, no. 6, pp. 1568–1576.

4. Waelbroeck, F.L. and Chen, L., Ballooning Instabilities in Tokamaks with Sheared Toroidal Flows, *Phys. Fluids, Ser. B,* 1991, vol. 3, no. 3, pp. 601–610.

5. Maslowe, S.A., Shear Flow Instabilities and Transition, in *Hydrodynamic Instabilities and the Transition to Turbulence*, Swinney, H.L. and Gollub, J.P., Berlin: Spinger-Verlag, 1985, ch. 7, pp. 181–228.

6. Bhattacharjee, A., Iacono, R., Milovich, J.L., and Paranicas, C., Ballooning Stability of Axisymmetric Plasmas with Sheared Equilibrium Flows, *Phys. Fluids, Ser. B*, 1989, vol. 1, no. 11, pp. 2207–2212.

7. Biglari, H., Diamond, P.H., and Terry, P.W., Influence of Sheared Poloidal Rotation on Edge Turbulence, *Phys. Fluids, Ser. B*, 1990, vol. 2, no. 1, pp. 1–4.

8. Shaing, K.C. and Crume, E.C., Jr., Bifurcation Theory of Poloidal Rotation in Tokamaks: A Model for *L-H* Transition, *Phys. Rev. Lett.*, 1989, vol. 63, no. 21, pp. 2369–2372.

9. Groebner, R.J., Burrell, K.H., and Seraydarian, R.P., Role of Edge Electric Field and Poloidal Rotation in the *L-H* Transition, *Phys. Rev. Lett.*, 1990, vol. 64, no. 25, pp. 3015–3018.

10. Ganguli, G., Slinker, S., Gavrishchaka, V., and Scales, W., Low Frequency Oscillations in a Plasma with Spatially Variable Field-Aligned Flow, *Phys. Plasmas*, 2002, vol. 9, no. 5, pp. 2321–2329.

11. Merlino, R.L., Agrimson, E.P., Kim, S.-H., D'Angelo, N., and Ganguli, G.I., Laboratory Studies of the Effect of Parallel Velocity Shear on Electrostatic Ion Waves in Magnetized Plasma, *Proceeding of XXIX General*

Assembly of Union Radio Scientifique Internationale, Chicago, USA, 2008, H05.1, p. 170 (4 pages).

12. D'Angelo, N., Kelvin-Helmholtz Instability in a Fully Ionized Plasma in a Magnetic Field, *Phys. Fluids*, 1965, vol. 8, no. 9, pp. 1748−1750.

13. Merlino, R.L., Electrostatic Ion-Cyclotron Waves Driven by Parallel Velocity Shear, *Phys. Plasmas*, 2002, vol. 9, no. 5, pp. 1824−1825.

14. D'Angelo, N. and Motley, R.W., Electrostatic Oscillations Near the Ion-Cyclotron Frequency, *Phys. Fluids*, 1962, vol. 5, no. 5, pp. 633−634.

15. Drummond, W.E. and Rosenbluth, M.N., Anomalous Diffusion Arising from Microinstabilities in a plasma, *Phys. Fluids*, 1962, vol. 5, no. 12, pp. 1507−1513.

16. Kim, S.-H. and Merlino, R.L., Electron Attachment to C_7F_{14} and SFe in a Thermally Ionized Potassium Plasma, *Phys. Rev., Ser. E*, 2007, vol. 76, no. 3, 035401(R).

17. Rosenberg, M. and Merlino, R.L., Instability of Higher Harmonic Electrostatic Ion Cyclotron Waves in a Negative Ion Plasma, *J. Plasma Phys.*, 2009, vol. 75, no. 4, pp. 495−508.

18. Agrimson, E.P., D'Angelo, N., and Merlino, R.L., Effect of Parallel Velocity Shear on the Excitation of Electrostatic Ion Cyclotron Waves, *Phys. Lett., Ser. A*, 2002, vol. 293, no. 5-6, pp. 260−265.

19. Teodorescu, C., Reynolds, E.W., and Koepke, M.E., Observation of Inverse Ion-Cyclotron Damping Induced by Parallel Velocity Shear, *Phys. Rev. Lett.*, 2002, vol. 89, no. 10, p. 105001.

20. Agrimson, E., Kim, S.-H., D'Angelo, N., and Merlino, R.L., Effect of Parallel Velocity Shear on the Electron Static Ion-Cyclotron Instability in Filamentary Current, *Phys. Plasmas*, 2003, vol. 10, no. 10, pp. 3850−3852.

21. Akerstedt, H.O., Velocity Shear Instabilition Associated with Plasma Motion Across a Magnetic Field, *Phys. Scripta*, 1984, vol. 29, no. 1, pp. 75−86.

22. Akerstedt, H.O. The Motion of a Finite Plasma Slab Across a Transverse Magnetic Field, *Phys. Scripta*, 1981, vol. 24, no. 4, pp. 775−784.

23. Noël, J.-M.A., Small-Scale Electrodynamics in the Auroral Ionosphere, *Ph.D. Dis.*, The University of Western Ontario, 1999.

24. Noël, J.-M.A., St.-Maurice, J.-P., and Blelly, P.-L., Nonlinear Model of Short-Scale Electrodynamics in the Auroral Ionosphere, *Ann. Geophys.*, 2000, vol. 18, no. 9, pp. 1128−1144.

25. Noël, J.-M.A., St.-Maurice, J.-P., and Blelly, P.-L., The Effect of *E*-Region Wave Heating on Electrodynamical Structures, *Ann. Geophys.,* 2005, vol. 23, no. 6, pp. 2081−2094.

26. Rother, M., Schlegel, K. and Lühr, H., CHAMP Observation of Intense Kilometer-Scale Field-Aligned Currents, Evidence for an Ionospheric Alfvén Resonator, *Ann. Geophys.*, 2007, vol. 25, no. 7, pp. 1603−1615.

27. Gavrishchaka, V.V., Ganguli, S.B., and Ganguli, G.I., Origin of Low-Frequency Oscillations in the Ionosphere, *Phys. Rev. Lett.*, 1998, vol. 80, no. 4, pp. 728−731.

28. Gavrishchaka, V.V., Ganguli, S.B., and Ganguli, G.I., Electrostatic Oscillations Due to Filamentary Structures in the Magnetic Field-Aligned Flow: The Ion-Acoustic Branch, *J. Geophys. Res.*, 1999, vol. 104, no. A6, pp. 12683−12693.

29. Basu, B. and Coppi, B., Velocity Shear and Fluctuations in the Auroral Regions of the Ionosphere, *J. Geophys. Res.*, 1989, vol. 94, no. A5, pp. 5316−5326.

30. Misra, K.D. and Pandey, R.S., Generation of Whistler Emissions by Injection of Hot Electrons in the Presence of a Perpendicular AC Electric Field, *J. Geophys. Res.*, 1995, vol. 100, no. A10, pp. 19405−19411.

31. Pandey, R.S., Misra, K.D., and Tripathi, A.K., Kelvin-Helmholtz Instability in an Anisotropic Magneto-Plasma in the Presence of Inhomogeneous Perpendicular Electric Field and Parallel Flow Velocity Shear, *Ind. J. Radio Space Phys.*, 2001, vol. 30, pp. 113−120.

32. Misra, K.D. and Tiwari, M.S., Particle Aspect Analysis of $E \times B$ Drift Instability in the Presence of Nonuniform Electric Field, *Phys. Scripta*, 1977, vol. 16, no. 3-4, pp. 142−146.

33. Huba, J.D., The Kelvin-Helmholtz Instability in Inhomogeneous Plasmas, *J. Geophys. Res.*, 1981, vol. 86, no. A5, pp. 3653−3656.

34. Fried, B.D. and Conte, S.D., *The Plasma Dispersion Function*, New York: Academic Press, 1961.

35. Pandey, R.S., Misra, K.D., and Tripathi, A.K., Generation of Ion-Cyclotron Wave by Parallel Flow Velocity Shear in the Presence of Inhomogeneous Electric Field in an Anisotropic Magneto-Plasma, *Ind. J. Radio Space Phys.*, 2003, vol. 32, pp. 75−82.

ELECTRICAL TREATMENT
OF BIOLOGICAL OBJECTS AND FOOD PRODUCTS

The Distant Effect of Water on Seeds Outside a Closed Reservoir

S. N. Maslobrod

Institute of Plant Genetics and Physiology, Academy of Sciences of Moldova,
ul. Pedurii 20, Kishinev, MD-202 Republic of Moldova
e-mail: maslobrod37@mail.ru
Received December 20, 2010

Abstract—By means of a biological detector (seeds of plants), we were the first to reveal the field outside a closed reservoir (a Petri cup) filled with water. The seeds (triticale and wheat) were placed above the closed reservoir with water for 24 and 72 hours and then were allowed to sprout. As a result, the energy of the seed germination and the number of right sprouts from the seeds increased. Different types of water (spring, tap, thawed, boiled, and water subjected to pretreatment by millimeter radiation) were used to determine the direct dependence of the effect on the structural (informative) state of the water. An electromagnetic screen was shown not to shield the field of water.

DOI: 10.3103/S1068375511040090

Water, which has been considered until recently to be an elementary chemical compound playing the role of a universal solvent, turns out to be inexhaustible from the point of view of its form and content [1, 2]. Even chemically pure water is a complex system consisting of a large number of particles with different isotope compositions, molecular masses, charges, and structures of the elements linked by mobile equilibriums sensitive to variations in the medium's parameters. It is a system possessing memory, i.e., the inhereditability of the properties of previous states [1—8]. According to Zenin, the results of the detailed investigation of a sequence of elementary acts in water turned out to be stunning: the water appeared before the researches as a strictly ordered completely determinate system rather than a chaotic cluster of molecules [1, 2].

The idea about water molecules as basic elements of the aquatic environment had to be substituted by the real pattern of the existing stable structural elements (water "quanta") consisting of a large number of molecules. In the brilliant theoretical and experimental works of Zenin, it was demonstrated that there are several informative levels in water that consist of stable structural elements with different sizes with them being a result and a consequence of the state of the electromagnetic water field [1, 2].

Direct proof of its existence has been obtained recently in [9, 10]. The so-called autooptical effect, i.e., variations in the optical density of samples during their exposure under mirror surfaces was revealed in water and blood preparation tests. Distilled and drinking water were used as test samples. The authors reached the conclusion that the mirrors form an optical resonator ensuring the mutual effect of the objects in it due to the generation of standing waves corresponding to the resonant frequencies of the system.

The water field reflected at the mirror is biologically active: if a palm is placed under it, functional systems of the human organism start reacting and it is possible to register this reaction based on cardiorythmograms or with the help of the Foll method [2].

In our experiment, an attempt was made to detect the water field based on its biological action on plants, namely, the influence on seed germination. In this case, the water field outside a closed reservoir (a Petri cup) filled with water was analyzed rather than the field reflected at the mirror and evidently making up only a part of the total water field.

TECHNIQUE

Seeds of winter triticale (Ingen-93) and winter wheat (N335) were used. The experiments were performed in a factorostatic chamber at a temperature of 22°C. The seeds were placed into reference and test Petri cups with 50 pieces in each. The version included three—four cups. It all the experiments, each test cup with the dry and wetted (for 24 h) seeds was placed on a closed cup filled with water (the technique of positioning the cups with the seeds under the cups with the water gave the same results). Water with different physical-chemical properties and structural states was used [11] (in this study, the preliminary estimation of these water properties was not made): (1) tap water (TW) and spring water (SW); (2) ordinary tap water (TW), boiled water (BW), and thawed water (ThW); (3) tap water (TW) and distilled water (DW); (4) ordinary tap water (TW) and the water treated with millimeter radiation (MMR) with a wavelength of 5.6 mm and a power density of 6 mW/cm^2, and exposures of 8 and 30 min (TW + MMW 8 min; TW + MMW 30 min); and (5) ordinary tap water (TW), boiled

Table 1. Germination energy and germination capacity of triticale seeds at the distant 24 and 72 h long action of tap and spring water on dry seeds, %

No.	Versions	Germination energy	Germination capacity
1	Germination in TW (reference sample 1)	77.0 ±2.51	88.0 ± 2.00
2	Germination in TW (reference sample 2)	79.3 ± 2.42	88.7 ± 2.35
3	Distant action of TW for 24 h, germination in TW	80.0 ± 0.00	96.0 ±3.51
4	Distant action of TW for 72 h, germination in TW	78.0 ±1.34	84.7 ±4.04
5	Germination in TW (reference sample 3)	92.0 ± 2.67	92.0 ±2.00
6	Distant action of SW for 24 h, germination in TW	86.7 ±3.51	97.3 ±1.36
7	Distant action of SW for 72 h, germination in TW	87.3 ± 2.67	95.3 ±1.36

Note: reference sample 2 is an empty cup under the Petri cup with the seeds; Student's criterion t for the pairs of versions according to the germination energy: 1.5—4.45, 1.7—2.81, 4.7—3.11; for the germination capacity: 1.7—3.02.

water (BW), and thawed water (ThW) using electromagnetic shields (aluminum foil). The cups with the dry and wetted seeds were exposed for 24 and 72 h. In one of the references, an empty cup was positioned under the cup with seeds during all the test. After that, the cups with the water were removed. Then, the reference seeds and the seeds of the test versions were germinated in the above types of water. The cups with the seeds were randomly positioned not less than 5 cm away from one another. In 2 and 4 days, the number of sprouts, i.e., the germination energy (GE) and the complete germination capacity (G), was evaluated according to the methodological requirements of [12]. In 7 days, the number of right sprouts (the first leaf of right sprouts is folded clockwise, while that of left sprouts, counterclockwise) was counted [13, 14].

RESULTS AND DISCUSSION

It is seen from Table 1 that the reference cup with the seeds above the empty cup and without such a cup do not differ as far as the germination energies and seed germination capacities are concerned. Thus, the empty cup did not affect the state of the seeds. In case of the seeds soaking in spring water, their germination energy is substantially higher as compared to the version of soaking in tap water (by 15%).

The germination energy and germination capacity at the distant action of tap water on the seeds do not differ from the reference. At the same time, a substantial increase in the germination energy and germination capacity during the noncontact action of the spring water on the seeds was revealed (this water was taken from the spring situated in Krikova in the Kriulaynsky region of the Moldova Republic).

Thus, the stimulus from the spring water distantly affected the dry seeds, and this stimulus can be only the field of this water. Moreover, the parameters of the test version become equal to those of the reference sample in which the seeds were soaked in spring water. Here, the assumption can be made that the spring water has distantly affected the water present in the dry

seeds in a bound, i.e., structurized, state. It turned out to be sufficient for the seeds to react as if they were contactly affected by spring water rather than tap water.

The exposure of the cups with spring water for 72 h is much more effective as compared to the exposure in tap water. No differences were revealed between the versions of the exposure of the cups with spring water for 24 and 72 h. Probably, there is a lower effective threshold of such exposure. On the whole, more precise results are observed as far as the germination energy parameter is concerned.

Thus, the presence of a water field outside a closed reservoir filled with water has been experimentally proved. The biological activity of this field is likely to depend on the structural (informative) state of the water. This field is not shielded by the plexiglas the Petri cups are made of.

For more precise data on the presence of the water field and the dependence of its activity on the structural state of the water to be obtained, an experiment using contrasting versions of the structural state of tap water (ordinary, boiled, and thawed) was carried out [11]. Dry seeds were exposed for 24 h above the cups filled with the above-mentioned types of water and then were germinated in tap water. The seeds of the reference samples were germinated in the same types of water. The germination capacity of the seeds and the number of right sprouts were taken into account. It is known that the right sprouts of Gramineae are characterized by more active growth as compared to the left sprouts [13, 14]. Based on the plentiful data, it is a more convenient criterion for evaluating the stimulation effect observed in Gramineae under the effect of different factors on seeds [13, 14].

As far as the reference sample is concerned, the seed stimulation parameter is the "thawed water" version as compared to the "ordinary water" and "boiled water" versions. There are no differences between the last two versions (Table 2).

Table 2. Germination capacity of triticale seeds and the number of right sprouts at the distant action of tap water (ordinary, boiled, and thawed) on seeds, %

No.	Versions	Germination capacity	Number of right sprouts
1	Germination in TW (reference sample 1)	85.3 ±4.11	57.0 ±1.12
2	Germination in BW (reference sample 2)	84.7 ±4.67	59.2 ± 2.54
3	Germination in ThW (reference sample 3)	93.3 ± 6.57	66.0 ± 7.05
4	Distant action of TW, germination in TW	93.0 ±4.56	60.0 ± 6.24
5	Distant action of BW, germination in TW	84.3 ± 2.68	49.2 ± 6.05
6	Distant action of ThW, germination in TW	93.3 ±3.53	64.2 ±2.36

Note: Student's criterion *t* for the version pairs by the number of right sprouts is 1.6–2.76.

Table 3. Germination energy of triticale seeds and the number of right sprouts at the distant action of tap and distilled water on dry seeds, %

No.	Versions	Germination capacity	Number of right sprouts
1	Germination in TW (reference sample 1)	70.7 ±3.01	32.8 ±1.65
2	Germination in BW (reference sample 2)	89.3 ±1.76	44.2 ± 2.89
3	Distant action of TW, germination in DW	80.7 ±4.76	45.3 ± 2.67
4	Distant action of DW, germination in TW	68.0 ± 3.05	52.6 ± 5.22
5	Distant action of DW, germination in DW	86.0 ±1.15	41.5 ±6.43

Note: Student's criterion *t* for the version pairs according to the germination energy: (*1* and *2*) 3.29, (*1* and *3*) 3.48, (*4* and *5*) 3.21, and (*2* and *4*) 3.33; according to the number of right sprouts: (*1* and *2*) 3.28, (*1* and *3*) 4.03, (*1* and *4*) 3.62, and (*1* and *5*) 2.90.

In the "ordinary water" and "thawed water" test versions of exposure, an excess over reference sample 1 ("ordinary water") was revealed. The water field, it being in this case the field of ordinary and thawed water, activates dry seeds. Substantial differences in the flavor of the thawed water field as compared to reference sample 1 (the germination of the seeds in tap water) were observed. Recall that, in this test (version 6, Table 2), the seeds after their exposure above the cup with the thawed water were also germinated in tap water. On the whole, the best results were obtained for the "number of right sprouts" parameter.

Thus, it is unambiguously demonstrated that the activity of the water field depends on its structural (informative) state: in this experiment, it is the highest for the thawed water.

As for the investigation of the role of the structural (informative) state of the water during its contact and distant action on the seeds, the "tap water–distilled water" pair is of interest since, according to Zenin [1, 2], several informative structural levels (molecular clusters) of water are formed in distilled water as early as at a normal temperature.

The data (Table 3) showed that the germination of the seeds in distilled water yields a substantial increase both in the germination energy and the number of right seeds as compared to the version with the germination in tap water (by 18.6 and 11.4%, respectively). It is likely to be attributed to the effect of both the chemical and the structural states of these two types of water.

It was confirmed during the distant effect of distilled water on the seeds: the further germination of the seeds in tap water yielded a substantial increase in the number of right sprouts as compared to the reference sample (by 19.8%), where the seeds were also germinated in tap water.

It is noteworthy that the germination of seeds in distilled water always gives identical values for all the reference and test versions (e.g., the summation of the effects at the simultaneous distant and contact action of distilled water is absent (version 5, Table 3)). Thus, the value of the effect is characterized by a certain optimum.

Based on our data, in the case of the seed germination in the water subjected to the effect of a weak millimeter-range electromagnetic field or millimeter radiation (MMR), the stimulation of the primary processes of the seeds' metabolism is observed: the germination energy and the germination capacity increase, the growth rate of the sprouts accelerates, and the number of right sprouts grows [13, 14]. According to the literary data [3, 4], MMR facilitates the structurization of the water, which yields an increase in its biological activity. Thus, it was expedient to stage an experiment using a pair consisting of tap water and the same water treated with MMR (the wavelength was 5.6 mm, the power density was 6 mW/cm^2, and the

Table 4. Germination energy of wheat seeds at the distant action of tap (ordinary and thawed) water and the water treated with millimeter radiation, %

No.	Versions	Dry seeds	Soaked seeds
1	Germination in TW (reference sample 1)	42.0 ± 2.45	54.0 ± 4.95
2	Germination in ThW (reference sample 2)	50.7 ± 1.24	74.6 ± 2.91
3	Germination in TW + MMR for 8 min (reference sample 3)	40.7 ± 4.78	
4	Germination in TW + MMR for 30 min (reference sample 4)	53.3 ± 1.24	
5	Distant action of ThW, germination in TW	56.0 ± 4.22	74.7 ± 2.91
6	Distant action of TW + MMR 8[1], germination in TW	49.3 ± 2.06	77.3 ± 2.62
7	Distant action of TW + MMR 30[1], germination in TW	51.3 ± 2.06	82.7 ± 2.64

Note: The Student criterion t for the version pairs for dry seeds: (*1* and *2*) 3.29, (*1* and *3*) 3.16, (*1* and *4*) 4.11, (*1* and *5*) 2.87, (*1* and *6*) 2.28, (*1* and *7*) 2.81; for soaked seeds: (*1* and *2*) 3.618, (*1* and *5*) 3.61, (*1* and *6*) 4.16, (*1* and *4*) 5.12.

exposure was 8 and 30 min) that served as a stimulus for the seeds [13, 14]. Dry and soaked (for 24 h) seeds of wheat (N335) were treated with MMR and analyzed. It is known that soaked seeds are more sensitive to the effect of MMR [13, 14].

According to Table 4, the thawed water in the reference sample again turned out to be more efficient than tap water (see Table 2). By the energy of the germination parameter for the dry and soaked seeds, the increase was by 8.7% and 20.7%, respectively. The effect of the MMR on the water in case of a 30 min-long exposure ensured its substantial stimulating effect on the germination of the dry seeds (a 13.3% excess over the reference sample). Unfortunately, these versions were not tested for soaked seeds, but the previous data showed that both MMR exposures for soaked seeds are stimulating [13, 14].

The distant action (for 24 h) of the thawed water on the dry and soaked seeds confirmed its stimulating function with respect to the seeds' germination with this effect (as before, version 2, Table 4) being better expresses in the soaked seeds (a 14.0 and 20.7% increase, respectively).

The answer to the key question of this experiment is as follows: the treatment of water with MMR providing stimulation of the seed germination at the contact action of this water on the seeds also yields the stimulation of the seeds germination at a distant action on them. This effect is again the most pronounced for the soaked seeds. They are stimulated by the water treated with two MMR exposures (8 and 30 min, the increase is 23.3 and 28.7%, respectively), while, for the dry seeds, the stimulation action was revealed only at a 30 min-long exposure (a 9.3% increase).

Thus, as in the previous tests (Tables 1–3), the effect of the water field turned out to substantially depend on the structural state of the water.

To determine the nature of the water field, we carried out an experiment where the Petri cups with water placed under the cups with dry seeds were covered with aluminum foil. Thus, an electromagnetic shield was created between the cups with the seeds and the water. The versions with boiled and thawed water were used.

As for the germination energy of the seeds, the version "thawed water" is predominant over the "boiled water" version in the reference sample (Table 3). As in the previous experiment, the exposure of the thawed water field to the dry seeds that are subsequently germinated in tap water gives the same result as in case of the direct germination of the seeds in the thawed water (Table 5).

In the test versions without a shield, the version of the "thawed water" field exposure also predominated over the version of the "boiled water" exposure. A similar situation is observed in the test version with shielding. In this case, the absolute values of the effects almost coincide in both cases.

Thus, the water field penetrates through the electromagnetic shield (at least, its component capable of stimulating the seed germination).

A similar picture was observed concerning the germination capacity: the "thawed water" test specimens substantially exceed the "boiled water" version both without and with a shield. Moreover, the shielding does not only weaken the effect but slightly intensifies it, which can be seen from the data of the germination energy.

As for the number of right sprouts, the observed regularity is similar to that for the germination energy and germination capacity. The differences between the contrasting test versions are substantial. The slight excess in the "shield" version over the version "without a screen" seems to be the result of the shield's operation as a mirror that, according to [9, 10], facilitates additional self-structurization of the water and the amplification of its total field and an unshielded component.

Thus, based on the behavior of three objective parameters, namely, the germination energy, the germination capacity, and the number of right sprouts grown from these seeds, it is possible to say that an

Table 5. Germination energy and germination capacity of triticale seeds and the number of right sprouts during the electromagnetic shielding of the distant action of tap water (ordinary, thawed, and boiled) on seeds, %

No.	Versions	Germination energy	Germination capacity	Number of right sprouts
1	Germination in BW (reference sample 1)	44.7 ± 4.81		56.9 ± 1.17
2	Germination in ThW (reference sample 2)	57.0 ± 0.81		63.0 ± 3.07
3	Distant action of BW (without shield); germination in TW	45.3 ± 2.91	62.2 ± 5.29	49.0 ± 4.47
4	Distant action of ThW (without shield); germination in TW	57.3 ± 3.53	75.3 ± 1.77	64.8 ± 5.61
5	Distant action of BW (with shield); germination in TW	47.3 ± 4.38	72.0 ± 0.82	43.6 ± 4.39
6	Distant action of ThW (with shield); germination in TW	61.3 ± 2.42	83.3 ± 4.43	66.2 ± 1.70

Note: The Student criterion t for the version pairs by the germination energy: (*1*, *2*) 2.53, (*2*, *3*) 3.87, (*3*, *4*) 2.63, (*5*, *6*) 2.78; by the germination capacity: (*3*, *4*) 2.38, (*5*, *6*) 2.54, by the number of right sprouts: (*3*, *4*) 2.20, (*5*, *6*) 4.80, (*1*, *5*) 2.83.

electromagnetic shields does not completely hinder the water field.

Note one more important fact: the water field exerts not only a stimulating effect (as in the case with the thawed water) but also an inhibiting one (as in the case with the boiled water). For example, the number of right sprouts in the "boiled water" test version substantially decreases as compared to the "boiled water" reference sample.

From the standpoint of the obtained data, it seems appropriate to analyze the test on revealing the line of far-ranging correlation between the populations of protozoa unicellular organisms in a water solution [5]. The solution was poured into two dishes, namely, an experimental and a reference one, made of a chemically neutral plastic. The solution in the experimental dish was subjected to a weak electromagnetic field of the millimeter range and a human field. The response of the system was registered by measuring the resistance of the water medium. Immediately after the action, the bottom of the experimental dish was set in contact with the surface of the water from the reference dish.

A synchronous response was revealed in both dishes; i.e., the excited state of the test object was passed to the reference object without any changes. The authors completely covered the bottom of the experimental dish with aluminum foil. No changes in the dynamics of the responses to the external action were observed in the reference and the experimental dishes.

The authors think that this effect shows that the far-ranging line of intercellular bonds of protozoa cannot be shielded. The authors also introduced the notion of the biological energy field of a living organism with properties different from those of an electromagnetic field. In this case, the biological structurization of water providing for the transfer of these biofields takes place owing to bioobjects (protozoa).

In this experiment, the line of the far-ranging bond between water and dry seeds (or, as assumed above, between the free water of the inductor and the bound water of the seeds (receiver)) was also obtained. It was also revealed that this line of the far-ranging bond cannot be shielded. We think that, in the experiment with the protozoa solution [5], the key role in "establishing" the bond line is played by water. Water is capable of the distant transfer of its state to objects of different nature owing to the generation of a specific field kindred to the field of a living organism.

As was mentioned above, a water field capable of "self"-amplification during its reflection at a mirror's surface was observed in the experiment, with the increase in the optical density of the water during this process pointing to it [9. 10]. In our experiment, aluminum foil also played the role of a mirror, but the field was not completely shielded in this case. At least, the distant biological activity of the water's field did not decrease as compared to the analogous activity of the water the seeds were soaked in.

The situation observed for the water's field is similar to that of the notion of a biological field: the latter is considered to be either an ensemble of known physical fields with different penetrating powers [15] or a field with an additional unidentified component. In the literature, this component is called a torsional [16], chronal [17], or nucleon [18] field, etc. We think that here we face the effect of the nonlocal interaction of macroobjects [19] analogous to the nonlocal interaction of elementary particles [20], which is one of the key regularities in quantum mechanics.

REFERENCES

1. Zenin, S.V., *Printsipy nauchnogo obosnovaniya bioenergoterapii* (Principles of Scientific Subtsntiation of Bioegergetic Therapy), Moscow, 2007.

2. Zenin, S.V., Informative System of Water, *Del'fis*, 2006, pp. 210–216.

3. Devyatkov, N.D., *Millimetrovye volny i ikh rol' v protsessakh zhiznedeyatel'nosti* (Millimeter Waves and Their Role in Vital Activity Processes), Moscow, 1991.

4. Betskii, O.V., Lebedeva, N.N., and Kotrovskaya, T.I., Unusual Properties of Water in Weak Electromagnetic Fields, *Biomed. Tekhnol. Radioelektron.*, 2003, no. 1, pp. 37–44.

5. Savel'ev, S.V. and Kuznetsov, I.V., Far-Ranging Line of Intercellular Bonds in the Interface of Intercellular Informational Interaction, *Millimetrovye Volny Biol. Med.*, 2005, no. 3, pp. 36–41.

6. Frohlich, K., *Coherent Excitation in Biological System*, New York: Springer, 1983.

7. Slesarev, V.I. and Shabrov, A.V., Distant Interaction of Water-Containing Systems, *Voda: ekologiya i tekhnologiya, EKVATEK-2006* (Water: Ecology and Technology, ECWATECH-2006), Moscow, 2006, part 2, p. 1030.

8. Maslobrod, S.N., Korletyanu, L.B., Ganya, A.I., and Gaidei, N.A., "Memory" of Water for the Effect of Millimeter Radiation by Seed Germination Criterion, *Voda: ekologiya i tekhnologiya, EKVATEK-2006* ("Water: Ecology and Technology", ECWATECH-2006), Moscow, 2006, part 2, pp. 1049–1050.

9. Petrash, V.V., Borovkov, E.I., Dovgusha, V.V., et al., Autooptical Effect, *Dokl. Akad. Nauk.*, 2004, vol. 396, no. 3, pp. 1–4.

10. Petrash, V.V., Il'ina, L.V., Dovgusha, V.V., and Borovkov, E.I., Mirror-Optical Effect of Water, *Sbornik trudov 7-i Mezhd. Krymskoi konf. "Kosmos i biosfera"* (Proc. VII Int.Crimean Conf. "Space and Biosphere"), Kiev, 2009, pp. 216–218.

11. Losev, K.S., *Voda* (Water), Leningrad: Gidrometeoizdat, 1989.

12. Internatoinal Rules for Seeds Testing, Moscow, 1984.

13. Maslobrod, S.N., Korletyanu, L.B., and Ganya, A.I., Biological Effects of Direct and Indirect Action of Millimeter Radiation on Plant Objects through Water, *Sbornik trudov 7-i Mezhd. Krymskoi konf. "Kosmos i biosfera"* (Proc. VII Int.Crimean Conf. "Space and Biosphere"), Kiev, 2009, pp. 149–151.

14. Maslobrod, S.N., Korletyanu, L.B., and Ganya, A.I., The Influence of Millimetric Radiation on Plant Viability: 2. The Changes in Seeds' Metabolism after the Treatment of Soaked Seeds, *Surf. Eng. Appl. Electrochem.*, 2010, vol. 46, no. 6, pp. 612–614.

15. Kogan, I.M., *Bioekstrasensorika* (Bioextrasensorics), Moscow, 2000.

16. Akimov, A.E. and Bingi, V.N., *Soznanie i fizicheskii mir* (Perception and Physical World), Moscow, 1995, pp. 126–136.

17. Lavrent'ev, M.M., Registration of Real Position of the Sun, *Dokl. Akad. Nauk SSSR*, 1990, no. 2, pp. 368–370.

18. Adamenko, A.A., *Modified Structure of Fundamental Interactions, Aktual. Probl. Sovrem. Nauki*, 2008, no. 2, pp. 201–210.

19. Maslobrod, S.N., Nonlocal Bond between Components of Plant Objects, *Sbornik trudov 7-i Mezhd. Krymskoi konf. "Kosmos i biosfera"* (Proc. VII Int.Crimean Conf. "Space and Biosphere"), Kiev, 2009, pp. 154–156.

20. Shimani, A., Reality of the Quantum World, *V Mire Nauki*, 1988, no. 3, pp. 22–30.